# Analysis of turbulent fluxes with the means of the continuous wavelet transform on the Belgian ICOS sites of Lonzée and Vielsalm

**Auteur :** Tzvetkov, Diana
**Promoteur(s) :** Heinesch, Bernard; Charles, Catherine
**Faculté :** Gembloux Agro-Bio Tech (GxABT)
**Diplôme :** Master en bioingénieur : sciences et technologies de l'environnement, à finalité spécialisée
**Année académique :** 2022-2023
**URI/URL :** http://hdl.handle.net/2268.2/18257

LIÈGE université
Gembloux
Agro-Bio Tech

# ANALYSIS OF TURBULENT FLUXES WITH THE MEANS OF THE CONTINUOUS WAVELET TRANSFORM ON THE BELGIAN ICOS SITES OF LONZÉE AND VIELSALM

DIANA TZVETKOV

THESIS SUBMITTED IN VIEW OF OBTAINING THE DEGREE OF MASTER IN BIOENGINEERING SPECIALIZED IN ENVIRONMENTAL SCIENCES AND TECHNOLOGIES

ACADEMIC YEAR 2022-2023

Supervisors : Pr. HEINESCH Bernard & Pr. CHARLES Catherine
Advisor : BITTON Jonathan

LIÈGE université
Gembloux
Agro-Bio Tech

# ANALYSIS OF TURBULENT FLUXES WITH THE MEANS OF THE CONTINUOUS WAVELET TRANSFORM ON THE BELGIAN ICOS SITES OF LONZÉE AND VIELSALM

DIANA TZVETKOV

THESIS SUBMITTED IN VIEW OF OBTAINING THE DEGREE OF MASTER IN BIOENGINEERING SPECIALIZED IN ENVIRONMENTAL SCIENCES AND TECHNOLOGIES

ACADEMIC YEAR 2022-2023

Supervisors : Pr. HEINESCH Bernard & Pr. CHARLES Catherine
Advisor : BITTON Jonathan

# Remerciements - Acknowledgments

Je tiens avant tout à remercier mes promoteurs, Bernard Heinesch et Catherine Charles, ainsi que mon encadrant Jonathan Bitton, qui m'ont accompagnée dans le cadre de ce travail, depuis le début et parfois jusqu'à prendre sur leurs jours de congés.

Les longues discussions abordant des sujets qui me semblent complexes encore aujourd'hui, et sûrement même plus qu'avant, ont toujours été abordées sur un ton léger toutefois sans manquer de rigueur et de sérieux. De même, les explications que j'ai reçues de chacun m'ont toujours été apportées avec bienveillance, ce qui a sans aucun doute participé à la motivation et au plaisir que j'ai pu prendre à réaliser ce travail. En effet, malgré la littérature parfois complexe et éparse, j'ai éprouvé beaucoup de curiosité à investiguer les phénomènes de turbulence atmosphérique. De plus, rien de tout cela n'aurait été possible sans le travail que Jonathan a réalisé pour son TFE en 2019, qui pose les bases théoriques de la transformée en ondelettes largements reprises dans le cadre de ce travail, ainsi que le code pour l'implémenter. De même, l'échange que nous avons eu avec Pedro Henrique Coimbra lors d'une réunion organisée par mes promoteurs me permit d'affiner la méthode, et je lui en suis également très reconnaissante.

J'aimerais aussi particulèrement remercier Gabriel, pour ses conseils et nos échanges tout au long de la période de travail, ainsi que mon frère Michaël et ma maman, qui m'ont aidée et suportée durant les derniers instants de rédaction. Plus largement, je suis reconnaissante à de nombreux amis, à Gembloux et ailleurs, pour leur présence tout au long de ce dernier semestre de vie étudiante.

Enfin, je remercie le reste de l'équipe Biodyne pour leurs conseils ponctuels et leur bonne humeur au bureau.

# Abstract

The eddy covariance and Fourier decomposition are the standard methods for the calculation and analysis of the turbulent flux. Nonetheless, their applicability is restricted by the necessity of steady-state flow conditions, rendering them unsuitable for analyzing mesoscale motions, which are the most prominent cause for energy balance unclosure according to recent review papers. Consequently, the wavelet transform has gained traction for turbulent flux analysis in the past few years. Originally developed for signal analysis, this tool effectively captures non-stationary power by decomposing the signal in both the temporal and frequency domains, and it can be used to derive flux cospectra and calculate the turbulent flux. The present paper makes use of this tool in the scope of two research objectives.

First, the parameters of the wavelet covariance formula are adapted to establish equivalence between wavelet and eddy covariance are equivalent for stationary half-hour records. Through a sensitivity analysis, the influence of parameters such as padding (introducing artificial values at signal boundaries), the shortest analyzed period, the scale step ($\delta j$), the threshold for the cone of influence ($qcoi$) in covariance computation are explored, along with the choice of mother wavelet and normalization.

The second research objective aims at investigating components of the turbulent flux that oscillate in periods larger than 30 min on two ICOS sites, namely Lonzée and Vielsalm, and that could explain energy balance unclosure on these sites. To achieve this, $CO_2$, $H_2O$, and temperature measurements are utilized to derive wavelet flux cross-scalograms, cospectra and ogives. These different representations revealed the presence of flux components in the low-frequency range that are much important that the energy balance residuals, which suggests that the flux containing oscillations of periods up to 3.2 hours is overestimated, as the consequence of a too short averaging time or of biased observations of quasi-stationary motions. In the conditions of mean wind and with the nature and scale of heterogeneities on Lonzée and Vielsalm, the presence of quasi-stationary motions is possible but could not be ascertained.

# Résumé

La méthode de covariance de turbulence et la décomposition de Fourier sont les méthodes standards pour le calcul et l'analyse du flux turbulent. Cependant, leur applicabilité est restreinte par la nécessité de conditions d'écoulement stationnaire, ce qui les rend inadaptées à l'analyse des mouvements de méso-échelle, qui sont la principale cause de non-fermeture du bilan énergétique selon des articles de revue récents. En conséquence, la transformée en ondelettes a gagné en popularité pour l'analyse du flux turbulent ces dernières années. À l'origine développé pour l'analyse de signaux, cet outil capture efficacement la puissance non stationnaire en décomposant le signal à la fois dans les domaines temporel et fréquentiel, et il peut être utilisé pour dériver des cospectres de flux et calculer le flux turbulent. Le présent article utilise cet outil dans le cadre de deux objectifs de recherche.

Tout d'abord, les paramètres de la formule de covariance en ondelettes sont adaptés pour établir l'équivalence entre les résultats de la covariance calculée par ondelettes et par covariance de turbulence pour des signaux de flux stationnaires d'une demi-heure. Par le biais d'une analyse de sensibilité, l'influence des paramètres tels que le "padding" (introduction de valeurs artificielles aux bords du signal), la plus petite période analysée, le pas d'échelle ($\delta j$), et le seuil pour le cône d'influence (*qcoi*) dans le calcul de la covariance est explorée, ainsi que le choix de l'ondelette mère et de la normalisation.

Le deuxième objectif de recherche vise à étudier les composantes du flux turbulent qui oscillent sur des périodes supérieures à 30 minutes sur deux sites ICOS en Belgique, à savoir Lonzée et Vielsalm, et qui pourraient expliquer la non-fermeture de la balance d'énergie sur ces sites. Pour ce faire, les mesures de $CO_2$, $H_2O$ et de température sont utilisées pour dériver des scalogrammes croisés de flux en ondelettes, des cospectres et des ogives. Ces différentes représentations ont révélé la présence de composantes de flux de basse fréquence qui sont bien plus importantes que les résidus de la balance d'énergie, ce qui suggère que le flux contenant des oscillations de périodes jusqu'à 3.2 heures est surestimé, soit en raison d'une période d'observation trop courte, soit en raison d'observations biaisées de mouvements quasi-stationnaires. Dans les conditions de vent horizontal et compte tenu de la nature et de l'échelle des hétérogénéités à Lonzée et Vielsalm, la présence de mouvements quasi-stationnaires est possible mais n'a pas pu être confirmée avec certitude.

# Contents

# List of Figures

# List of Tables

# 1 Introduction

Understanding the ecological role of ecosystems as either "sources" or "sinks" of gases, energy, and pollutants is a prerequisite for the mitigation of climate change (IPCC, 2014). Monitoring exchanges of these scalars between the surface and the atmosphere is a direct method to quantify them (Franz et al., 2018) with minimal disturbance of the ecosystems (Aubinet et al., 2012, p.346). The capability of sonic anemometers, sonic thermometers and infrared gas analyzers to detect variations at scales below the hour is the key element for the estimation of surface fluxes with the eddy-covariance (EC) technique (Aubinet et al., 2012, p.1). The fundaments of EC already have been proposed in 1951 by Swinbank (Aubinet et al., 2012, p.1), but could not be implemented before adequate sensors were developed in the 1990s. Closely aligned with these technical advancements, the past 30 years have witnessed a remarkable surge in campaigns involving EC measurements conducted from towers (Aubinet et al., 2012, section 1.1). At the center of these initiatives, the NASA initiated in 1997 a "network of networks" named FLUXNET (NASA, 2015: https://fluxnet.org/data/fluxnet2015-dataset/), which brings together regional networks that collect high-frequency measurements with the goal of creating a global database. Initially, networks from Europe, Asia, and North America were included, and later expanded to include Brazil, Canada, China, and Australia. Presently, the regional networks within the FLUXNET initiative encompass the Integrated Carbon Observation System Research Infrastructure (ICOS) (Franz et al., 2018), CarboEurope, AmeriFlux, AsiaFlux, and CarboAfrica (Mader, 2020). In addition to that, numerous aircraft measurement campaigns have emerged, many of which took place in the United States namely the CHEESEHEAD19 (Butterworth et al., 2021), HI-SCALE (Schobesberger et al., 2023), CABERNET (Misztal et al., 2014), but also in the rest of the world such as the BEAM97 campaign in Spain (Attié and Durand, 2002), HAPEX-Sahel in Niger (Lothon et al., 2007). While aircrafts allow conducting spatial measurements restricted in time, towers provide single-point measurements that have the advantage of being continuous. Hence, both techniques are complementary and prove valuable in ecosystem monitoring (Metzger et al., 2013).

Apart from measurements, the EC technique also encompasses a data processing chain for the estimation surface fluxes under the assumption that turbulent flow is the primary mode of transport of scalars near the surface. More precisely, it is within the atmospheric boundary layer (ABL), which is the "part of the troposphere directly influenced by the Earth's surface and that responds to surface forcing with a timescale of approximately 1 hour or less" (Stull, 1988, p. 2) that scalars originating from the ecosystem are transported. Within the ABL, air movement occurs through mean wind, waves, and turbulence (Fig. 1). While horizontal transport is mainly effectuated by mean wind, vertical transport is predominantly governed by turbulence. In the ABL, turbulence primarily arises in the form of large convective cells, created from buoyancy forces due to thermal forcing on the ground, and from shear (frictional drag) decelerating horizontal wind near the surface (Stull, 1988, p. 4). The large cells break down into smaller cells through an energy cascade (Stull, 1988, p. 32). The resulting turbulent flow can be visualized as a combination of eddies of different sizes (Stull, 1988, p. 29), as represented in Fig. 1. The EC method evaluates the turbulent flux of a scalar by combining the measured fluctuations in its quantity in ambient air with the measured fluctuations of the vertical wind velocity. Measurement towers are used to position the sampling point within the surface layer (SL), which corresponds to the lower 10% of the ABL and that is characterized by constant fluxes with respect to height, as well as variations in turbulent fluxes and stress that are less than 10% of their magnitude (Stull, 1988, p. 10).

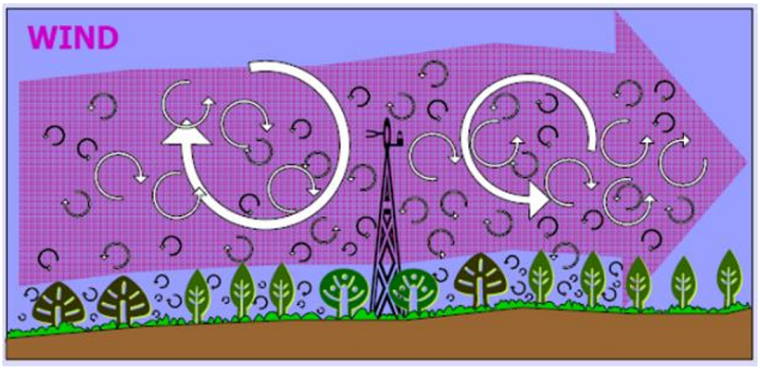


Figure 1: Schematic representation of turbulent eddies and mean flow (Burba and Anderson, 2010)

However, the EC method of calculation of the turbulent term is only valid for stationary flows, and results are highly unreliable when this condition is not met (e.g. Dutaur et al., 1999; Foken and Wichura, 1996; Mahrt, 1998; Fortuniak et al., 2013, Li et al., 2023). Stationarity is undermined by various phenomena such as sunrise and sunset, large-scale motions and passage of clouds (Mahrt, 1998; Finnigan et al., 2003; Lee et al., 2004, p. 177). To avoid discarding large amounts of data, stationarity can be artificially forced by removing low frequency components from the time-series. However, such detrending operations interfere with theoretical assumptions inherent to the EC flux calculation (e.g. Mahrt, 1998; Mahrt, 2010). In practice, non-stationary records[1] are discarded from the analysis (Aubinet et al., 2012, section 4.3.2), which can seriously diminish the amount of analyzable data (Aubinet et al., 2012, section 6.1) and prevent the analysis of specific events such as gaseous outbursts (Göckede et al., 2019).

To insure stationarity, single-point EC fluxes are most generally averaged over 30 min, which corresponds to a period for which neither high-frequency fluctuations (see 8.2) nor low-frequency components (Haugen et al., 1978) can alter significantly the mean and higher-order moments of the signal (i.e. induce non-stationary, Foken and Wichura, 1996).

Actually, the primary reason for a to set the averaging period to 30 min is to only include eddies of turbulent scales – i.e. that are of sizes smaller than 2 (Mahrt, 2010) or 3 km and revolve in periods shorter than one hour (Stull, 1988, p. 20) – to the estimation of the turbulent flux. Only these motions are believed to transport scalars from the ecosystem, which is an area wide a few hundreds of meters up to a few kilometers (e.g. Mauder et al., 2008; Lothon et al., 2007) to a measurement tower. On the contrary, eddies that are larger than a few tens of kilometers and revolve in periods longer than a day (Stull, 1988, p. 20) belong to the synoptic range, do not carry scalars from the ecosystem to the measurement point (Lee et al., 2004, p.102). Because the revolution period of eddies, and thus their size are related to the period of an oscillation of the measured signal under the hypothesis of frozen turbulence (e.g. Kaimal and Finnigan, 1994), it is possible to exclude synoptic motions from the calculation of the turbulent flux with an adequate choice of the averaging time (e.g. Stull, 1988, p. 33 ; Lee et al., 2004, p. 102) since only the oscillations of periods shorter than the window are included in the calculation of the turbulent flux term.

Spectral decomposition (i.e. conversion of the time-series into a function of frequency) of the turbulent flux has allowed to observe a spectral gap at periods of 30 - 60 min (e.g. Fig. 2, Van der

[1] A record is a finite portion of a signal.

Hoven, 1957), which comes in handy to separate turbulent and synoptic motions (Stull, 1988, p.33 ; Terradellas et al., 2001; Saito and Asanuma, 2008).

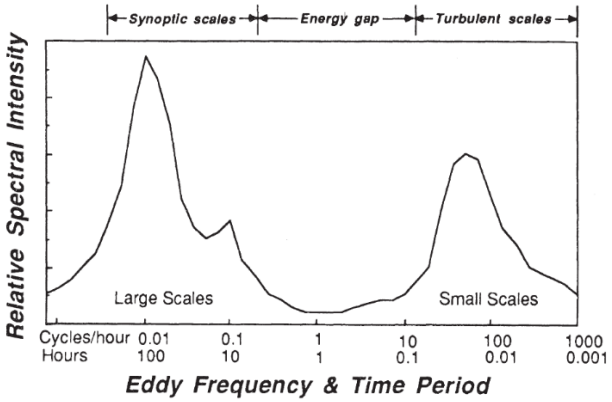


Fig. 2.2 Schematic spectrum of wind speed near the ground estimated from a study of Van der Hoven (1957).

Figure 2: Representation of the spectrum of horizontal wind velocity established by Van der Hoven (1957) and reworked by Stull (1998)

The observation of the spectral gap has brought the scientific community to the consensus that averaging measurements made a few (tens of) meters above a surface of interest over 30 min is adequate to capture all motions that are responsible for the exchange between this surface and the above atmosphere (Stull, 1988, p.33; Lee et al., 2004, p.102).

In practice, the averaging time of EC is usually set to 30 min – or 15 min in some exceptional cases (e.g. Dupont, 2019) – which limits the finest temporal resolution of EC flux estimations to that period. But another major drawback of EC was discovered when recent studies (e.g. Sakai et al., 2001; Finnigan et al., 2003; Lee et al., 2004, p.102; Von Randow et al., 2002) suggested that there also exists motions in the mesoscale range, of sizes comprised between 3 to a few tens of kilometers and that these motions carry scalars from the ecosystem to the measurement point. Because these motions revolve in periods ranging from 1 hour to a day (Orlanski, 1975; Stull, 1988, p.20; Finnigan et al., 2003; Mahrt, 2010), they are disregarded from the calculation of the turbulent flux with EC.

The monitoring of water vapor and energy over the past 25 years has played a major role in the discovery of mesoscale motions (Mauder et al., 2020). Since the late 1980 s (Foken, 2008), the exchange rates of these scalars computed with EC have been consistently underestimated, which has been noticed since the available energy (I in Eq.1) arriving to ecosystems is consistently underestimated by the turbulent fluxes of energy calculated with EC (II in Eq. 1), which constitutes unclosed budget equations. In its simplified form, the surface energy balance (SEB) equation writes (e.g. Foken, 2008):

$$\underbrace{R_n - G}_{I} - \underbrace{(H + \lambda E)}_{II} = Res \tag{1}$$

Where $R_n$ is the net radiation, $G$ is the soil heat flux, $H$ is the sensible heat flux, $\lambda E$ is the latent heat flux and $Res$ is the SEB residual, which should theoretically be close 0 if the SEB were computed correctly. SEB unclosure has been extensively studied across different land covers and external conditions (Mauder et al., 2020), but still remains a major interrogation in modern micrometeorology.

Even though instrumental errors (Foken, 2008), data correction for time-lag, high-frequency losses and coordinate rotation, neglect of heat storage in the canopy, energy storage in photosynthesis and water (Mauder et al., 2020) have previously been pointed out for this underestimation, recent review papers (Foken et al., 2008; Mauder et al., 2020) state that these errors have become negligible and that the most prominent explanation for the unclosure is the presence of mesoscale motions. If mesoscale components transport energy, they might as well transport other scalars (carbon dioxide, methane, fine particles, etc.). Phenomena causing mesoscale motions are far from uncommon : they can be generated by intermittent atmospheric transport (Sun et al., 2004; Prabha et al., 2008; Schaller et al., 2019), as well as large obstacles (Mahrt, 2010) and heterogeneity of the land cover (Stoy et al., 2013; Paleri, 2022) or topography (Finnigan et al., 2003), and they are likely to occur during the day, which is also when SEB unclosure is most problematic (Mauder et al., 2006; Oncley et al., 2007).

In order to include their contributions to the turbulent flux calculation, attempts have been made to extend the averaging period of EC (Sakai et al., 2001; Finnigan et al., 2003; Foken et al., 2006a; Saito and Asanuma, 2008). But these tryouts have not become common practice, because the necessity to have stationary flow during extended periods limits the amount of available data. For example, records containing measurement dysfunctions and important variations of the flow such as seasonal, weather and diurnal alterations have to be excluded (Finnigan et al., 2003).

The inadequacy of EC due for the analysis of mesoscale motions calls for an alternative method of flux calculation. The wavelet transform (WT) is a mathematical tool that can be used to calculate fluxes from EC measurements. It is originally a tool for spectral analysis, which decomposes signals and functions in frequency and time space (Katul et al., 1994) instead of infinite frequency components such as Fourier decomposition (Farge, 1992). Since it does not require steady-state condition of flow (e.g. Katul et al., 1994; Howell and Mahrt, 1997), it is better suited to analyze mesoscale motions and thus improve turbulent flux estimations. Moreover, its ability to separate time and frequency resolutions allows for the inclusion of large-scale contributions with fine temporal resolutions (Dupont, 2019; Schaller et al., 2019).

The cross-wavelet transform (XWT) is one of the numerous tools brought by wavelets and is particularly useful for the study of turbulence. XWT is composed by the product of WT coefficients for two signals (Hudgins et al., 1993) and its coefficients are interpreted as a local measure of covariance in the time-frequency plane, than can be displayed in a cross-scalogram. Aggregating the real part of its coefficients over time produces the cospectrum (Stull, 1988, p. 331) which resembles the Fourier spectrum but with a smoother appearance (Desjardins et al., 1997). Additionally, aggregating over frequencies and applying certain scaling factors (Torrence and Compo, 1998) computes the covariance of two signals, which corresponds to the covariance computed with EC (Stull, 1988, p.331; Schaller et al., 2017).

Lately, an increasing number of researchers are utilizing the XWT to calculate fluxes with the hope to capture mesoscale components in daytime conditions and enhance estimations of the turbulent flux (e.g. Von Randow et al., 2002; Saito et al., 2007; Saito and Asanuma, 2008; Dupont, 2019; Paleri et al., 2022), but this tool has not yet succeeded in resolving the SEB closure problem. The present study incorporates into the existing body of research by enlarging the seek of mesoscale motions that are supposedly causing SEB unclosure. The aim of this research is twofold: the first objective is to adjust the parameters of the XWT to insure that it can accurately estimate the turbulent flux of temperature and $CO_2$ at the ecosystem scale. The accuracy of the calculation is verified by comparing

the XWT results with EC results under stationarity data. Following this, the second objective is to use the adjusted XWT to derive turbulent flux cospectra of temperature, water vapor and carbon dioxide on two ICOS sites distinct by their topography and land cover. This calculation will serve to analyze motions revolving in periods >30 min and hopefully enlighten the reasons why the EC method underestimates turbulent fluxes at the ecosystem scale. To meet this second objective, the analysis will focus on conditions of well-developed fluxes and non-intermittent turbulent transport when the SEB unclosure is important.

The following sections, the theoretical foundations of EC flux calculation and spectral analysis are presented, followed by a review of some of the observation that have been made with EC. Then, theoretical background and previous observations of mesoscale motions are put forward, and the study sites on which measurements for the current analysis are conducted are also presented. Following that, the methodologies necessary to attain the two research objectives are subsequently presented, after which the results are discussed by comparing them to previous studies and to site specifics.

# 2 Materials

This aim of this section is to present the theoretical basis and literature review that will serve the following investigation, and introduce the studied sites from which data is retrieved. The cornestone of the flux calculation being the scalar budget equation, its derivation is presented at before anything else, allowing not only to understand the essence of the turbulent flux term, and to justify its calculations with the EC method, which in turn allows to justify the requirement of stationary of flow and the restriction to a 30-min averaging period inherent to EC. In order to weight evenhandeldy the advantages offered by WT when it comes to turbulent flux calculation, it is necessary to first presents the possible adaptations that can be made in EC to cope with the restrictiveness of its analyzing window and the requirement for flow stationarity. Then, results of spectral analysis conducted with EC are shown, after which previous studies comparing EC and WT are presented. General results obtained from investigation of mesoscale motions with wavelets are also discussed. Finally, the study sites and the choice of the data that will serve the present research are presented.

## 2.1 The EC method

### 2.1.1 Scalar budget equation

Scalar budgets are established following the conservation of mass in a control volume. In the following developments, the scalar intensity of a atmospheric scalar will be noted $c$, and designates molar concentration $[\mu mol.m^{-3}]$ or temperature $[K]$ for gases and heat respectively (Aubinet et al., 2012, p.5). Under the assumption that molecular diffusion is negligible, the scalar conservation equation at one point in space writes (Lee et al., 2004, p.37):

$$\frac{\delta c}{\delta t} + \nabla \cdot \mathbf{u}c = s \tag{2}$$

where $t$ is the time variable, $S$ is the source of scalar, $\mathbf{u}$ is the vector of wind velocity and $\nabla$ designates the divergence operator. To calculate scalar budgets from continuous single-point measurements performed e.g. from a tower, the quantities are averaged temporally (denoted with a horizontal bar) over

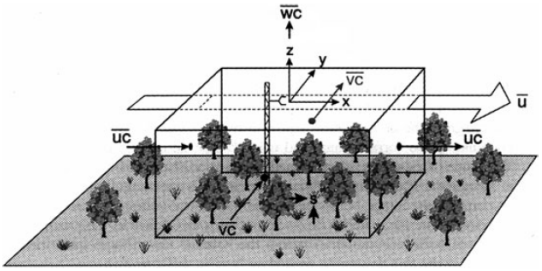


Figure 3: Paralellepipedic control volume of horizontal square basis and height $h$. The horizontal arrow with a subscript $\bar{u}$ represents the wind velocity (Aubinet, 2012)

a record period of typically 30 min and integrated over a control volume $V$, which writes (Lee et al., 2005, p.213):

$$\int_V \left( \frac{\delta \bar{c}}{\delta t} dV + \int_V \nabla \cdot \overline{\mathbf{u}c} \right) dV = \int_V \bar{s}\, dV \tag{3}$$

This equation can be expanded in space in a 3-dimensional orthonormal coordinate system noted $(x,y,z)$ in which the vector of wind velocity $\mathbf{u}$ expands in this coordinate systems as $\mathbf{u} = u_{i_{1,2,3}} = u.1x + v.1y + w.1z$ . The region contributing to the flux measured at the tower, i.e. the control volume, is taken for the purpose of simplicity as a parallelepiped with a square horizontal basis and of height $h$. The measurement point is situated in the horizontal middle of the control volume and at the top of the control volume $h$ (Fig. 3). Further, Eq. 2 is expanded following Reynolds decomposition, which allows to attribute separate terms to the turbulent motions and to the mean flow. It implies the calculation of the temporal averages, keeping the annotation of the horizontal overbar, $\bar{c}$ and $\bar{u}_i$:

$$c(t) = \bar{c} + c'(t)\ ;\ u_i(t) = \bar{u}_i + u_i'(t) \tag{4}$$

$$\Leftrightarrow\ \overline{u_i c} = \bar{u}_i \bar{c} + \overline{\bar{u}_i c'} + \overline{u_i' \bar{c}} + \overline{u_i' c'} \tag{5}$$

Further, Eq.3 simplifies following two hypothesis (Lee et al., 2005, p.213-217):

1. The validity of Reynolds assumptions under stationarity of flow (see Appendix 8.1.1): the second and third term cancel out, leaving the following decomposition: $\overline{u_i c} = \bar{u}_i \bar{c} + \overline{u_i' c'}$
2. The assumption that air is incompressible verifies the continuity of flow and implies $\delta \overline{u_i} / \delta x_i = 0$

Expanding Eq.3 into the 3-dimensional othornormal coordinate system, applying Reynolds decomposition and the simplifications stated hereabove writes:

$$\int_V \left( \underbrace{\frac{\delta \bar{c}}{\delta t}}_{I} + \underbrace{\bar{u}\frac{\delta \bar{c}}{\delta x} + \bar{v}\frac{\delta \bar{c}}{\delta y}}_{II} + \underbrace{\bar{w}\frac{\delta \bar{c}}{\delta z}}_{III} + \underbrace{\frac{\delta \overline{u'c'}}{\delta x} + \frac{\delta \overline{v'c'}}{\delta y}}_{IV} + \underbrace{\frac{\delta \overline{w'c'}}{\delta z}}_{V} \right) dV = \int_V \underbrace{\bar{s}}_{VI}\, dV \tag{6}$$

Where $I$ is the storage term, $II$ represents the horizontal advection, $III$ the vertical advection, $IV$ the horizontal flux divergence, $V$ the turbulent flux and $VI$ the source of sink of scalar in the control volume, which is the flux of mass or energy from the soil to the atmosphere (Finnigan, 1999). Inside the control volume these terms depend on space and should carry the subscript $(x,y,z)$. This subscript is however not noted for the purpose of simplicity.

The assumption is made that the surface is planar and homogeneous, so that (1) the scalar source field is homogeneously spread on that surface and (2) the wind flows horizontally and homogeneously in only one direction. The x-axis of the coordinate system is placed in the direction of the mean wind flow, refered to as the streamwise direction. As a consequence, there is no component of the mean flow along the y-axis, which is refered to as the cross-wind direction (Fig. 3). Hence, the mean wind in the vertical and cross-wind direction are assumed to be negligible ($\bar{w} = 0$ and $\bar{v} = 0$) and the horizontal homogeneity of the horizontal wind flow implies that the derivatives with respect to $x$ and $y$ cancel. This simplies Eq. 6 as follows :

$$\int_V \left( \underbrace{\frac{\delta \bar{c}}{\delta t}}_{I} + \underbrace{\frac{\delta \overline{w'c'}}{\delta z}}_{V} \right) dV = \int_V \underbrace{\bar{s}}_{VI} \, dV \tag{7}$$

The assumption of horizontal homogeneity further implies that variables equal their horizontal averages at any height $z$ (Finnigan, 1999). This comes in handy since variables are only sampled at the central point of the control volume $(x,y) = (0,0)$. For instance, taking an arbitray quantity $\phi$, the equality writes :

$$\phi_{x=0,y=0,z} = \int_{-L}^{L} \int_{-L}^{L} \phi_{x,y,z} \, dx \, dy \tag{8}$$

which simplifies the integration over the control volume into an integration only over height. In other words, it reduces the equation from three dimensions to only one and Eq. 7 becomes:

$$\underbrace{\int_0^h \frac{\delta \bar{c}}{\delta t} dz}_{I} + \underbrace{\int_0^h \frac{\overline{w'c'}}{\delta z} dz}_{V} = \underbrace{\int_0^h \bar{s} \, dz}_{VI} \tag{9}$$

The storage term ($I$), which is the vertical integral of the temporal derivative of $c$, has to be measured at different heights. The total of sources and sinks over the record period and the height are evaluated, hence the integral of $s$ with respect to height simplies as $\bar{S}$. It represents the next echange of the scalar between the control volume and the exterior environment over the record period (Aubinet et al., 2012, p.11). Finally, in term $V$, $\delta z$ and $dz$ simplify, which gives:

$$\underbrace{\int_0^h \frac{\delta \bar{c}}{\delta t} dz}_{I} + \underbrace{\overline{w'c'_h}}_{V} = \underbrace{\bar{S}}_{VI} \tag{10}$$

The eddy-covariance technique refers to the estimation of the turbulent flux term $\overline{w'c'}$ of the scalar budget equation as a covariance of the time-series of $w$ and $c$. Standard EC practice is to calculate the covariance by averaging the fluctuating terms of $w$ and $c$ over the record period $T$ :

$$Cov_{EC} = \overline{w'c'} = \frac{1}{T} \sum_{i=0}^{T} (w_i - \bar{w})(c_i - \bar{c}) \tag{11}$$

### 2.1.2 Adapted EC

As mentioned earlier, the two limitations that significantly impair the performance of the EC for the calculation of the turbulent flux is that (1) the averaging period of 30 min disregards contributions of motions revolving in periods longer than 30 min and (2) the requirement of stationarity of the flow leads to the exclusion of important amounts of data. The attempts that have been maid to adapt the EC method to cope with these two limitations are presented here.

#### 2.1.2.1 Extending the averaging period

As a reminder, in the case where significant mesoscale motions are present, extending the averaging period so that is longer than the revolution time of these motions allows to integrate their contribution to the turbulent flux term $\overline{w'c'}$. This improves the estimation of the source term in the mass balance. If the averaging period is not long enough for that, the motions of periods longer than the averaging period find themselves in the product of the means ($\bar{w}\bar{c}$). As Lee (1998) proposed, $\bar{w}\bar{c}$ could be added in the mass balance, which would prevent from bothering to set an adequate averaging time. But Finnigan (1999) and Finnigan et al. (2003, p.18) disfavor this suggestion on the grounds that $\bar{w}\bar{c}$ might also be partly compensated by the terms of horizontal advection and, over averaging times in the range of 30 min, by transient changes in the storage term and the source term. As a consequence, adding $\bar{w}\bar{c}$ to the mass balance might include new unwanted contributions from these other terms.

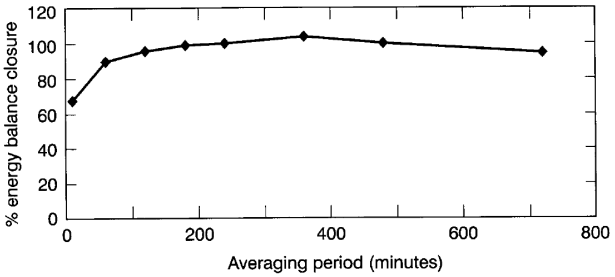


*Figure 14.* Ratio of total energy flux, $H + LE$ to available radiant energy, $Rn - G$ at Manaus for different averaging and rotation periods.

Figure 4: Ratio of total energy flux $H + \lambda E$ to the available energy $Rn - G$ according to averaging time for a homogeneous forest (Finnigan et al., 2003)

Coming back to extending averaging periods of EC, it has the downside that datasets must be stationary over the extended periods (Mauder et al., 2020). In practice, this translates into the constraint that the dataset must not contain any gaps or measurement errors, nor any significant seasonal or weather changes. Diurnal changes can also undermine stationarity, unless the averaging time is long enough to smoothen its contribution (Finnigan et al., 2003). For example, Sakai et al. (2001) performed averaging over 3-hour periods, centered around the local noon. Their publication was followed closely by that of Finnigan et al. (2003), who performed EC over averaging periods of 4 hours, and even though the time was not exactly consecutive, these blocks were assembled to form larger blocks long up to 12 hours. On two sites with complex topography, they achieved to increase the estimations of latent heat, sensible heat, and $CO_2$ by around 15% with the averaging time of 12 hours and by 8% with an averaging time of 8 hours compared to the averaging time of 15 minutes, but the certainty of the estimation was importantly greater for the 8-hour averaging period. On a site that was considered horizontally homogeneous, a satisfactory SEB closure was achieved with an averaging period of 4

hours ( 4).

However, the criteria of selecting days containing six 4-hour blocks of uninterrumpted data, which lead to the exclusion of 55 days out of 67, illustrating the selectiveness of this method regarding time-series. In another study, Foken et al. (2006a) extended the averaging time of EC up to 4 hours on data from the LITFASS-2003 experiment, which is a maize field, but the calculated ogives of momentum could only be analyzed for periods of revolution up to 2 hours, because longer averaging time undermined stationarity. For this research, only 121 4-hour time-series (that were in some cases overlapping since only 2-hour periods were analyzed) were retrieved from the 2-month experiment (Foken et al., 2006b).

In summary, extending the averaging period of EC leads to excluding many datasets due to requirements of stationarity of the time-series. The litterature review performed in the scope of the present study suggests that the practise is rather exploratory and has been dropped out in favor of wavelet techniques.

#### 2.1.2.2 Detrending

Another adaptation that can be made to EC is to remove instationarity of the records by the means of detrending; i.e. filtering of low-frequency components. The detrending operation replaces the temporal average in Eq. 11. For this reason, detrending is often referred to as "averaging operation". The use of the temporal mean, which is not considered detrending, is known as "block averaging". Among researchers, the relevance of detrending is controversed. Linear detrending, i.e. removing from the time-series its linear fit, is said to effectively remove non-stationarity due to synoptic components, but not mesoscale ones, and applying higher-order filters does generally not improve that (Mahrt, 1998). Saito et al. (2007) hypothesis that detrending may be efficient for high-canopy vegetation, but not for short vegetation. Saito and Asanuma (2008) showed that when the averaging time is set to the cospectral gap, EC results are independent from the averaging procedure. Either way, Mahrt (1998) supports that the choice of the filter is arbitrary and unsupported by actual physical phenomena. On top of that, any type of detrending discredits Reynolds assumptions, as it has been proven by Lee et al. (2005, p. 14). In summary, many suggest to exclude instationary records rather than applying detrending (e.g. Mahrt, 1998; Mahrt, 2010).

## 2.2 Spectral analysis of the atmospheric turbulent flow

### 2.2.1 Fourier analysis

Spectral decompositions convert time-series into a function of frequency. In micrometeorology, they are used to decompose the flux $w'c'$ into its different constituents, the eddies (Stull, 1988, section 2.1 ). Within the EC method, the benchmark processing technique of spectral analysis is Fourier decomposition, which decomposes the signal into infinite sine waves of different periods (Farge, 1992). Because the sine waves are infinite, the decomposition disregards temporal variations of the signal and as a consequence, it is only exact when the flow is stationary. For an extended comparison between wavelet and Fourier spectral decomposition, see Bitton (2019).

Coefficients of the spectral decomposition (let it be Fourier or any other) are depicted in a power spectrum or cospectrum for respectively a signal or a product of two signals. The (co)spectra can

be interpreted as the distribution of (co)variances into multiple frequency bands of width equal to the sampling period (Aubinet, 2012, section 1.5.1). Accordingly, differential terminology will from now on be adopted in this paper to designate the gap found in the cospectrum (cospectral gap) and in a spectrum (spectral gap). The turbulent flux being a product of $w'$ and $c'$, it is represented in a cospectrum.

The integration of Fourier coefficients is supposed to render the average turbulent flux (Aubinet 2012, section 1.5.1) :

$$Cov_{EC} = \overline{w'c'} \simeq \int_0^\infty C_{wc}(f)df \tag{12}$$

where $C_{wc}(f)$, the Fourier coefficients of the product $wc$ depending on frequency $f$ are integrated in the frequency domain. However, caution must be taken with these assumptions : Vickers and Mahrt (2003) warn that a direct relationship between both equations does not exist (Howell and Mahrt, 1997) warns that the integration of Fourier spectra does not satisfy Reynolds averaging. Anyhow, most often the integral of the flux cospectrum is not used to calculate the average value of the flux over the whole record period as in Eq.12. Instead, the ogive, which is the cumulative integral from the highest frequencies to some arbitrary frequency (Foken, 2008), is used to determine quantitative relative contributions from some frequency bands to the total flux (Von Randow et al., 2002; Foken et al., 2006a&b; Mauder et al., 2007a). Further, spectral decompositions and their ogives are used to identify the (co)spectral gap and the frequencies that most largely contribute to the flux (Terradellas et al., 2001; Vickers and Mahrt, 2003; Dupont, 2019), establish similarity theories (i.e power laws that model turbulent fluxes from variables such as friction velocity and mean wind magnitude; Stull, 1988, p. 316; Kaimal and Finnigan, 1994, p.35; McNaughton and Laubach, 2000; Nordbo and Katul, 2013) and are useful to determine a suitable averaging period, according to site-specific conditions (Mahrt, 2010; Saito and Asanuma, 2008).

The size of the eddies composing the flow can be derived from the frequencies observed at a single measurement point via Taylor's hypothesis of frozen turbulence, which is the assumption that the flow is not altered as it passes the measurement point under mean wind, and thus that there is a direct relationship between the wavelength $\lambda$ and the frequency f $[s^{-1}]$(Kaimal and Finnigan, 1994, p.39):

$$\lambda = \bar{U}/f \ [m] \tag{13}$$

where $\bar{U}$ is the mean horizontal wind given by $\bar{U}^2 = u^2 + v^2$ Some authors prefer to speak in terms of the wavenumber $\kappa$:

$$\kappa = 2\pi/\lambda \ [m^{-1}] \tag{14}$$

### 2.2.2 Wavelet analysis

The WT is a tool for spectral analysis that decomposes signals and functions in frequency and time space (Katul et al., 1994) by performing the convolution between the time-series and an analyzing kernel – the wavelet (Torrence and Compo, 1998). In that way, the WT is analogous to Fourier decomposition, but Fourier decomposition uses infinite sinusoids as analyzing functions (Bitton, 2019), the temporal localization of the different frequencies composing the signal are inaccessible (Katul et al., 1994). On the contrary, a wavelet has finite oscillations in both the time and frequency domains (Fig. 5), which property makes it suitable to capture instationarities of the signals (Katul et al., 1994; Torrence and Compo, 1998; Schaller et al., 2017).

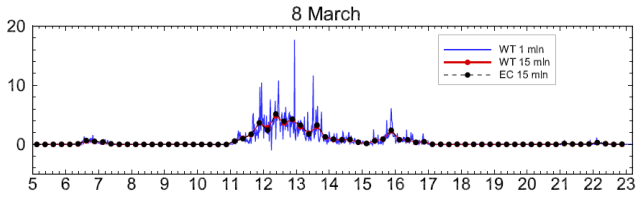


Figure 6: Momentum flux [$10^6$ $m^{-2}s^{-1}$] estimated with WT (1 min and 15 min averaging period) and with EC (15 min averaging period) (Dupont, 2019)

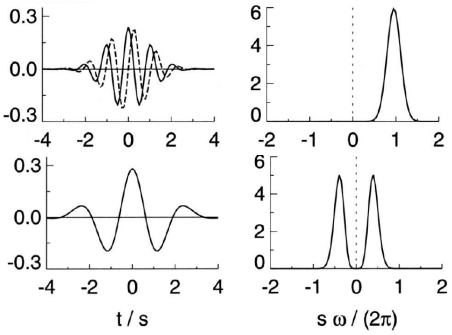


Figure 5: Representation of the Morlet (left) with the dashed lines representing its imaginary part, and Mexican hat (right) wavelet; in both the time and frequency domain. t is the time, s the scale parameter (noted *a* in the present paper) and ωis the frequency (Torrence and Compo, 1998).

Moreover, it allows fine temporal resolution that can resolve short-term events such as outbursts of methane (Göckede et al., 2019).

### 2.2.3 Comparison between XWT and EC

In the range of frequencies that can be captured by EC, Fourier and wavelet spectra also show the same distribution of momentum and scalar flux, even though the wavelet spectrum appears much smoother (see Fig. 6) (Farge, 1992; Dupont, 2019).

Moreover, the study of Schaller et al. (2017) has shown that the fluxes derived with the Mexican hat and the Morlet wavelet match the EC fluxes with a good precision ($R^2 \approx 0.98$) when the flow is stationary. Wavelet-derived fluxes are slightly lower than EC, and the underestimation is more pronounced for Mexican hat than for Morlet. EC and wavelets also show similar results when stationary fluxes are averaged over 15 minutes (Dupont, 2019).

## 2.3 Investigation of mesoscale motions

### 2.3.1 Definition and physical origins

Investigating mesoscale motions formulates the question of their exact nature and classification. Apart from the practical separation of turbulent and mesoscale motions with the spectral gap and the spatial and temporal scales that are generally associated to some type of motion, a more fundamental classification of motions is still a matter of debate (Von Randow et al., 2002) but is required since motions in these categories show several fundamental differences. First, mesoscale motions do not obey similarity theories, which relate turbulent fluxes to the local wind shear, temperature stratification

(Vickers and Mahrt, 2003) and measurement height (McNaughton and Laubach, 2000), and they also disrespect the scalar similarity obeyed by turbulent motions (Mauder et al., 2007a, 2010), which is the proportionality of fluxes of different scalars. Second, the processes leading to mesoscale motions such as heterogeneous forcing, entrainment and passage of clouds happen outside of the boundary layer, contrary to small-scale turbulence that stems from inner-boundary layer phenomena (Williams et al., 1996). Third, mesoscale motions can be two-dimensional, whereas turbulent-scale motions are three-dimensional (Etling and Brown, 1993; Prabha et al., 2007a&b). Lastly, the turbulent and mesoscale fluxes are governed by different dynamics: the cospectra of turbulent fluxes and accordingly of mesoscale fluxes of a few successive days are correlated with each other, but the turbulent fluxes are not correlated with the mesoscale ones (Foken et al., 2006a). The same argument was investigated in the study of Von Randow et al. (2002) who showed that fluxes in the turbulent range are pretty similar among records, but show large variations in the mesoscale range (see section 2.3). Studies attempting to build process-related classifications building on these arguments are presented in Appendix 8.4. In the end, partitioning of motions into different classes is mostly useful to isolate contributions of "locally meaningful" (Lee et al., 2004, p.102) fluxes for short term ecosystem-scale flux calculation (Stull, 1988, p.19) and to establish similarity theories, whereas the distinction is less important for long-term budgets (Mahrt, 2010). In the present study, motions in scales > 30 min will be analyzed without assuming any partitioning *a priori.*

The physical processes behind mesoscale motions differ from those causing turbulent ones. As a first approach, correlations between mesoscale motions and environmental conditions can be established. Conditions that have been found to favor the development of mesoscale motions include low friction velocity (u*) linked to high atmospheric instability (Stoy et al., 2013; Mauder et al., 2020) and heterogeneities of the topography and land cover (Patton et al., 2005; Stoy et al. 2013; Mauder et al., 2020). For heterogeneous forcing, mesoscale processes are additionally correlated to turbulent kinetic energy and measurement height, as well as differences in scalar mean values between the surface and the measurement height.

Wavelets unlocked the possibility of a more precise analysis. Calculating fluxes with XWT, Saito et al. (2007) demonstrated that the presence of such components depends on the wind direction, and therefore, the upwind surface conditions at the mesoscale. Also using XWT, Zhang et al. (2007) observed near-neutral conditions and high wind speeds preferentially yield mesoscale motions. This contradicted other studies who found that mesoscale were less correlated to speed than turbulent motion (Sun et al., 1996) and that mesoscale motions appear under high thermal instability with poor mixing (i.e. small friction velocity) (Stoy et al., 2013) and weak wind (Patton et al., 2005). Actually, mesoscale motions emerge under various and sometimes opposing conditions depending on their physical origin. One possible cause is turbulence intermittency, which refers to events of outbursting or under-developed turbulence, which translates into mesoscale fluxes with no increase of local source emissions. Various phenomena have been found to cause intermittency: wave–turbulence interactions (Einaudi and Finnigan 1993), low-level nocturnal jets (Prabha et al., 2007a, 2008; Schaller et al., 2019), shear-flow instability, gravity waves (Sun et al., 2004; Schaller et al., 2019), weather fronts, and cold-air drainage (Schaller et al., 2019).

Another cause of mesoscale motions is spatial heterogeneity at the mesoscale – also called landscape scale – (Finnigan et al., 2003; Stoy et al., 2013; Paleri, 2022) which corresponds to 3 km up to a few tens of kilometers (Stull, 1988, p.20, Mauder et al., 2007b). Over a homogeneous ground at a given

height, the flux magnitude brough by eddies revolving in long periods must be weak in order to satisfy continuity (Finnigan et al., 2003). In the SL, periods of large eddies in homogeneous conditions are limited to $u^*/z$ where $z$ is the measurement height, but over non-homogeneous terrain, the coupling of scalar concentration and wind direction can induce much lower frequency components (Finnigan et al. 2003, p.37).

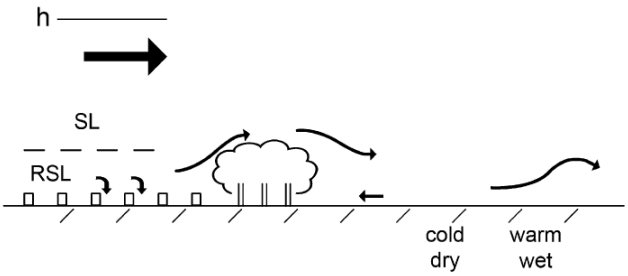


Figure 7: Schematic representation of obstacles that can create mesoscale motions in the surface layer (SL), with h the height of the boundary layer. Smaller obstacles lead to circulations that are bound to the roughness sublayer (RSL) (Mahrt, 2010)

Surface heterogeneities that can induce mesoscale motions include horizontal changes of surface roughness and albedo and local topography (Mahrt, 2010). Obstacles can also cause mesoscale motions, as long as their height is sufficiently important, compared to the depth of the boundary layer : only high obstacles such as forest edges can cause mesoscale motions in deep boundary layers, while smaller obstacles would lead to circulations bound to the roughness sublayer (RSL) (Fig. 7, Mahrt, 2010).

### 2.3.2 Evidence of mesoscale motions

Since the (co)spectral gap separates mesoscales from turbulent scales (e.g. Mahrt et al., 2001), XWT is commonly deployed to identify its location in the frequency domain, even though this task is uncertain because the cospectral gap might not occur (e.g. Mahrt 2010). The periods of the cospectral gap increases with thermal instability (Mahrt, 2001; Vickers and Mahrt, 2003) and measurement height (Saito and Asanuma, 2008; Vickers and Mahrt, 2003). In the following section, studies on mesoscale motions appearing during daytime are discussed.

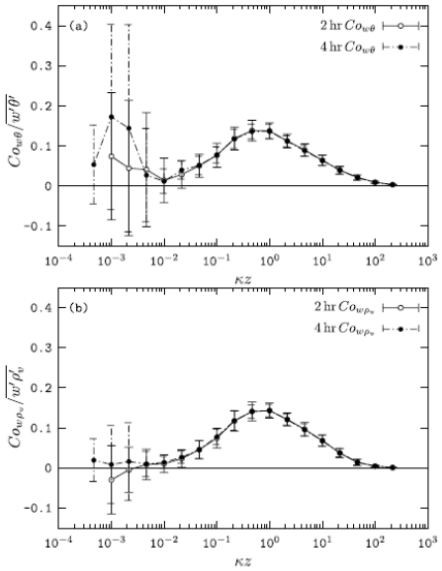


**Figure 2.** Bin-averaged wavelet cospectrum of (a) $\overline{w'\theta'}$ and (b) $\overline{w'\rho_v'}$. The open and solid circles are 2-hour and 4-hour data sets, respectively. The wavelet cospectra are normalized with the corresponding covariance. See the text for details. The error bars represent a standard deviation from the mean.

Figure 8: Wavelet cospectra of temperature flux and water vapor flux bin-averaged from over many record. The x-scale is the wavenumber (Saito et al., 2007)

Measurements made from towers have been deployed to identify mesoscale motions. Latent and sensible heat fluxes were calculated thanks to XWT from measurements at 6.3 m over a 1.2 m rice paddy field by Saito et al. (2007). Wavelet cospectra bin-averaged[2] over the whole experimental period revealed a gap at wavenumber of $10^{-2}$ [$m^{-1}$], which corresponds to approximately 20 minutes. In their study, significant contributions beyond the cospectral gap were only observed for sensible heat (see Fig. 8).

An example study over a homogeneous flat bar soil in this case – is that of Dupont (2019). On this site, 2.5-µm dust concentrations and wind speed were measured at 3 m and fluxes calculated thanks to XWT. Dust fluxes were calculated over the exceptionally long processing period of 18 hours and revealed a cospectral gap at 30 min (Fig. 9).

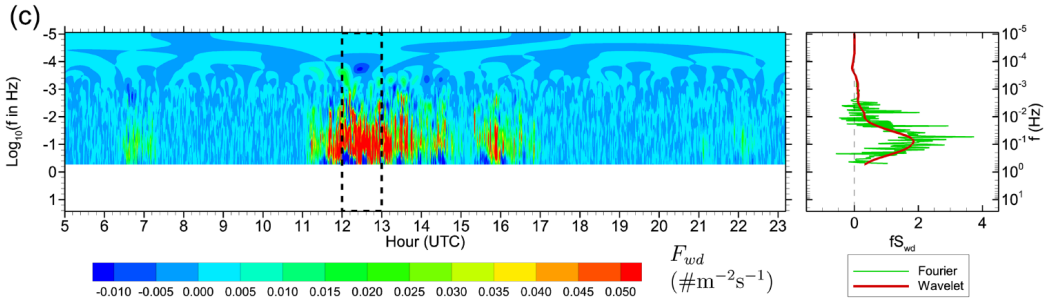


Figure 9: cross-scalogram and cospectrum of 2.5-µm dust flux over a flat bare soil (Dupont, 2019)

[2]Bin-averaging is the averaging of values over certain (e.g. one-hour long) bandwidths and potential taking data from more than one time-series. For example, the one-hour bin-averaged value of temperature at 09:00 could be the average of temperature measurements from 08:30 to 09:30 from day 1 to day 3

Von Randow et al. (2002) calculated fluxes of $CO_2$, water vapor and temperature made at 62 m above a 32-meter high patchy forest canopy. Taking many 4-hours long record periods from several different days, flux values were calculated according to wavelenghts [m] with a discrete WT. The standard deviation between flux at the same wavelenght but from different records allowed to analyze boundary layer processes. Normalizing the standard deviation of fluxes at each scale by the mean value of flux at the respective scale showed that the variation between records is constant and small in scales below 1000 m, but there is a large variation at bigger scales (Fig. 10).

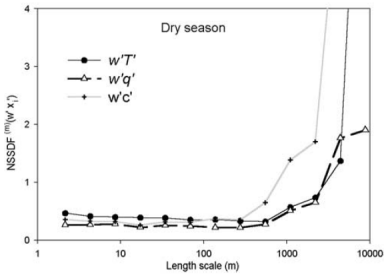


Figure 10: Normalized standard deviation of the fluxes computed at each scale but from different records, with respect to the wavelenght of the oscillation (Von Randow et al., 2002)

This highlighted that on the study site, two different boundary layer regimes govern fluxes in separate scale ranges. The separation of these two regimes occurs at a scale of 800 m, which is related to a period of 6.5 minutes. All three scalars ($CO_2$, latent heat and sensible heat) had 30% of flux contributions that exceeded the cospectral gap.

The analysis led by Foken et al. (2006a) and Finnigan et al. (2003) are exceptional examples of the study of mesoscale motions performed with EC with extended averaging time. (up to 12 hours). Despite the difficulties they encountered in the selection of data, the obtained cospectra are comparable to those yielded with XWT and their results are valuable to the present study. The analysis of Foken et al. (2006a&b) computed ogives in periods of revolution up to 2 hours for momentum, sensible and latent heat flux over maize field. They found that in around 85% of cases, the ogive stabilized for periods > 30 min. In the remaining 15% of cases, the ogives continued to vary towards an increase or a decrease of the total flux. They concluded that in the case where the ogive does not converge for periods <= 30 min, the averaging time should be extended. The three typical cases of ogives are illustrated in Fig. 11.

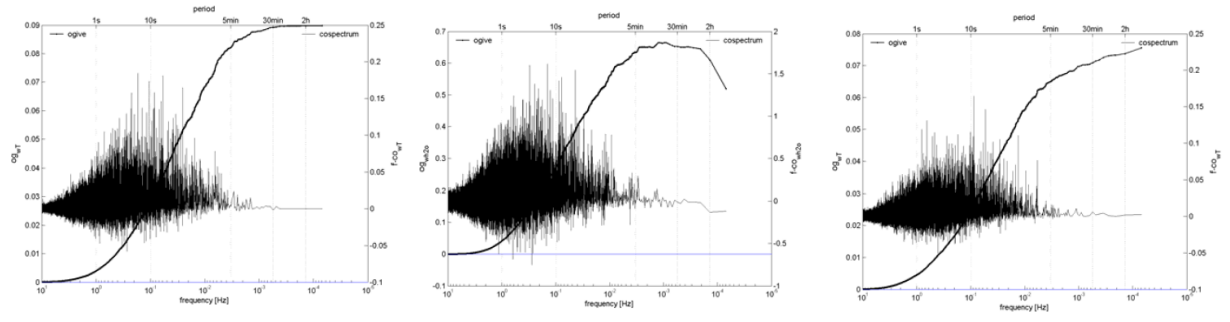


Case 1 Case 2 Case

Figure 11: Typical cases of an ogive converging within 30 min (Case 1), showing a maximum and decreasing (Case 2) and continuously increasing (Case 3)

On the other hand, flux cospectra obtained with averaging up to 12 hours in a spatially homogeneous forest (a) and two forests with complex topography (b and c) stemming from the study of Finnigan et al. (2003) are depicted in Fig. 12. The forest land cover was homogeneous on the three sites, so the heterogeneities are assumed to be mainly due to relief.

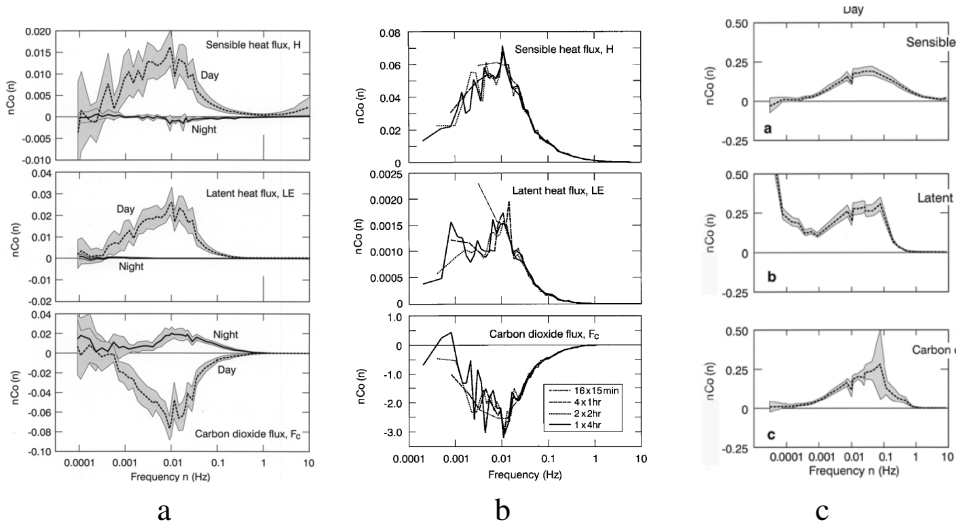


Figure 12: Cospectra of sensible heat, latent heat and $CO_2$ for a spatially homogeneous site (a) and two sites with complex topography (b and c) (Finnigan et al., 2003)

Mesoscale motions have also been investigated with aircraft measurements, which bring an insight of the spatial scales of mesoscale motions. The study of Mauder et al. (2007a) computed wavelet cospectra for fluxes of sensible and latent heat, $CO_2$ and $O_3$ over a Canadian boreal forest with lakes. The cospectra show that components larger than 2 km have lower magnitudes and seem to vanish for high wavelengths (Fig. 13). The components larger than 2 km represented flux contributions on the order of 10-30%, but varied among scalars and flights, so the closure could not be attained.

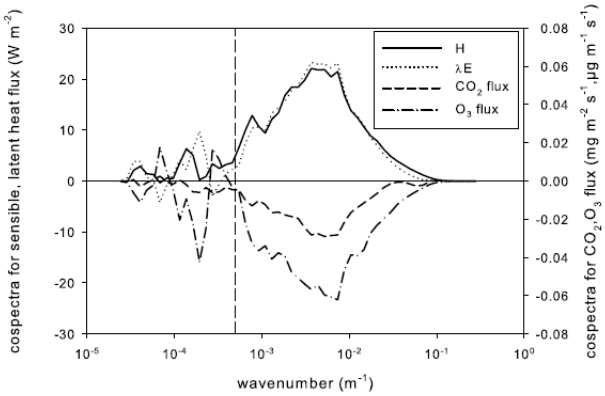


Figure 13: Wavelet cospectra for fluxes of sensible and latent heat, $CO_2$ and $O_3$ computed from aircraft measurements and presented with respect to the wavenumber $\kappa$ [$m^{-1}$]. The vertical dashed line is placed at a wavelength of 2 km and shows the spectral gap (Mauder et al., 2007a)

The study of Paleri et al. (2022) investigated mesoscale motions from aicraft measurements from the CHEESEHEAD19 campain. The main part of the spectral energy was contained in wavelenghts of 2 - 10 km, and the cospectra did not show any energy in wavelenghts larger than 10 km (Fig. 14).

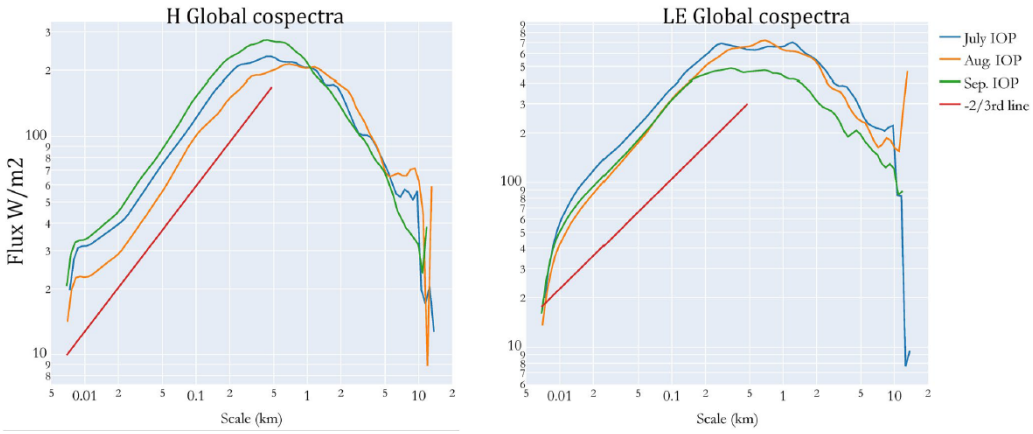


Figure 14: Bin-averaged flux cospectra of sensible (left) and latent (right) over each intensive observation period (IOP) computed from measurements of the CHEESEHEAD19 campain (Paleri et al., 2022)

## 2.4 Study sites

The data used for this work stems from two ICOS-labelled sites in the Walloon Region in Belgium. The first study site (named BE-Lon in ICOS referencing system), is a cropland situated in the province of Namur in the municipality of Lonzée (50°33'05.7"N 4°44'46.1"E; 170 m above sea level). The parcel on which the tower is situated is approximately 400 m x 400 m wide, and is surrounded by parcels of comparable or smaller sizes. The wind predominantly comes from the South-West. On this site, the EC measurement system is mounted at 2.1 m above-ground.

The second study site (BE-Vie) is a mixed forest situated in the province of Liège (50°18'N, 6°00'E, altitude: 450 m) in the municipality of Vielsalm. The relief is hilly and there is a 3% slope in the Northwesterly direction (Aubinet et al., 2001). The tower is situated at the edge of the forest, and is surrounded by forest crossed by traffic routes on the South and by a few meadows in the North.The canopy surrounding the tower is on average 35 m high and the eddy covariance system is placed at 51 m above-ground (ICOS system labelling report BE-Vie, 2020). The satellite views of Fig. 15 and Fig. 16 show the area at the spatial scale of turbulent motions (3 km) as defined by Stull (1998).

On both sites, the eddy-covariance system is compatible with standards of the EUROFLUX network (Sabbatini and Papale, 2017) and consists of an infrared gas analyser (IRGA) (Model LI-7200, LI-COR Inc., Lincoln, NE, USA) and a three-dimensional sonic anemometer (Model HS-50, Gill Instruments, Lymington, UK) (ICOS, 2020). Additional information on the instrumental set-up can be found in the ICOS reports and in Aubinet et al. (2001). In the present work, measurements made at a 20-Hz frequency have not been subjected to any corrections such as despiking, coordinate rotation, correction for high-frequency losses, etc.

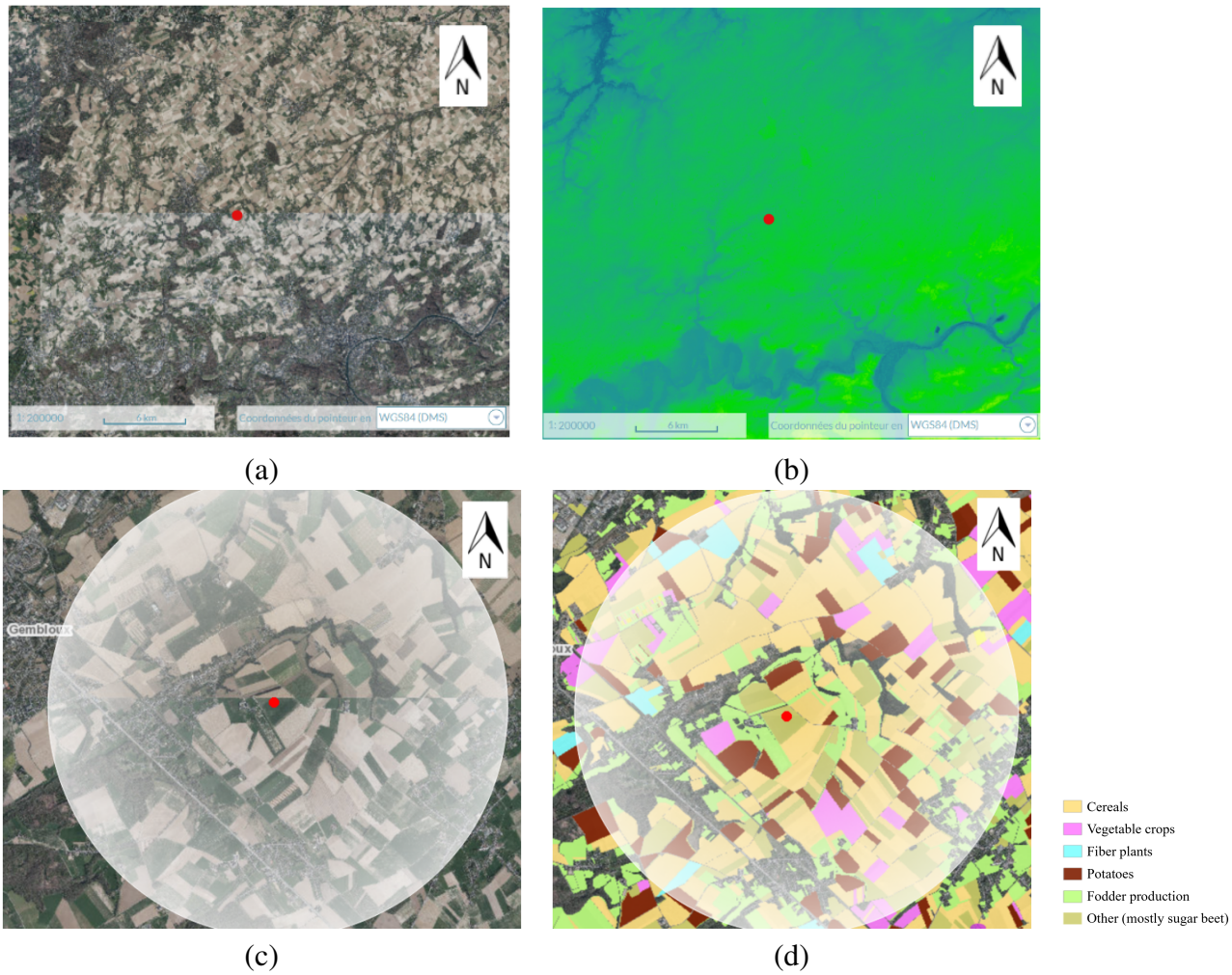


Figure 15: Top : Land cover (a) and topography (b) at the mesoscale in Lonzée in 2020. The tower is situated at the red arrow and the landscape is shown in the main upwind direction. Bottom : Land cover (c) and cultural type (d) at the turbulent scale in Lonzée in 2020. The tower is situated at the red dot and the white circle shows a radius of 3 km around the tower (own production)

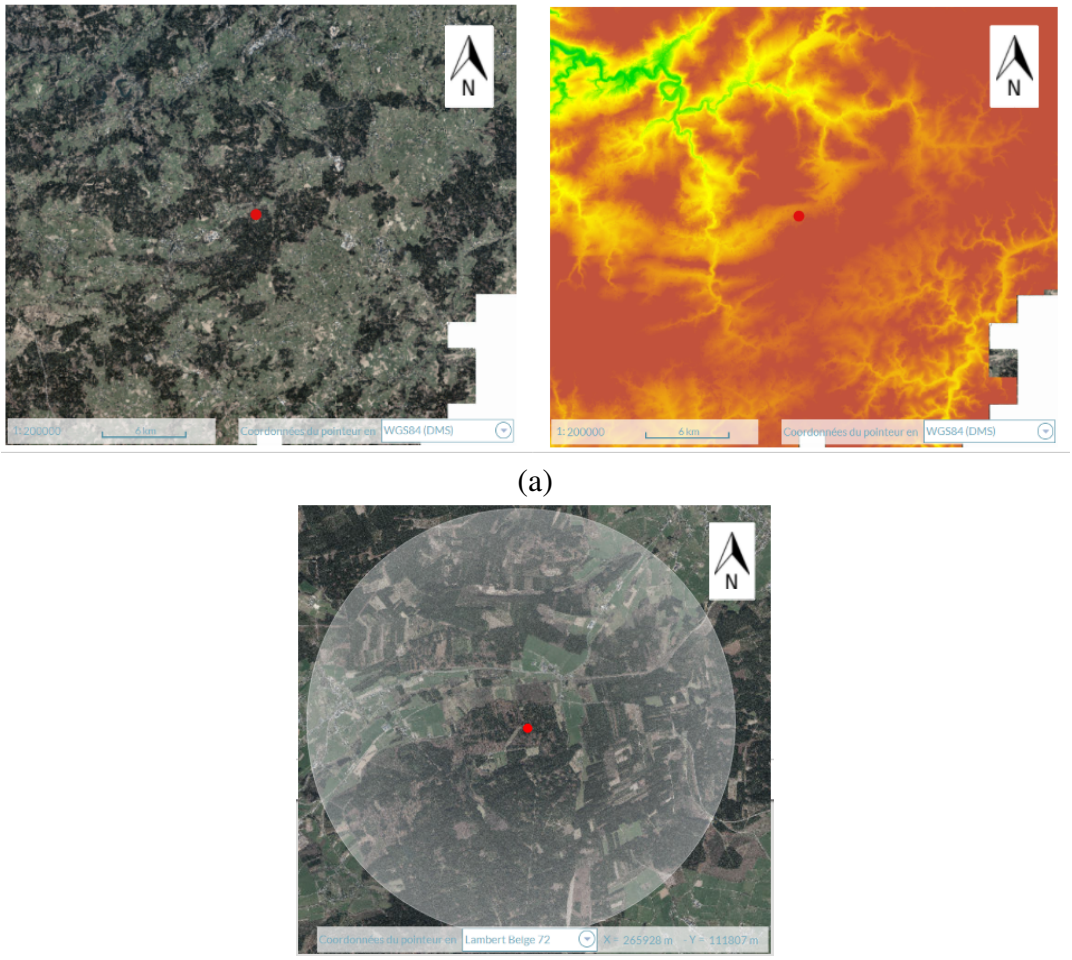


(a)

(b) (c)

Figure 16: Land cover in Vielsalm in 2022 at the mesoscale (a) and land cover at the turbulent scale (b). The tower is situated at the red dot and the white circle shows a radius of 3 km around the tower

# 3 Methods

In this section, the methods necessary to attain the two research objectives are presented subsequently. For the first objective, presented in 3.1, no particular criteria of data selection was required, except for the absence of gaps and measurement errors. Contrary to that, the second research objective required careful data selection, so the data selected for the second objective was also used to carry out the first objective, since it was perfectly suitable for it. However, since the criteria for the selection are inherent to the second objective, they will be presented along with it in 3.2.

## 3.1 Parametrization of the XWT

### 3.1.1 The wavelet transform

Wavelet decomposition happens through the convolution of the signal the convolution with an analyzing function. WT exists in both a discrete and continuous version, and while the first demands

less computation power, the latter is better adapted to measure the contribution of turbulent structures at different scales and to detect the singularities of signals measured in the atmosphere, not only because it yields a continuous, fine-resolved graphics, but also because of its redundant properties (Farge, 1992, p. 3).

The general formula of the continuous WT, which is a convolution between the measured signal $x(t)$ and the analyzing function writes:

$$T_x(a,b) = \int_{-\infty}^{+\infty} x(t)\psi^*_{a,b}(t)dt \tag{15}$$

Where :

- $T_{a,b}$ are the wavelet coefficients depending on the parameter of scale (a) and time (b)
- $\psi_{a,b}(t)$ are the daughter wavelets, deduced from the analyzing function $\psi$ and depending on a scaling parameter (a) and on the localisation in time (b) and * denotes the complex conjugate

The daugther wavelets $\psi_{a,b}(t)$ are obtained by translation (b), dilation (a) and normalization ($\lambda$) of the mother wavelet $\psi$ according to :

$$\psi_{a,b}(t) = \lambda_{norm}\psi\left(\frac{t-b}{a}\right) \tag{16}$$

The set of scales $a_j$ that dilate the daughter wavelets can be chosen arbitrarily for continuous WT, and here they are chosen according to Torrence and Comp (1998) :

$$a_j = a_0 2^{j\delta j}, \quad j = 0,1,...J \tag{17}$$

Where $a_0$ is the smallest analyzed scale, and $J$ determines the largest scale and is chosen as (Torrence and Compo, 1998) :

$$J = \delta j^{-1} log_2(\frac{N\delta t}{a_0}) \tag{18}$$

The factor $\lambda_{norm}$ depends on the chosen normalization, and impacts the graphical representation of wavelet coefficients. A normalization in $L^2$ implies that the daughter wavelets conserve the energy of the mother wavelet such as (Bitton, 2019):

$$||\psi_{a,b}(t)||^2 = ||\psi(t)||^2 = \int_{-\infty}^{+\infty} |\psi(t)|^2 \, dt \quad \Leftrightarrow \quad \lambda_{norm} = a^{-0.5} \tag{19}$$

In practice, a normalization in $L^2$ attributes a greater amplitude to small-scale coefficients. With this normalization, the energy density at different scales can be compared, but the amplitude cannot. Further, it is common to set the $L^2$ normalization for unit energy, which implies that the terms in Eq. 19 are equal to 1.

In a similar manner, $\lambda_{norm}$ can be computed in $L^1$ normalization assuming that:

$$||\psi_{a,b}(t)|| = ||\psi(t)|| = \int_{-\infty}^{+\infty} |\psi(t)| \quad \Leftrightarrow \quad \lambda_{norm} = a^{-1} \tag{20}$$

The $L^1$ normalization attributes similar ranges of values for all scales, and it is suitable to compare the scaling properties of wavelet coefficients of different scales (Farge, 1992, p. 415).

Comparison of the $L^1$ and $L^2$ for the Morlet wavelet is shown in Fig. 17.

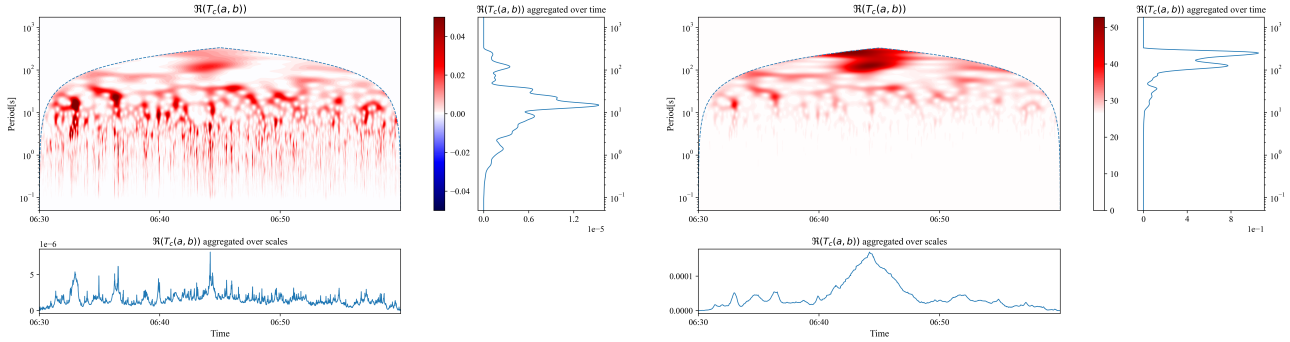


a b

Figure 17: Comparison of cross-scalograms for the same signal with the normalization $L^1$ (a) and $L^2$ (b). The plot on the right and on the bottom show $T_c(a,b)$ aggregated over time and over scales

To be able to compare the amplitude at different scales, wavelet coefficients can be "renormalized" (Farge, 1992, p.3) by dividing $T_x(a,b)$ by the respective scale $a$, which gives a similar aspect to the cross-scalograms in $L^1$ and $L^2$.

### 3.1.2 Mother wavelets

For the analysis of turbulent flow, one of the most commonly used wavelets is the Mexican hat, and its function writes:

$$\psi(t) = (1-t^2)e^{-\frac{t^2}{2}}$$

It has an good resolution in the time domain (Schaller et al., 2017) and is suitable to detect coherent structures such as ramps (Steiner et al., 2011). The Morlet wavelet is the other frequently used one:

$$\psi(t) = e^{-jw_0 t} e^{\frac{-t^2}{2}} \tag{21}$$

where $w_0$, called the based frequency even though it is adimensional (Terradellas et al., 2001) and is often set to 6 (Farge, 1992). The Morlet wavelet better known for its good frequency resolution (Schaller et al., 2017) and its complex part is suitable for e.g. the analysis of phase shift between two signals (Farge, 1992, p.406), the direction and the phase speed of turbulent oscillations (Terradellas, 2001).

The normalization factor $K$ is specific to each wavelet, and can be derived from Eq. 19 and 20 by replacing $\psi(t)$ by its expression. For example, the factor $K$ for a unit-energy normalization gives of the Morlet wavelet (Bitton, 2019): $K = \left(\sigma^2\pi\right)^{-\frac{1}{4}}$. Fig. 18 shows a comparison of WT with Morlet and Mexican hat normalized in $L^1$.

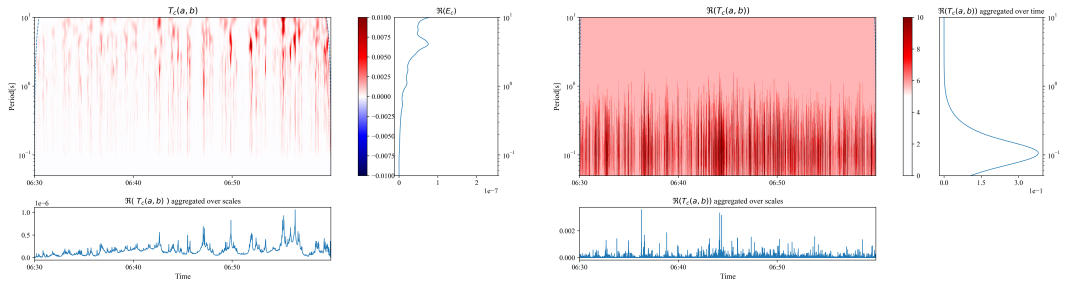

Morlet Mexican hat

Figure 18: Comparison of WT with the Morlet and the Mexican hat wavelet performed on the same signal. For each wavelet, the cross-scalogram, cospectrum (right) and wavelet cross-coefficients aggregated over time (bottom) are shown. The COI is outside of the plot

For analytical purposes — such as the calculation of covariance — it is advised that the shape of the wavelet (see Fig. 5) resembles the features of the signal : smoothly varying time-series such as those of wind velocity and carbon concentration are better analyzed by damped cosines such as the Morlet wavelet (Torrence and Compo, 1998). For the analysis of wavelet cospectra however, the choice of the mother wavelet does not matter, since all wavelets should render qualitativavely accurate results (Torrence and Compo, 1998).

### 3.1.3 Cone of influence

With wavelet decomposition, the maximal period of oscillation that can be interpretated is not directly equal to the averaging time. Indeed, wavelet coefficients at the borders of the signal are contaminated by the discontinuities at these borders and should not be interpretated. The cone of influence (COI) defines the regions of the scale-time domain where the edge effects are estimated to be important (Torrence and Compo, 1988). The width of the COI is defined as the distance in the time-domain at which the power of a wavelet coefficient $|T^2(a,b)_x|$ yielded by a peak at a certain time $t$ decays by a fraction $qcoi$ of its peak magnitude (Kirby and Swain, 2013). The COI can be visualized by simulating Dirac implusions at the borders of an otherwise silent time-series (Bitton, 2019). Fig. 19 shows the cross-scalogram of such an artificial time-series as well as the limits of the COI defined for $qcoi = 0.02$ and $qcoi = e^{-1}$.

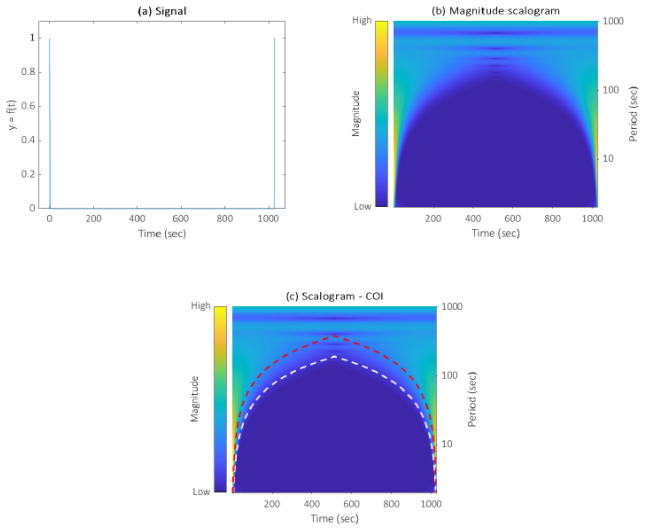


Figure 19: Artificial time-series constant at 0 with Dirac impulsions at its left and right borders (a), magnitude of the wavelet coefficients of the Dirac implusions visualized in the cross-scalogram of the artificial time-series (b) and limits of the COI fo $qcoi = e^{-1}$ (red) and $qcoi = 0.02$ (white) plotted in the cross-scalogram (Bitton, 2019)

For the calculation of covariance, it imports to exclude the values beyond the COI border, since they might contain spurious components (Mauder et et al., 2007a; Herig Coimbra, 2023, personal communication).

### 3.1.4 Formula of spectrum and covariance

The continuous formulas for the average variance of wavelet coefficients over the whole record period have been adapted for discrete signals under the $L^2$ normalization by Torrence and Compo in 1998. Later, Schaller et al. (2017) adapted the formulas of Torrence and Compo in order to calculate the wavelet cross-spectrum $E_{wc}(j)$ of the flux, analogous to the Fourier cross-spectrum. By taking the measured signals of vertical wind velocity $w$ $[ms^{-1}]$ and another scalar (temperature $[°C]$, $CO_2$ or $H_2O$ $[\mu mol_{gas} mol_{air}^{-1}]$), the flux cross-spectrum writes:

$$E_{wc}(j) = \frac{\delta t}{C_\delta} . \frac{1}{N} \sum_{n=0}^{N-1} [T_w(a_j, b_n) . T_c^*(a_j, b_n)] \tag{22}$$

where,

- the product $[T_w(a_j, b_n) . T_c^*(a_j, b_n)]$ constitutes the wavelet cross-coefficients
- $\delta t$ is the time step, which is the duration escaped between two values of the signals. It is 0.05 s since the sampling frequency of the sensors is 20 Hz.
- N is the number of values composing a signal
- $C_\delta$ is a constant depending only on the chosen wavelet, that was primarily derived for the reconstruction of the signal from wavelet coefficients. Torrence and Compo suggest a value of 3.541 for the Mexican hat wavelet and 0.776 for the Morlet wavelet, however successive deconstruction and reconstrution has shown that the value of 0.7784 is more accurate for the latter and it is this value that is used in the present analysis.

The cospectrum, i.e. the real part of the cross-spectrum (Stull, 1988, p. 331) can be "renormalized" (Farge, 1992, p.441) by dividing by the respective scales and multipling by $dt$, and then aggregating over all scales to yield the average covariance over the record period according to Schaller et al. (2017) :

$$Cov_{XWT} = \overline{w'c'} = \mathfrak{Re}\Big[ \frac{\delta t}{C_\delta} . \frac{\delta j}{N} \sum_{j=0}^{J} \sum_{n=0}^{N-1} \frac{[T_w(a_j, b_n).T_c(a_j, b_n)^*]}{a_j} \Big] \tag{23}$$

where $Cov_{XWT}$, is analogous to $Cov_{EC}$ and is expressed in the same units, which is the product of units of both signals ([µmol$_{CO_2}$.mol$_{air}$.m.s$^{-1}$] for $CO_2$ and [°C.m.s$^{-1}$] for temperature). The equation can be adapted to the $L^1$ normalization by alleviating it from the renormalization factors, that is, by eliminating the factor $\delta t$ and not dividing by the respective scales $a_j$. For the calculation of covariance to be unaffected by edge effects, the values above the COI border should be discarded in the coefficients of Eq. 23 (Mauder et al., 2007a).

### 3.1.5 Choice of scaling factors

For a given wavelet and normalization, the parameters of the XWT that affect the $Cov_{XWT}$ are the scale step δj, and the minimal period of oscillation that is analyzed Period$_{min}$, and the threshold limiting the maximal analyzed period *qcoi*. Additionally, artificial values can be added at the beginning and at the end of the original signals to diminish edge effects (Meyers et al., 1993), and such "padding" or "buffering" could have an influence on the value of covariance. The padding values can be zeros (further referred to as *zpd*) or can mirror the values of the signal by duplicating borders (*sym*) or not duplicating them (*symw*).

Since EC is the benchmark for calculation of the turbulent flux for stationary half-hour records, the parameters of the XWT have to adjusted so that the $Cov_{XWT}$ (Eq.23) matches $Cov_{EC}$ (Eq. 11) for such data as in Schaller et al. (2017) and Dupont (2019). A sensitivity analysis will be conducted by testing different values of one parameter of the XWT while the other remain constant. The dataset is constructed as such : half-hourly records of temperature and $CO_2$ from Lonzée (stemming from the dataset constructed for the second research objective as explained in 3.2.2) were tested with three stationarity tests, as prescribed by Fortuniak et al. (2013) :

- Foken and Wichura (1996) (FW),
- Mahrt (1998) (MA),
- Dutaur et al. (1999) (DU), later revised by Nemitz et al. (2002)

The equations of these tests are expanded in Appendix 8.3. The records selected for the analysis are those evaltuated as stationary according to the threshold values advised in the papers (also presented in Appendix 8.3).

To compute the covariance, the Morlet mother wavelet normalised in $L^2$ is chosen since it is frequently used to computate of flux cospectra (Mauder et al., 2007a; Schaller et al., 2017). The starting value of $\delta j$ is 0.25 from Mauder et al. (2007a). The restrictiveness of the COI, defined by the threshold *qcoi* is set to 0.10, which is a compromise between the value $qcoi = e^{-1}$ proposed by Torrence and Compo (1998) and the value $qcoi = 0.02$ proposed by Nobach et al. (2007). Period$_{min}$ is expressed relative to the the time step $\delta t$ and as a start, it is set to $\delta t$, which is the finest resolution possible since

it does not make sense to look for oscillations smaller than that. Starting and tested values of these parameters are summarized in Table 1.

Table 1: Starting values and tested ranges of parameters for the parametrization of the XWT. Acronyms are explained in the text

| | Starting value | Tested values |
|---|---|---|
| $\text{Period}_{\text{min}}$ | $\delta t$ | $[1:20]\ \delta t$ |
| $\delta j$ | 0.25 | $[0.03:0.95]$ |
| Padding side | both sides | {none, right side, both sides} |
| Padding values | zeros | {none, *zpd*, *sym*, *symw*} |
| *qcoi* | 0.10 | [0.02:1] |

The $Cov_{XWT}$ and $Cov_{EC}$ are computed for all half-fours that are analyzed and the relative error $\varepsilon$ of the $Cov_{XWT}$ compared to the $Cov_{EC}$ is calculated as follows:

$$\varepsilon = \left| \frac{Cov_{XWT} - Cov_{EC}}{Cov_{EC}} \right| \tag{24}$$

### 3.1.6 Choice of the mother wavelet

The mother wavelet and the normalization are chosen jointly. $Cov_{XWT}$ is calculated with Mexican hat and the Morlet wavelet, and these wavelets are tested with the normalizations $L^1$ and $L^2$. The acronyms of each option are the conjunction of the wavelet and the normalization (e.g. MEXL1 stands for Mexican hat, normalized with $L^1$). For all four options, the parameters of the $Cov_{XWT}$ are equal and set according to the results of the analysis of the scaling parameters. In the same way as for 3.1.5, the relative error is calculated with each option for the 238 half-hours according to Eq.24, which allows to compare the four options.

## 3.2 Analysis of mesoscale motions

### 3.2.1 Graphical representation

Wavelet cross-coefficients are obtained by performing WT with the signal of $w$ and another scalar, either temperature, $H_2O$ or $CO_2$ atmospheric concentration, with the wavelet and the values of parameters selected in section 3.1.

Different graphical representations and then produced from the coefficients, which allows to analyze particular aspects. The real part of wavelet cross-coefficients are displayed in cross-scalograms, where they are they are displayed in the time-frequency domain. The wavelet scales $a_j$ (Eq. 17) are converted into the equivalent period of oscillation or "Fourier period" $\lambda_j$ following Bitton (2019) :

$$\lambda_j = \frac{2\pi}{w_0} a_j \tag{25}$$

for the Morlet wavelet, and

$$\lambda_j = \frac{2\pi}{\sqrt{\frac{5}{2}}} a_j \tag{26}$$

for the Mexican hat wavelet.

The flux cospectra, i.e. the real part of $E_{wc}(j)$, are presented by summing the absolute values in Eq. 22, which prevents the canceling of components of opposite signs and thus allows to visualize all components at each $a_j$. The cross-wavelet coefficients for an entire day (09:00 - 16:00 UTC+1) were also used to calculate ogives by successively integrating $Ewc(j)$ over periods $dp$ from the lowest period of revolution to higher ones, spaced by 100 seconds and ranging up to 3.2 hours (11 500 s) :

$$Og_i = \int_0^i \Re(Ewc)\, dp \quad ; \quad i \in \{100, 200, 300, ..., 11500\}\ [s] \tag{27}$$

Contrary to the cospectra, the ogives are calculated directly over the real part of wavelet coefficients; without an absolute value, so that the actual value of flux is expected to be found at the end of the high-period end of the integral. The graphs of the ogives are displayed respective to the oscillation period in logarithmic scale as in Foken et al. (2006a&b).

### 3.2.2 Data selection

The data for the computation of wavelet cross-coefficient was carefully selected in order to meet the second research objective. As a reminder, this objective is to identify mesoscale components that could explain the SEB unclosure and that are not linked to turbulence intermittency but to other phenomena. As said previously, SEB unclosure is most problematic during the day, which is also when and turbulence is better developped, since insolation and thermal starification are most developped. For these two reasons, fluxes will be computed from 9:00 to 16:00 local time (UTC+1) during the warm season, which stretches between June and September in Belgium. An additional reason to choose data within these months is that the vegetation responsible for photosynthesis and respiration is well-developed, which serves as strong sources and sinks of $CO_2$. To eliminate potential causes of turbulence intermittency, cloudless days are specifically chosen by analyzing the graph of incoming solar radiation, which exhibits a characteristic Gaussian shape on such occasions. Furthermore, to account for potential variations in mesoscales due to wind direction (Inagaki et al., 2006; Prabha et al., 2007b), two distinct sets of data are selected for each site, with each set featuring a different wind direction. Also, the wind direction is deliberately chosen to be stable throughout the day to prevent turbulence intermittency caused by changes in wind direction. Gaps and measurement errors are also avoided in order to refrain from the need of gap-filling methods.

### 3.2.3 Choice of the averaging time

With wavelet decomposition, the maximal period that can be analyzed depends on the COI, and thus on the threshold *qcoi*. This implies that the averaging time has to be extended a lot more than the maximal period that is wished to be analyzed. For the analysis of mesoscale components, the cross-scalograms are computed for values under the COI with a threshold $qcoi = e^{-1}$, since this is the heighest thereshold that was found in literature (Torrence and Compo, 1988).

The maximal analyzed period was determined based on computational constraints. To save computational power, matrices of wavelet coefficients are computed over periods of 14 hours before being cropped, and only a portion of 1 hour (in the time domain) is kept in the middle of the matrix, since in the middle of the matrix the COI border is highest. As a consequence, spikes and measurements gaps have to be avoided in approx. 7 hours before and after the period of interest. These time-series are used to compute wavelet coefficients, without any change of units.

# 4 Results

## 4.1 Parametrization of the XWT

### 4.1.1 Scaling parameters

The selection process (section 3.1) generated a dataset of 238 stationary half-hours that were used to calculate $Cov_{XWT}$, $Cov_{EC}$ and the $\varepsilon$. The accuracy (i.e. is the systematic bias of the estimation with respect to the real values, Mercatoris, 2021) of the $Cov_{XWT}$ with respect to the $Cov_{EC}$ is statistically represented by the mean error $\langle\varepsilon\rangle$, plotted in red in Fig. 20. On the same figure, the scatter plot of the 238 individual values gives an idea of the precision (i.e. the degree of deviation around this average value (Mercatoris, 2021). The separation of these quality indicators is important, for example because the scatter is smallest for $qcoi \in [0.02, 0.10]$ but the accuracy is best for $qcoi = 0.22$ ($\langle\varepsilon\rangle = 0.099$), which represents an error reduction of 2.3% compared to the maximal mean error attained for $qcoi = 0.35$ ($\langle\varepsilon\rangle = 0.128$).

The trend followed by $\langle\varepsilon\rangle$ according to the minimal period is different, since $\langle\varepsilon\rangle$ increases steadily by 5% (from 0.10 to 0.15) when the $\text{Period}_{\text{min}}$ increases. The precision degrades and the mean error increases by 7% (from 0.10 to 0.17) when $\delta j$ is increased from 5 $\delta t$ to 20 $\delta t$, but accuracy and precision are only slightly affected when $\delta j$ is less than 5 times greater than $\delta t$. A factor of five means that $\delta j = 5 \cdot 0.05 = 0.25$, which is the value Mauder et al. (2007a) suggested to use. Regarding the padding, zero-values provide larger errors compared to both types of symmetrical padding and even compared to no padding at all. The no-padding option provides only slightly degraded results (mean error increases by less than 0.1%) compared to the symmetrical padding, which is the option provide the best accuracy. Throughout all the options of padding values, the side of the padding does not seem to have any influence on the results.

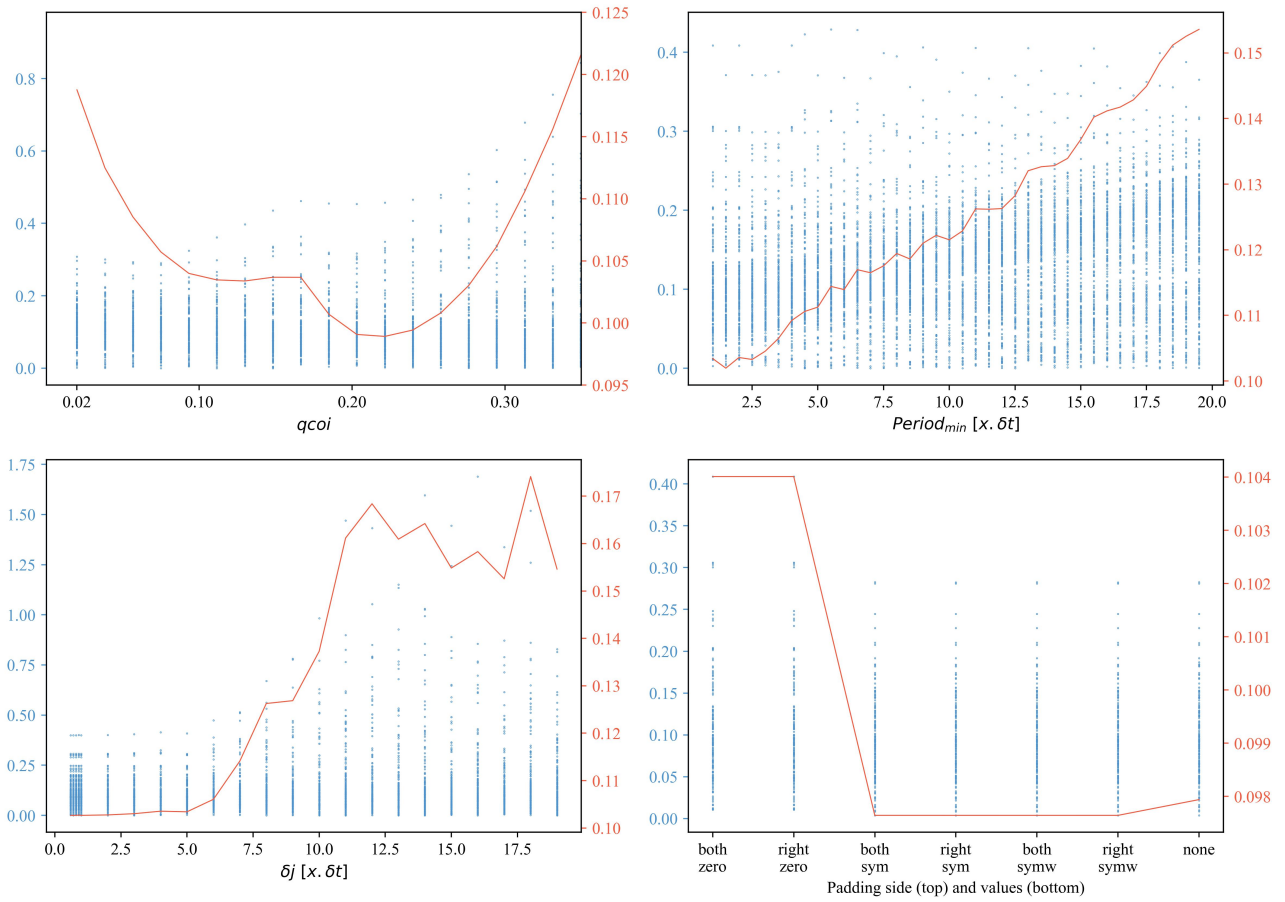


Figure 20: Relative error as in Eq.24 (left blue y-axis) with respect to values of $qcoi$, $\text{Period}_{\text{min}}$ and $\delta j$ (both expressed as a factor multiplying $\delta t$) and padding modes (refer to the text for their signification). The right y-axis (red) shows $\langle \varepsilon \rangle$, the relative error over all instances in a scale that is exagerated compared to scale of the left axis

These results allow to determine the adequate values of the parameters that will be retained for the choice of the mother wavelet. The retained values are the following :

- $\text{Period}_{\text{min}} = \delta t$ is retained since it minimizes the error.
- the value of $qcoi = 0.10$ is kept since it is renders a small $\langle \varepsilon \rangle$ and also a small scatter, unlike the value $qcoi = 0.22$ that only optimises $\langle \varepsilon \rangle$.
- $\delta j = \delta t = 0.05$ is set, because this value is sufficiently far from 0.25, which is the threshold value and if $\delta j$ is increased more than that, the mean errors increases.
- No padding is applied since this option leads to a good accuracy and requires less computational power compared to other options.

### 4.1.2 Wavelet and normalization

$Cov_{XWT}$ was parametrized according to section 4.1.1. Histograms of the relative errors show that the Morlet wavelet, normalized in $L^1$ is the best option, since (1) the most represented range of error for this option (0-10%) is smaller than for other options (2) other ranges of errors are regrouped around

the 0-10% class, while errors of the Mexican Hat seem randomly distributed among error ranges. For this reason, the MORL1 option is retained for the analysis of the second objective.

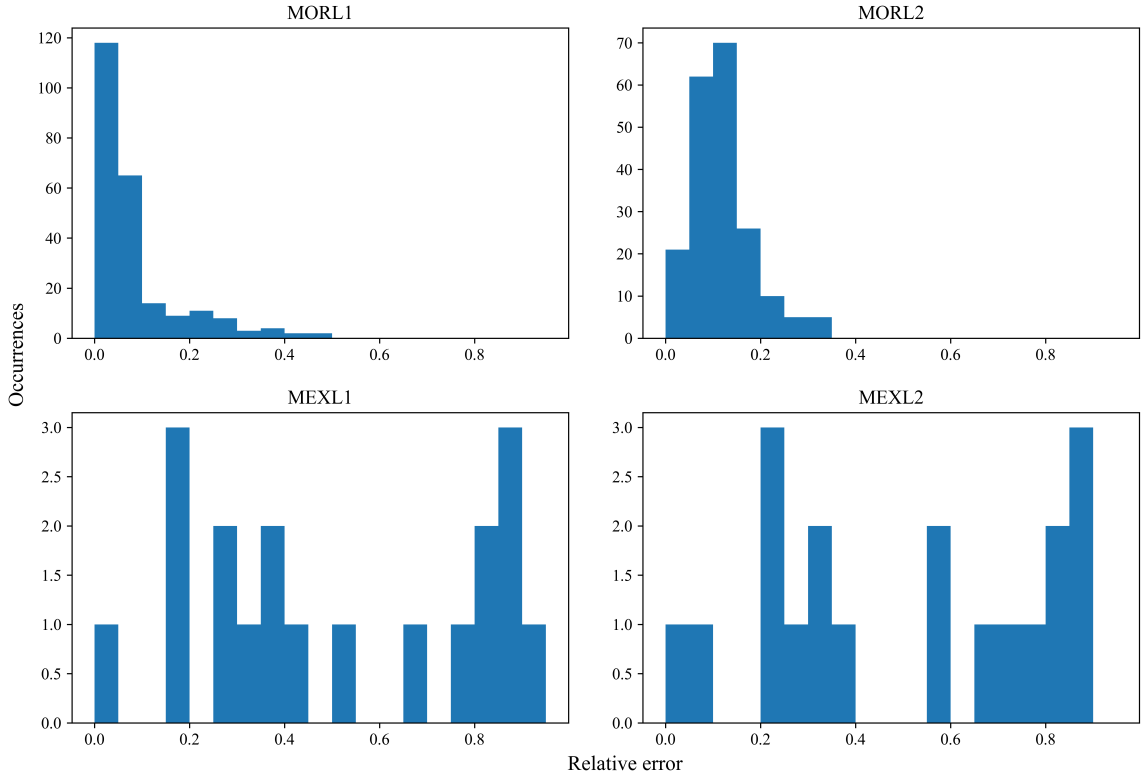


Figure 21: Histograms of relative error in Eq.24 of the $Cov_{XWT}$ calculated with two mother wavelets Morlet and Mexican hat and normalization $L^1$ and $L^2$). The parameters for the wavelets are chosen from section 5

## 4.2 Analysis of mesoscale motions

### 4.2.1 Selected data

Two periods of 24 to 48 hours featuring cloudless days with constant solar insolation and stable wind direction were found on each site of Lonzée and Vielsalm. The graphs of wind direction and incoming solar insolation are displayed in Fig. 22, where it can be seen that the solar insolation follows a Gaussian shape and that the wind direction is stable for the selected period.

The time-series of vertical wind velocity $[m.s^{-1}]$, $CO_2$ and $H_2O$ concentration $[\mu mol_{gas}.mol_{air}^{-1}]$, and temperature $[°C]$ are presented in Fig. 23. Displayed is the window of interest (09:00 to 16:00 UTC+1) as well as 7 hours before and after it : the wavelet coefficients are computed over periods of 14 hours before being cropped, with only 1 hours that kept in the middle in order to avoid edge effects. As a consequence, spikes and measurements gaps have to be avoided in approx. 7 hours before and after the period of interest. These time-series are used to compute wavelet coefficients, without any change of units.

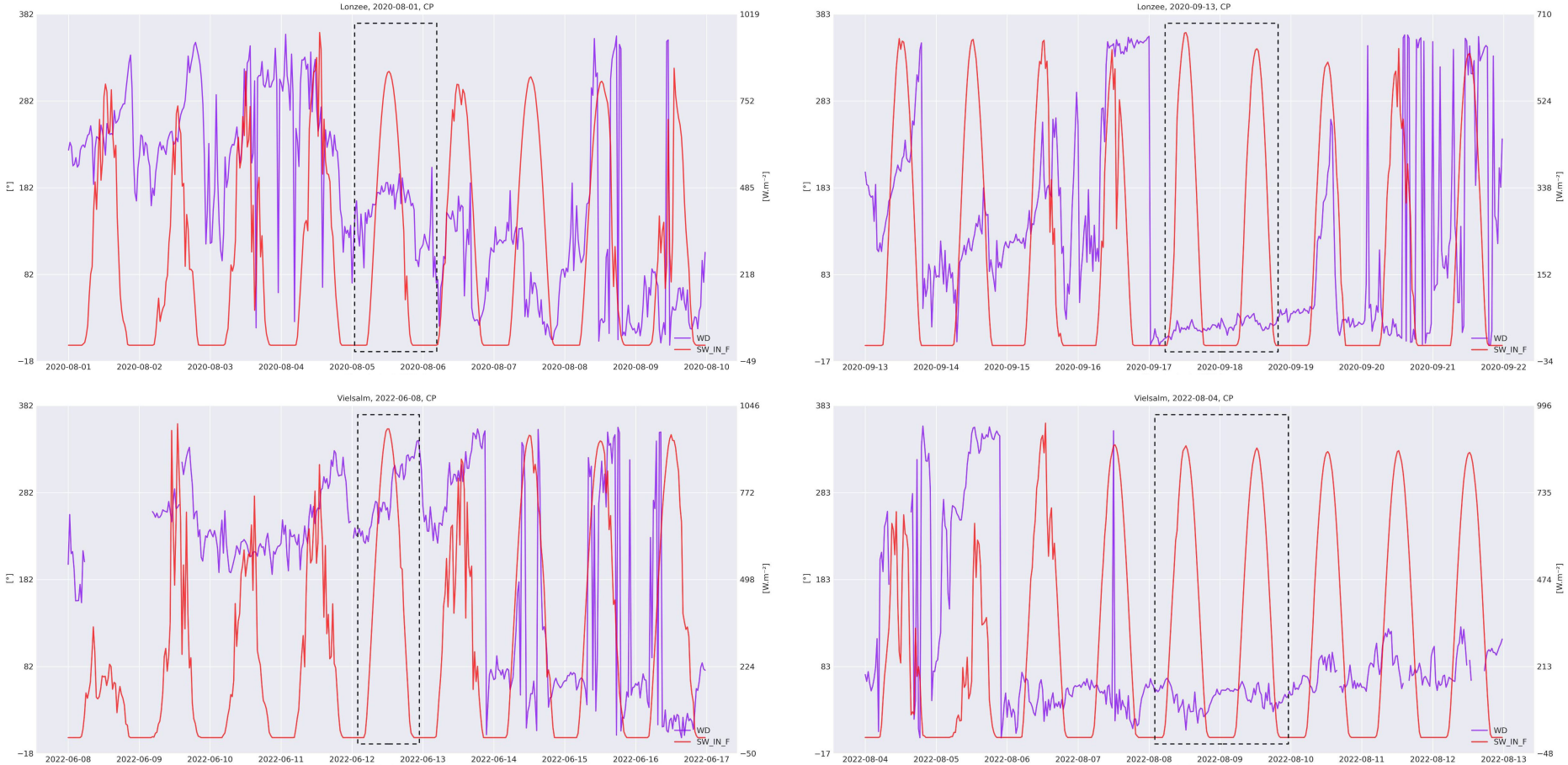


Figure 22: Selected ranges of data according to the criteria mentioned in section 2.4 in Lonzée (upper row) and Vielsalm (lower row). The wind direction is plotted in degrees in violet (left axis) and the incoming shortwave radiation is plotted in red (right axis) with respect to time in UTC+1. The black dashed box frames the days selected for the analysis. On the top of each graph is the site, starting date of the presented and the source of the data

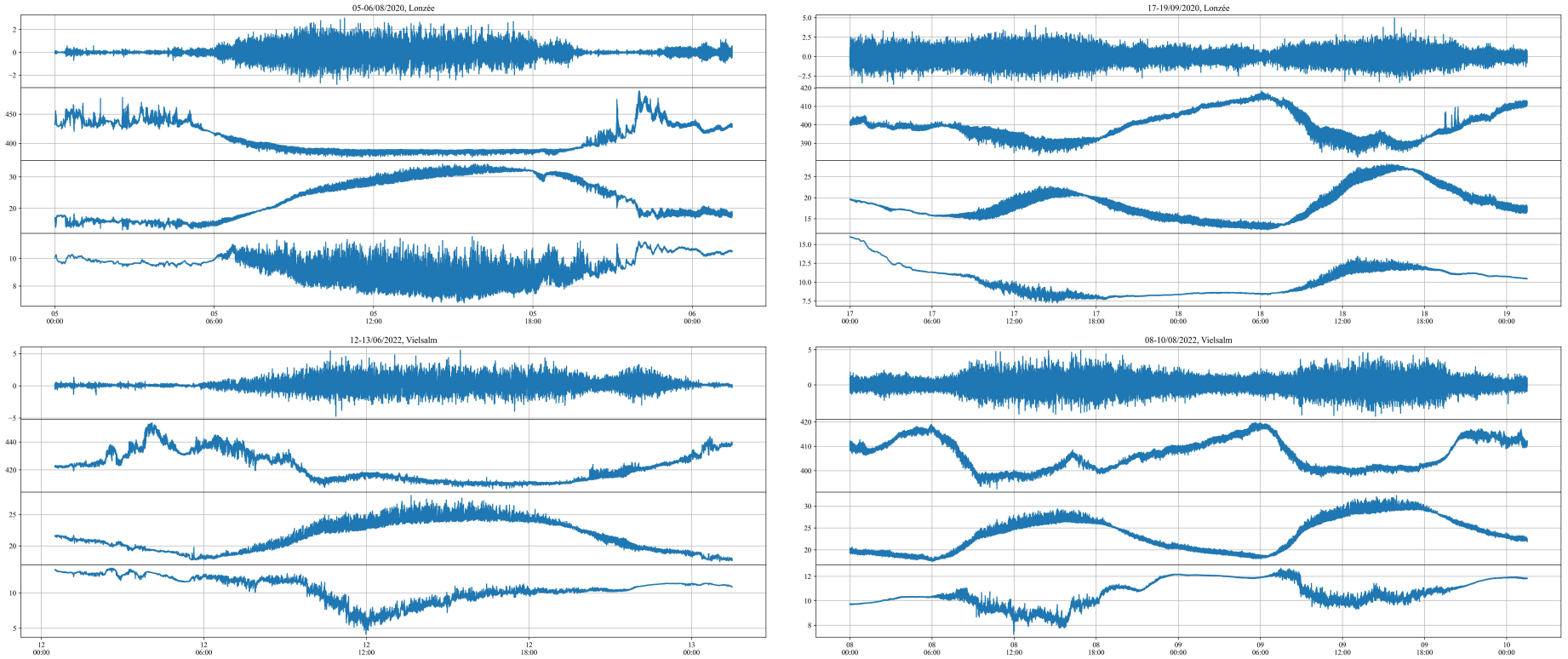


Figure 23: Time-series of vertical wind velocity (top), $CO_2$ (second row) concentration $[\mu mol_{gas} mol_{air}^{-1}]$, temperature (third row) and $H_2O$ $[\mu mol_{gas} mol_{air}^{-1}]$ (bottom)

## 4.3 $CO_2$, temperature and $H_2O$ fluxes

To facilitate the designation of *records*, these will be referenced with the first three letters of the site name (e.g. "Lon" for Lonzée), followed by the date of the record in a yyyy-mm-dd format and a letter designating the scalar ("c" for $CO_2$, "t" for temperature and "h" for $H_2O$). If the scalar is not specified, then the reference designates the *day* (e.g. Lon_2020-08-05 refers to the 5th of August 2020, a day analyzed in Lonzée, and Lon_2020-08-05_c refers to the record of $CO_2$ on that day).

In general, all the analyzed records met satisfactory conditions of stationarity and thus are expected to not contain any mesoscale motions due to turbulence intermittency or diurnal variations. The COI is more concerning : two elements ascertain that the cospectral peak visible visible near the COI line with $qcoi = e^{-1}$ is due to edge effects. First, wavelet coefficients explode beyond the border of the COI with a threshold $qcoi = e^{-1}$, noted $\mathrm{COI}_{e^{-1}}$ (Fig. 25). Second, the discontinuities of wavelet cross-coefficients are situated exactly where two files were concatenated to create the cross-scalogram, which suggests that wavelet coefficients in this region of the time-frequency plane were influenced from edge effects. The discontinuities are visible in high periods (Fig. 29 1,2,4; Fig. 28 1,2). For better visualization, a zoomed cross-scalogram is shown for Lon_20-09-18_c in Fig. 24 and similar depictions for all the other records are made available in Appendix 8.5. From the observation of the zoomed cross-scalograms, it is assumed that components in periods above the $\mathrm{COI}_{0.10}$ are spurious, while components in periods comprised between the lines of $\mathrm{COI}_{0.02}$ and $\mathrm{COI}_{0.10}$ are affected by edge effects by are still valid for qualitative analysis. On the other hand, quantitative analysis of components in this region is not exact but is assumed to be satisfying for comparisons of relative contributions in the mesoscale and turbulent range. The ogives will be computed for periods ranging up to the line of $\mathrm{COI}_{0.10}$, situated at 3.2 hours, but the analysis of ogives > $\mathrm{COI}_{0.02}$ (periods of 2.8 hours) must remain cautious.

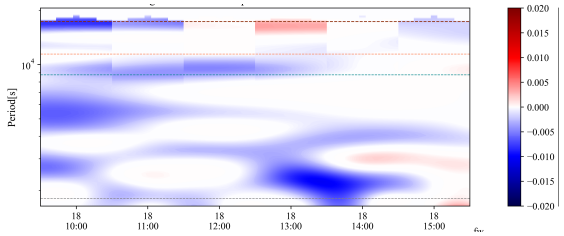


Figure 24: Example of cross-scalogram for Lon_20-09-18_c zoomed in the periods >30 min (gray line). The lines represent the $\mathrm{COI}_{0.02}$ (turquoise), $\mathrm{COI}_{0.10}$(orange) and $\mathrm{COI}_{e^{-1}}$

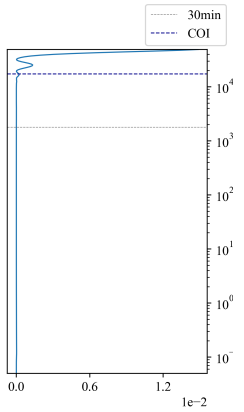


Figure 25: Cospectrum of Vie_2022-08-09_c, including the periodic range beyond the COI (dashed blue line). The dashed gray line is placed at 30 min.

Regarding the range of periods < 30 min, the cospectra of $CO_2$ and temperature form similar Gaussian shapes on both sites. A few differences distinguish spectral behaviors for both scalars:

1. $CO_2$ fluxes are mostly negative while temperature fluxes and $H_2O$ fluxes are mostly positive
2. At the same date, there are temperature fluxes at lower periods of revolution than $CO_2$ and $H_2O$.

The fluxes also show site-specific differences in the range of periods <30 min :

1. Significant components appear at periods > 10 s in Vielsalm, but appear already for much lower periods (>$10^{-1}$) in Lonzée
2. The peak of the Gaussian is situated at $10^2$s in Lonzée, and $10^3$s seconds in Viesalm. This is also evident in the ogives as the most important slope is between 0 and 15 minutes for Lonzée and between 0 and 30 minutes in Vielsalm.
3. Flux magnitudes are greater in Vielsalm than in Lonzée
4. The cospectral gap is well-defined at 30 min in Lonzée, which can be seen in the ogive graphs (Fig. 30) as a convergent before the 30-min period for all of the analyzed dates and for both scalars in for the site of Lonzée, with only two exceptions where the convergent is in higher periods (Lon_2020-09-17_t and Lon_2020-09-17_h). There is also a convergent in the ogives of certain records in Vielsalm, but it is not as consistent.

The key features of the wavelet decompositions of the flux are regrouped in Table 2, presented after the cross-scalograms and cospectra. The maximal magnitude attained by $E_{wc}$ (Eq.22) in periods < and > 30 min give an idea of the strength of flux components in both ranges. It is smaller than the maximal height of the plotted cospectra, because, as a reminder, the cospectrum shows the cumulated *absolute* wavelet coefficients. In the range of periods > 30 min, flux magnitudes are lower by one to two orders of magnitude compared to the lower periods – except for Vie_2022-12-06_c and all records of $H_2O$ in Vielsalm where the order of magnitude is similar – which translates into milder colors in the cross-scalograms and as lower peaks in the cospectra.

Since the ogives are computed for periods ranging up to 3.2 hours, the proportion of the flux contained in periods < 30 min was calculated with respect to the value of flux attained at 3.2 hours. In Table 2,

the mean EBR between 09:00-16:00 is also added. Half-hourly fluxes for the calculation of the EBR in Table 2 were taken from the PI-processed datasets available on demand at the Wallonian ICOS team. However these fluxes differ significantly from those of of the carbon portal. These two available sources are presented more extensively in Appendix 8.6. The $\%flux_{<30min}$ usually underestimated the EBR, except for some records of water vapor flux where it overestimated it, and except for the day Vie_2022-08-08 where the $\%flux_{<30min}$ was close to the EBR.

Shapes of the ogives are also displayed in Table 2, with the "convergent", "oscillating" and "rising" shapes corresponding respectively to case 1, 2 and 3 in Foken et al. (2006a&b). The two records with a convergent ogive also have the greatest amount of flux contained in the periods < 30 min, but do not show a better EBR than the other. The components in high periods are both negative and positive signs in Vielsalm, so these components compensate each other and the fraction of the flux contained in the periods < 30 min is generally higher in Vielsalm than in Lonzée. The EBR is also higher in Vielsalm than in Lonzée, but this EBR differs from the fraction of flux in periods < 30 min.

The wind direction seems to influence the fraction of flux in periods < 30 min in Lonzée : this fraction is greater when the wind comes from the South, but the EBR is not affected by the wind direction. In Vielsalm, the wind direction does not seem to have any influence on the ogives nor on the EBR.

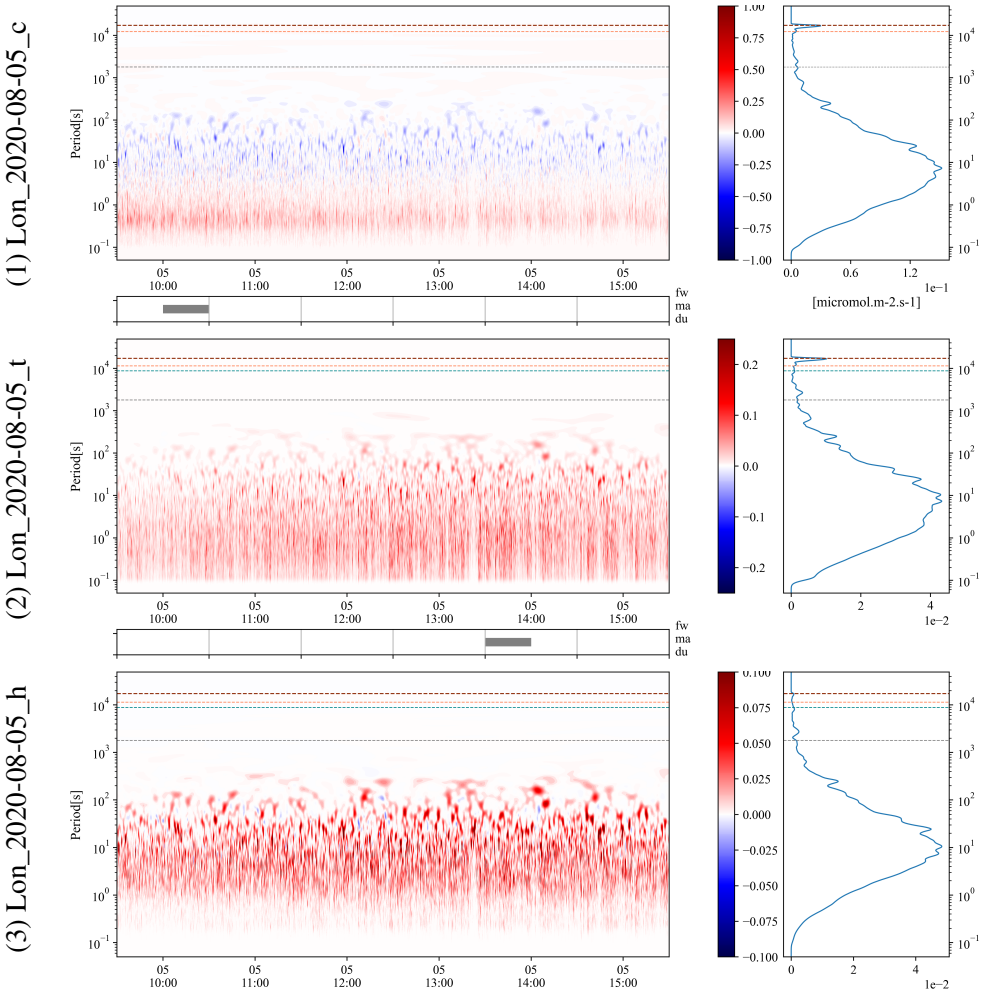


Figure 26: Cospectra of $w$ and $CO_2$, $w$ and temperature and $w$ and $H_2O$ for the the 2020-08-05 in Lonzée. The line graph in the middle shows results of stationarity tests (gray = instationary, white = stationary) for the half-hour record for three tests: FW (top), MA (middle) and DU (bottom). The gray dashed line presents the 30-min threshold, the orange dashed line is the limit of the COI at a level of $e^{-2}$ and the red dashed line is the limit of the COI at a level $e^{-1}$

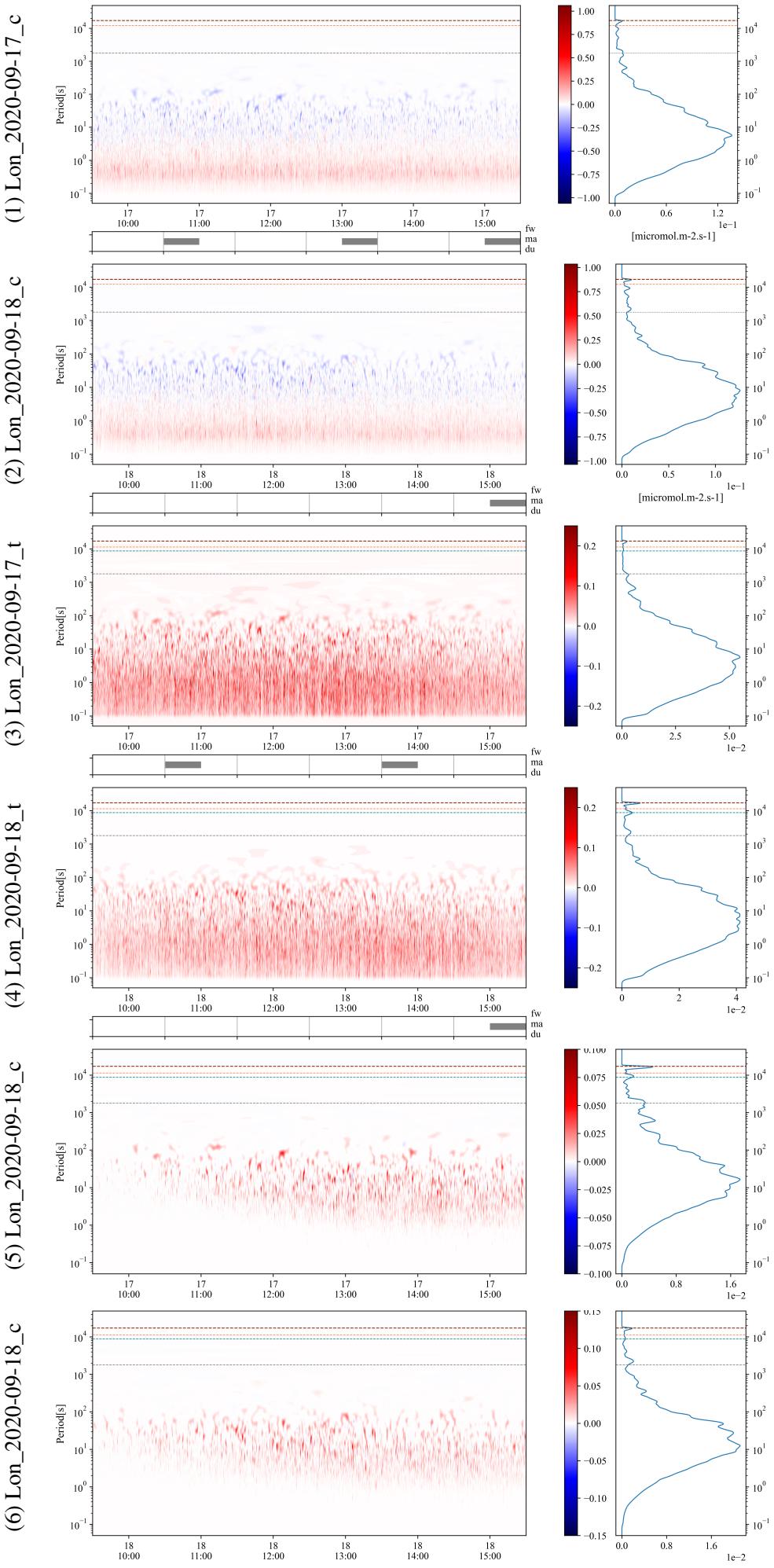


Figure 27: Same graph as Fig. 26 for the the 2020-09-17 and 2020-09-18 in Lonzée.

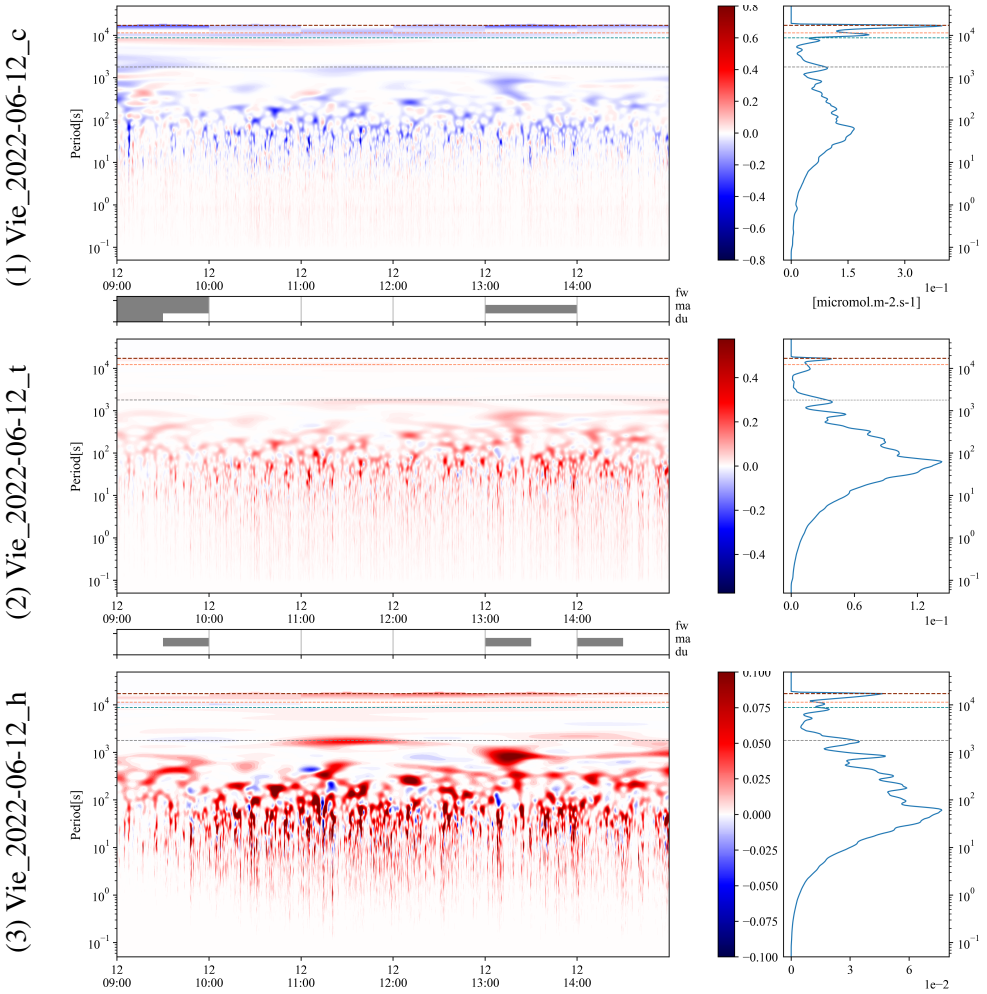


Figure 28: Same graph as 26 for the 2022-06-12 in Vielsalm

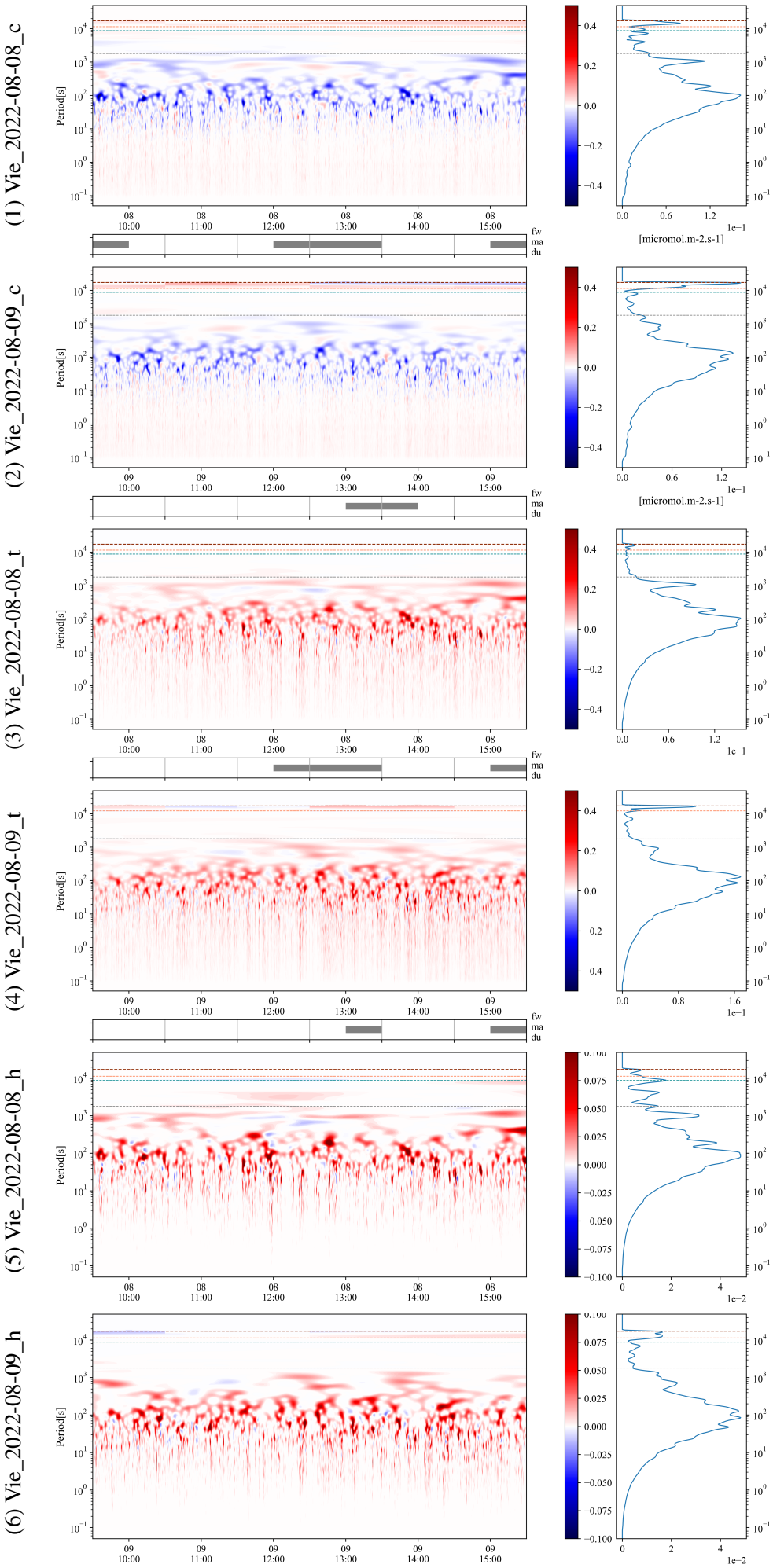


Figure 29: Same graph as 26 for the 2022-08-08 and 2022-08-09 in Vielsalm

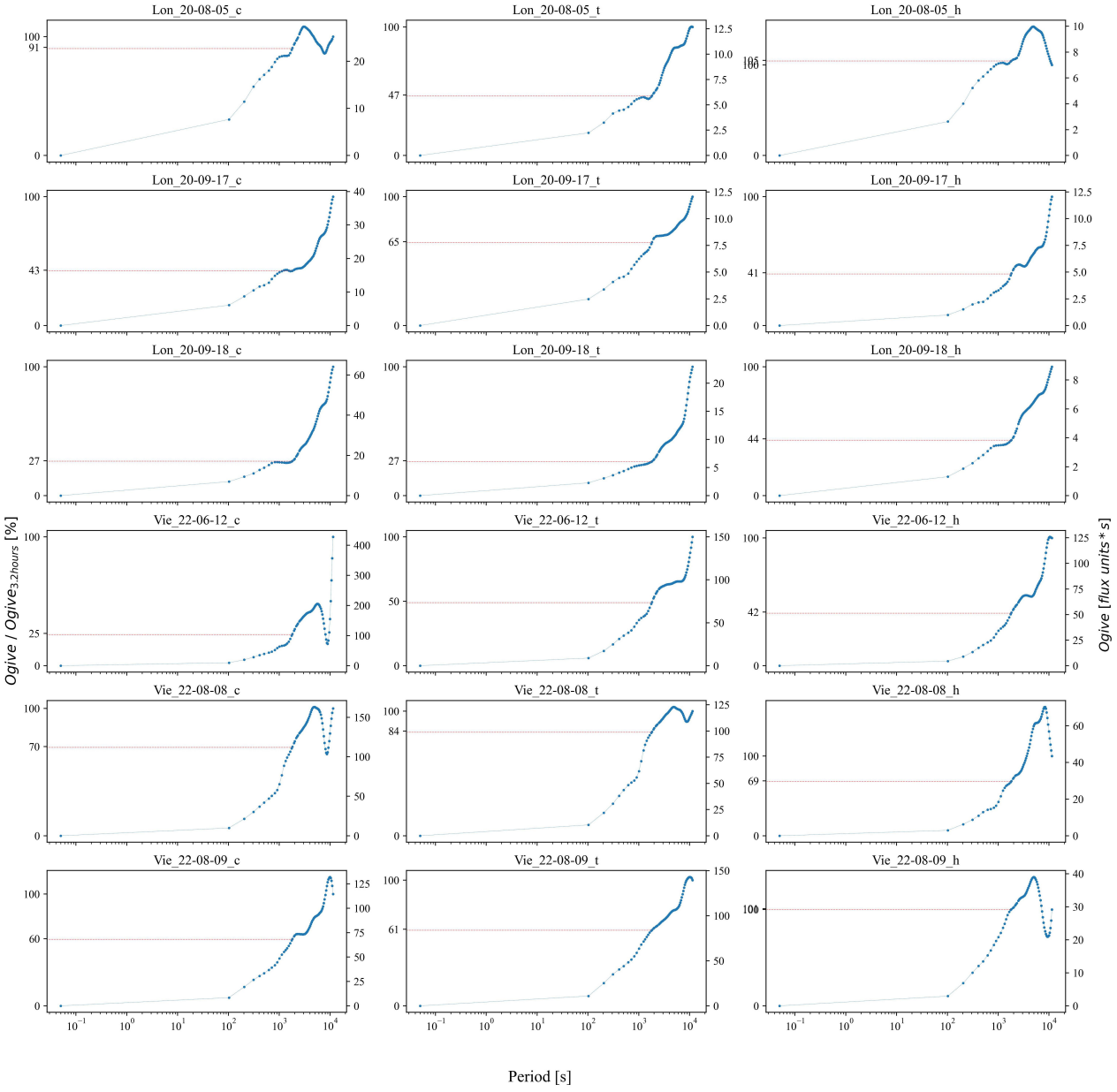


Figure 30: Ogive of the cospectra for the period 09:00-16:00 on each day of the analysis computed for periods of 0.05-1150s (x-axis). The calculated ogives are represented with respect the periods of revolution in logarithmic scale (x-axis) as a fraction in [%] of the ogive attained at 3.2 hours (left y-axis) and as the value of the integral of flux (right y-axis)

Table 2: Summary of the key features of the flux and environmental conditions for every record : the maximal magnitude of the flux ($E_{wc}$, Eq. 22) for periods < and > 30 min is given in the units of wavelet coefficients. The fraction of flux at 30 min is calculated as $ogive_{30min}/ogive_{3.2hours}$. Ogives shapes of convergent, oscillating and rising correspond to the Case 1, 2 and 3 in Foken et al. (2006a) and the () denote the uncertainty of the value due to strongly raising fluxes near the $COI_{0.10}$. EBR is taken from the Biodyne research center 4.

| Record | Magn. $_{\text{min}}^{<30}$ | Magn. $_{\text{min}}^{>30}$ | flux $_{<30\text{ min}}$ | Ogive shape | EBR | Upwind dir. |
|---|---|---|---|---|---|---|
| Lon_2020-08-05_c | 0.13 | 0.0058 | 91% | convergent | 73% | S |
| Lon_2020-08-05_t | 0.036 | 0.0028 | 47% | rising | | |
| Lon_2020-08-05_h | 0.041 | 0.0021 | 105% | oscillating | | |
| Lon_2020-09-17_c | 0.11 | 0.0042 | 43% | rising | 77% | N |
| Lon_2020-09-17_t | 0.046 | 0.0024 | 65% | rising | | |
| Lon_2020-09-17_h | 0.014 | 0.0026 | 41% | rising | | |
| Lon_2020-09-18_c | 0.11 | 0.0094 | 27% | rising | 73% | N |
| Lon_2020-09-18_t | 0.034 | 0.0036 | 27% | rising | | |
| Lon_2020-09-18_h | 0.018 | 0.0021 | 44% | rising | | |
| Vie_2022-06-12_c | 0.14 | 0.19 | (25%) | oscillating | 86% | W |
| Vie_2022-06-12_t | 0.13 | 0.033 | 50% | rising | | |
| Vie_2022-06-12_h | 0.066 | 0.022 | 42% | oscillating | | |
| Vie_2022-08-08_c | 0.16 | 0.037 | 70% | oscillating | 76% | NNE |
| Vie_2022-08-08_t | 0.15 | 0.018 | 84% | convergent | | |
| Vie_2022-08-08_h | 0.047 | 0.015 | 69% | oscillating | | |
| Vie_2022-08-09_c | 0.13 | 0.021 | 60% | oscillating | 78% | NNE |
| Vie_2022-08-09_t | 0.16 | 0.015 | 61% | oscillating | | |
| Vie_2022-08-09_h | 0.045 | 0.045 | 101% | oscillating | | |

# 5 Discussion

### 5.0.1 Parametrization of the XWT

The most accurate covariance obtained with the Morlet wavelet (Fig. 21) might be due to the fact that the Morlet wavelet better captures the variations of the signal due to its shape (Torrence and Compo, 1988). Nonetheless, the fact that the parameters were adjusted to minimize the error with the Morlet wavelet, and not with the Mexican hat probably allowed a better parameterization for this wavelet, but is in accordance with Schaller et al. (2017) who found a smaller error for the Morlet wavelet (2% than for the Mexican hat (7%) on stationary data. The study of Li et al. (2023), which compared the covariance of both wavelets using artificial instationary data, found that the Mexican hat yields more precise results for high grades of instationarity, even though they stress that their results might not be directly transferable to real data.

Regarding the influence of the COI, the average error is minimized when $qcoi$ is set to $\simeq 0.22$. This shows that the restrictiveness of the COI should be balanced by the compromise between including components of relatively long periods and excluding edge effects. However, the largest analyzed period can be augmented by extending the averaging time, which would probably be the best solution since the larger scatter of $\langle \varepsilon \rangle$ for $qcoi > 0.10$ (Fig. 20) shows that spurious components were

sometimes included with this threshold. In summary, even though $qcoi = 0.22$ provided the best accuracy for 30-min stationary records, it is suspected that a more restrictive $qcoi <= 0.10$ will be more suitable for wavelet decomposition of longer time-series.

It is rather unsurprising that lower values of $\delta j$ and $\text{Period}_{\text{min}}$ provide smaller errors for $Cov_{XWT}$ due to an improved resolution. The values discussed in section 3.1.5 are thus kept for the performance of the second objective.

## 5.1 Fluxes of $CO_2$, temperature and $H_2O$ on Lonzée and Vielsalm

The following discussion concerns the results obtained in the scope of the second research objective. Since the spectral gap was well-observed at 30 min in Lonzée, in the following section, a partitioning of scales will be assumed on this basis. Fluxes at periods < and > 30 min will be respectively referred to as turbulent and mesoscale in both Vielsalm and Lonzée for practicality, even though it is yet unclear whether such partitioning is funded on physical processes.

### 5.1.1 Source partitioning

The large majority of the $CO_2$ flux on every record is negative, which is unsurprising in the seasons where most of the crop vegetation on Lonzée (principally sugar beet) and the tree foliage in Vielsalm is fully developed and plant photosynthesis acts as a sink of $CO_2$. However, eddies of lower periods of revolution contribute to positive fluxes, signs of biological respiration, especially on the site of Lonzée. Since positive and negative fluxes occur simultaneously with different frequencies, they probably originate from different sources. The positive fluxes are in periods of approximately $4.10^{-1}$s and in the condition of mean wind at the time of the analysis (Table 3), the eddy size of these positive fluxes is consequently of approximately 0.90, 1.24 and 1.6 m assuming frozen turbulence. Hence, the surface that is likely to contribute to these fluxes is the sugar beet crop on which the tower stands. Sugar beet is typically in intensive growth from mid-May to mid-July and is harvested in September or October, and since the cospectra on Lon_2020-08-05 contain similar components in the small periods < 30 min as Lon_2020-09-17 and Lon_2020-09-18, crop cover was likely present on all days of the analysis.

Models of source partitioning such as that of Scanlon and Kustas (2010) can distinguish between soil and plant-emitted $CO_2$ and $H_2O$ fluxes by calculating their correlation $\rho$. If that value is smaller than the leaf-level water use efficiency (WUE), which is the ratio of $CO_2$ and water vapor exchanged only through plant stomata, it indicates soil respiration. Such partitioning was for example implemented in the Large-Eddy Simulation (LES) of Klosterhalfen et al. (2019), who simulated winter barley exchanging these scalars at different heights, with a source distributed mainly between the soil and the top of the plant cover (Fig. 31).

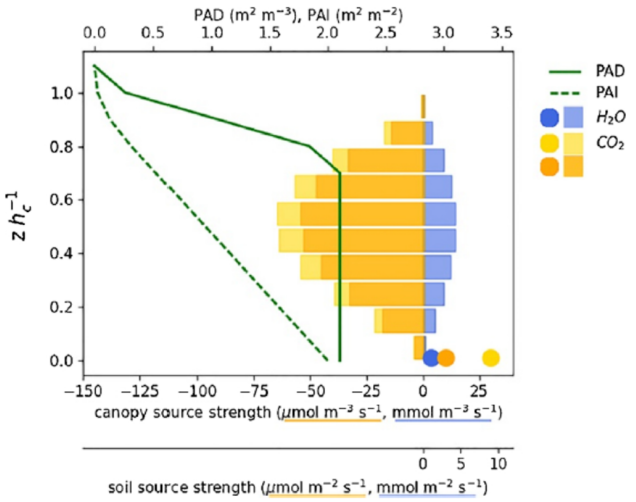


Figure 31: Vertical profile (height z /canopy height $h_c$) of ten sources and sinks of $H_2O$ and $CO_2$ from vegetation (bars) and one source from soil (circles), plant area density (PAD) and cumulative plant area index (PAI) used for LES of Klosterhalfen et al. (2019). Yellow and orange distinguish different $CO_2$ source/sink strength scenarios

Their model allowed to compute the vertical profiles of $CO_2$ fluxes and H2O fluxes, which could then be plotted (Fig. 32).

However, in the case of the tower measurements in Lonzée, the fluxes are sampled at only one height, as opposed to all heights as in LES. Therefore, the separation of soil and plant origins of water vapor and carbon dioxide would imply that for a certain measurement height, a relationship between the period of oscillation of the signal, the size of the eddy and also the height of the source can be made. Smaller eddies are usually sampled from lower measurement heights (McNaughton and Laubach, 2000), because the size of the eddies is limited due to the ground. However, the relationship between measurement height, height of the source and size of the eddy sources has to be further investigated in order to partition fluxes from their cospectral distributions. Indeed, simply assuming that Taylor's space-scale conversion is exact and that eddies are isotropic would mean that sources of $CO_2$ were brought from : $\underbrace{2.1}_{measurement height} - \underbrace{0.90}_{eddy\ diameter} = 1.2\ [m]$ above the ground, which does neither correspond to soil nor to sugar beet height.

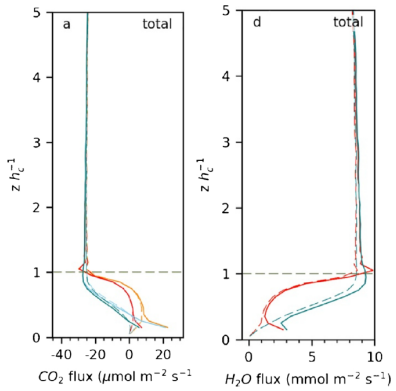


Figure 32: Vertical profiles (height z /canopy heigh $h_c$) of $CO_2$ and $H_2O$

### 5.1.2 Mesoscale components : comparison with other studies

Despite the fact that most half-hours were not flagged as instationary, mesoscale components of the flux were observed on both study sites. Overall, mesoscale motions represent a large portion of the average flux over the whole day and the whole averaging period (in the following developments, the "averaging period" refers to the range in the frequency domains over which the flux is integrated, i.e. the x-axis of the ogives). This shows that mesoscale motions are indeed present, and consequently, the flux averaged over a 30-min period[3] is assumed to be underestimated, which confirms the hypothesis that mesoscale motions are responsible for the SEB unclosure on both Lonzée and Viesalm. But the proportion of mesoscale flux found on the analyzed days is not at all consistent with the SEB residual (100% - EBR) as shown in Table 2. Actually, the EBR should be compared to a weighted sum of latent and sensible heat fluxes in [W $m^2$], but for the sake of simplification it will be assumed that temperature and $H_2O$ fluxes are equally underestimated in the calculation of EBR and that $\%flux_{<30min}$ should equal EBR for these two scalars.

Since conditions of turbulence intermittency were avoided in a major way, mesoscale motions are most probably linked to spatial heterogeneity at the mesoscale. Studies with extended averaging periods have shown that, over heterogeneous sites (Finnigan et al., 2003; Paleri et al., 2022), mesoscales motions appear. However, over homogeneous sites (Dupont 2019), there is few flux components oscillating in periods > $10^3$ s, even with averaging periods as long as $10^5$ s (Dupont, 2019, see Fig. 9). Nonetheless, assessing how spatial heterogeneity creates mesoscale motions on Lonzée and Vielsalm requires to first analyze the characteristics of mesoscale motions that transfer in the cross-scalograms, cospectra and ogives.

On the days when ogives oscillate or converge (Lon_2020-08-05, Vie_2022-08-08, Vie_2022-08-09 and Vie_2022-06-12) extending the averaging time could diminish the difference between the EBR and the calculated percentages of flux in periods < 30 min. Essentially, if extending the averaging time made the ogive for the whole averaging period shrink (grow), the percentage of flux contained in periods < 30 min would increase (decrease). A hypothesis which could explain the inconsistency between EBR and the proportion of $flux_{< 30\ min}$ is that ogives converge for averaging periods longer than 3.2 hours (Foken et al., 2006a& b). Finnigan et al. (2003) found that averaging over 4 hours was sufficient to capture all components over a homogeneous forest, but not for the two heterogeneous forests where the 8-hour averaging period captured additional components. Since the ogives on Lon_2020-08-05, Vie_2022-08-08 and Vie_2022-08-09 oscillate, extending the averaging time would modify the fraction of flux contained in periods < 30 min and a convergence could be found after some periods.

However, on the days when the ogives grow with a strong slope for all three scalars (Lon_2020-09-17, Lon_2020-09-18), convergence for longer averaging periods seem improbable, and in the periods comprised between $COI_{0.10}$ and $COI_{0.02}$, flux components are of the same sign as in the periods below (Appendix 8.5). Moreover, landscape heterogeneity cannot explain alone why flux components in the mesoscale range are of the same sign. The consistently rising ogives could be due to the presence of mesoscale convective structures that do not propagate with a mean wind that is not well observed from measurement towers (Etling and Brown, 1993). When eddies propagate past the measurement point, both updraft and downdraft motions are adequately measured, and then the time-averaged vertical

[3] In the frequency domain, as explained above

velocity is supposed to vanish. However, if the convective structure is fixed on the landscape, the same part of the cell is continuously observed by the tower, so the observation is biased (Patton et al., 2005; Inagaki et al., 2006; Mauder et al., 2008; Mahrt, 2010; Mauder et al., 2020; Paleri et al., 2022). Such structures are qualified as "quasi-stationary"– a denomination related to the fact that they are fixed on the landscape rather than to a presumed state of flow stationarity, even though that condition is also verified – and as "turbulent organized structures " (TOS) in LES (Inagaki et al., 2006; Mauder et al., 2007a) and are distinct but can coexist with "regular" propagating mesoscale eddies (Inagaki et al., 2006; Mauder et al., 2010).

Since quasi-stationary motions do not propagate — or only slowly—, a period of revolution cannot be attributed from time-averaged measurements such as those conducted from a tower. Hence, they do not respect Taylor's space-scale conversion. In fact, this law is only respected in a small portion of the time-frequency domain (Fig. 33).

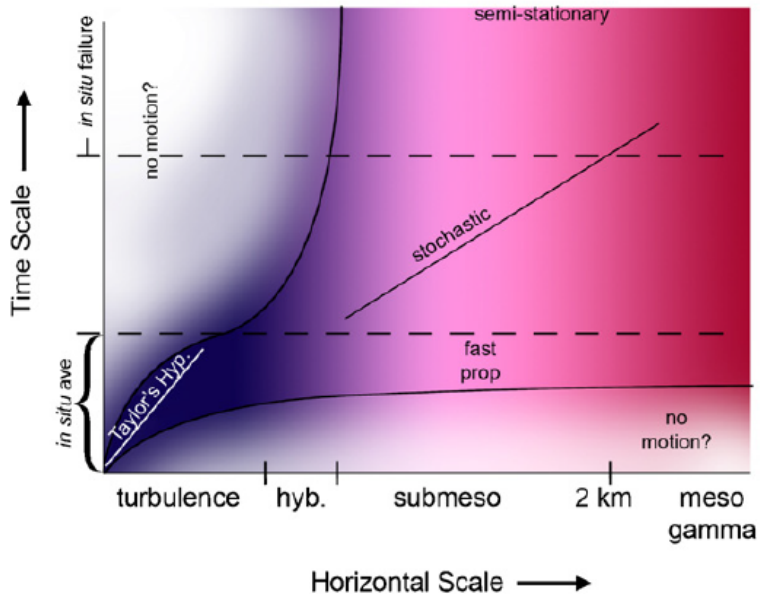


Figure 33: Types of turbulent structures in the space-time plane. Taylor's space-frequency conversion law is depicted in the lower left corner (white line). Quasi-stationary motions are situated outside of the graph, they are bigger than 2 km and extend in large temporal scales (they are larger than "*semi-stationary*" motions). "*In situ failure*" refers to the inability to capture components of this region. "In situ ave" designates the ranges included in EC processing, according to the choice of the averaging time. White regions indicate nonexistence (figure from Mahrt, 2010)

Further, if the motions were completely stationary, they would not create oscillations $w'$ and $c'$ in the signals measured from towers (Mauder et al., 2008) and their contribution would rather fold into the terms of horizontal and vertical advection, $\bar{u}\frac{\delta\bar{c}}{\delta x}$ and $\bar{w}\frac{\delta\bar{c}}{\delta z}$. A few authors (Lee, 1998; Finnigan, 1999) have explored the possibility to include these motions to the scalar conservation equation as vertical and horizontal advection. Finnigan (1999) represented quasi-stationary motions in two dimensions – these can represent roll vortices or cell-like structures in reality – in the presence of additional horizontal mean wind. His representation (Fig. 34) shows that streamlines are vertical only on the ground, that $\bar{u}$ is never negligible compared to $\bar{w}$, and that, on the horizontal center of the motion, $\bar{w} = 0$. If the cells are standing, the mass balance could be corrected by adding both the terms of vertical and horizontal advection, but these terms are technically difficult to measure.

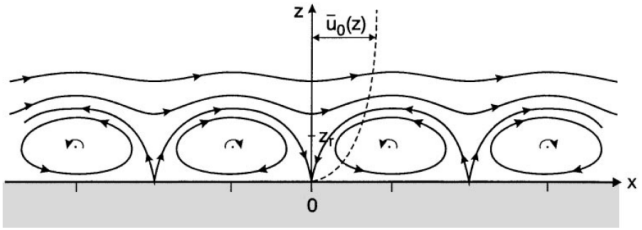


Figure 34: Representation of quasi-stationary motions in two dimensions (Finnigan, 1999)

#### 5.1.2.1 Influence of quasi-stationary motions on our sites

On Lon_2020-09-17 and Lon_2020-09-18, the fact that the $\%\text{flux}_{<30\text{ min}}$ is very small relative to the EBR might be due to an overestimation of the fluxes averaged over 3.2 hours (in the frequency domain) because the tower is situated in the updraft of quasi-stationary eddies. The percentage of overestimation of the sensible heat flux averaged over 3.2 hours can be calculated according to Inagaki et al. (2006), assuming that the flux calculated over a 30-min averaging time is equal to the EC flux thanks to the developments in 4.1.2[4]:

$$\%TOS = 100\% - SEB_{residual} - \%flux_{<30min}$$

Since quasi-stationary eddies are difficult to observe from single-point (Mauder et al., 2010) and even from spatial measurements (Lothon et al., 2007), numerical simulations such as LES and mesoscale models are to this day, the most explored way to understand their dynamics. LES of idealized one-directional surface heterogeneities with no mean wind have shown that the sensible heat flux is overestimated in zones of vertical updrafts and underestimated in zones of vertical downdraft of quasi-stationary motions (Patton et al, 2005). A 20-25% overestimation of sensible heat due to quasi-stationary motions was also concluded with the LES of Prabha et al. (2007b), which featured moderate horizontal wind speed (5 m $s^{-1}$) and heterogeneities reproducing a real-life forest site with clearcuts. These studies have come in opposition with previous LES studies (Kanda et al., 2004) and theoretical considerations (Mauder et al., 2008) stating that the updraft of stationary eddies can only induce an underestimation of the sensible heat flux, since the contributions $\overline{w'T'}$ ($T$ is the measured signal of temperature) they carry are necessarily positive since $w' > 0$ when $T' > 0$ and $w' < 0$ when $T' < 0$ because cold air sinks and warm air rises (Fig. 35).

[4]Here again, the calculation supposes that the SEB residual is due in equal parts to latent and sensible heat flux.

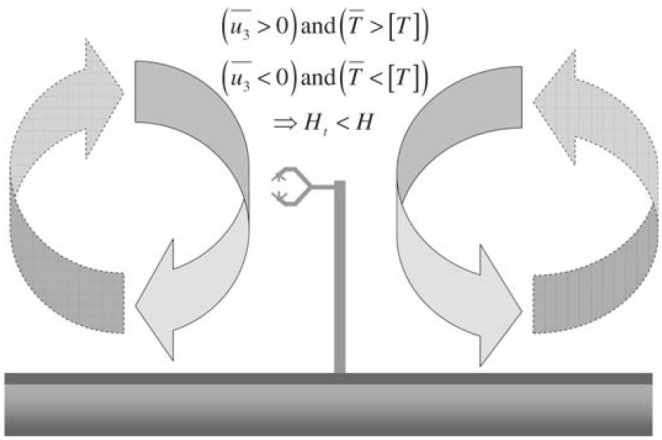


Figure 35: Schematic representation of the way the updraft or downdraft of quasi-stationary motions carrying sensible heat leads to an underestimation of the sensible heat flux (Mauder et al., 2008)

However, the assumption that the total flux is overestimated due to an updraft of quasi-stationary eddies can be contradicted. The studies of Patton et al. (2005) found that in zones of vertical updrafts, the latent heat flux should be underestimated, at least in heights < 0.8 $z_i$, where $z_i$ is the height of the boundary layer, while on Lon_2020-09-17 and Lon_2020-09-18, the water vapor fluxes are also presumed to be overestimated since the $\%\text{flux}_{<30\text{min}}$ is very small compared to the EBR. The observation of the latent heat flux brought by quasi-stationary eddies is less covered in literature, so an expansion of this study is difficult. Overall, the study of quasi-stationary motions is very exploratory and while their existence is commonly acknowledged, their understanding is majorly brought by numerical simulations.

Quasi-stationary motions have been observed with spatially resolved measurements conducted using aircraft (Mauder et al., 2007a), scintillometers (Boland, 2019), LiDAR (Higgins et al., 2013) or sets of multiple towers (Steinfeld et al., 2007; Mauder et al., 2008; 2010) leading to spatial averaging, which allows to capture the contribution of quasi-stationary motions in [w'c'] (brackets denote the operation of spatial averaging). Some studies even propose to combine spatial and temporal averaging with the hopes to include quasi-stationary motions *and* obtain continuous flux measurements. Mauder et al. (2010) propose to calculate the flux with combined averaging $F$ following :

$$F = \bar{w}\ (\bar{c} - [c])\ + \overline{w'c'} \tag{28}$$

Where the mean vertical velocity $\bar{w}$ would be measured from one tower and the $[c]$ would be calculated from measurements conducted at several points in space. However, they have not succeeded in closing SEB with that setting (Appendix 8.7).

## 5.2 Environmental conditions inducing mesoscale motions

In the following developments, the site characteristics that could explain the presence of quasi-stationary *and/or* "regular", propagating mesoscale motions under the conditions of mean horizontal wind speed $\overline{U}$ are assessed. Distinction between the conditions susceptible to lead to quasi-stationary or "regular" mesoscale motions is made when possible, but since both types of mesoscale motions are induced by heterogeneity, this distinction is not always possible. If unspecified, then the conditions are assumed to be possible to yield both types of motions.

It is the depth of the ABL $z_i$, which is typically one or two kilometers (Prabha et al., 2007b) that in great part determines the scale of the heterogeneities potentially responsible for mesoscale circulation. The ability of heterogeneties smaller than $z_i$ to create mesoscale motions are reduced in the presence of mean wind (Mahrt, 1998, Patton et al., 2005; Prabha et al., 2007b) and are mostly present when mean wind is weak (0 to 1 m $s^{-1}$) (Patton et al., 2005; Inagaki et al., 2006; Steinfeld et al., 2007). If the mean wind is very weak, large convective structures are more likely to be completely stationary, and they would not at all contribute to oscillations (Mauder et al., 2008; Mahrt, 2010) and would not lead to overestimated fluxes : the contribution of completely stationary structures folds into the terms of the horizontal and vertical advection $\bar{u}\frac{\delta\bar{c}}{\delta x}$ and $\bar{w}\frac{\delta\bar{c}}{\delta z}$. On the contrary, heterogeneities of wavelengths $\approx z_i$, comprised between 2km and 100 km (Dalu et al., 1996) are likely to yield strong quasi-stationary mesoscale motions with increasing mean wind (2 m $s^{-1}$ to 5 m $s^{-1}$). Quasi-stationary motions are stronger over heterogeneous terrain, where they result of the competition between differential buoyancy and horizontal pressure gradients (Inagaki et al., 2006; in Patton et al., 2005). When the horizontal pressure gradients dominate (Patton et al., 2005) and mean wind is moderate but not weak (Prabha et al., 2007b, Steinfeld et al., 2006), these motions take the form of roll vortices, which are also called "cloud streets" since they extend very far in the streamwise direction (Fig. 36) and can spread over a significant part of the globe in that dimension (Etling and Brown, 1993).

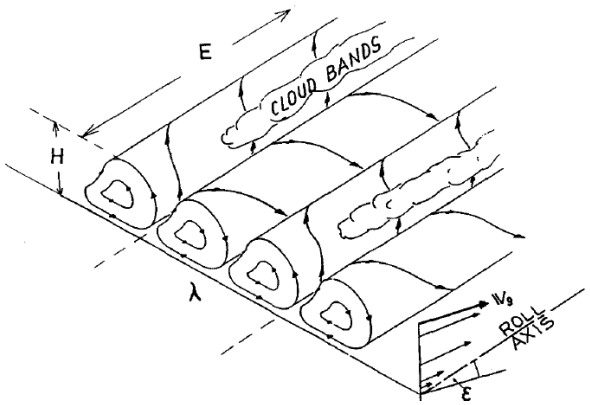


Figure 36: Schematic representation of roll vortices (Etling and Brown, 1993)

Rolls are broken down into small-scale plumes if buoyancy takes over (Patton et al., 2005; Steinfeld et al., 2006; Mauder et al., 2020).

#### 5.2.0.1 Mean wind speed

Quasi-stationary form majorly during daytime when mean wind is moderate (5 m $s^{-1}$) (Prabha et al., 2007b) or weak (0 to 1 m $s^{-1}$) (Patton et al., 2005; Inagaki et al., 2006; Steinfeld et al., 2007). However, if the mean wind is very weak, they are more likely to be completely stationary, and they would not at all contribute to oscillations (Mauder et al., 2008; Mahrt, 2010), but their contribution will rather fold into the terms of the horizontal and vertical advection $\bar{u}\frac{\delta\bar{c}}{\delta x}$ and $\bar{w}\frac{\delta\bar{c}}{\delta z}$ (Finnigan, 1999).

On Lonzée and Vielsalm, quasi-stationary motions are more likely to appear from heterogeneities of scales > $z_i$ since the mean wind is moderate (Table 3). Previous studies calculating fluxes with XWT from aircraft measurement confirm that mesoscales have wavelengths larger than 2 km (Mauder et al.,

2007a, Lothon et al., 2007) and even up to 10 km (Paleri et al., 2022), which means that there exist heterogeneities of similar wavelengths.

Table 3: Mean horizontal wind $\bar{U} = \sqrt{u^2 + v^2}$ for the period 09:00-16:00 for each date of the analysis

| Site | Date | $\bar{u}[ms^{-1}]$ |
|---|---|---|
| Lonzée | 2020-08-05 | 2.2 |
| | 2020-09-17 | 3.1 |
| | 2020-09-18 | 4.1 |
| Vielsalm | 2022-06-12 | 2.7 |
| | 2022-08-08 | 2.9 |
| | 2022-08-09 | 3.9 |

#### 5.2.0.2 Spatial heterogeneity on Lonzée

As a first approach, the test of integral characteristics examines moisture and temperature source-distribution heterogeneity. If the integral characteristics calculated from the variance of wind and scalar measurements are greater than values computed from similarity parameters (e.g. friction velocity, Monin-Obukhov length), it indicates that spatial heterogeneities have induced instationarities in the calculation of the EC flux (Foken and Wichura, 1996). On Lonzée, this test indicated that during the day and under unstable conditions, the temperature source field is heterogeneous towards the North and even more in the South (Moureaux, 2004). No heterogeneities in the wind field were, however, detected in these directions.

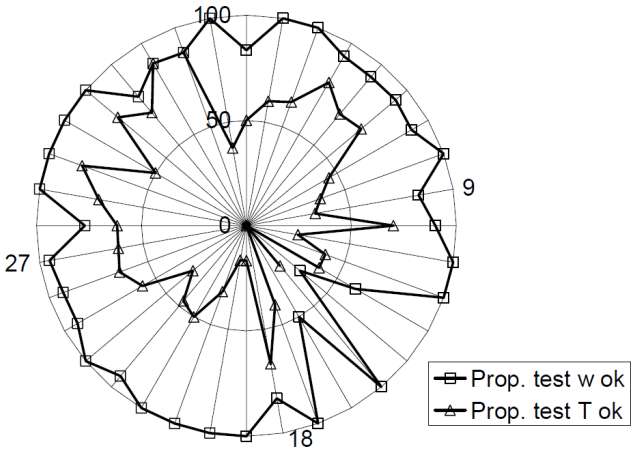


Figure 37: Proportion of diurnal half-hour records respecting the integral characteristics for $w$ (squares) and T (triangles) (Moureaux, 2004)

Similarly, the SEB closure on Lonzée in conditions of well-developed turbulence is also slightly better in the Northern direction than in the Southern direction (Fig. 38, Boland, 2019), which could suggest that the landscape towards the South is more heterogeneous.

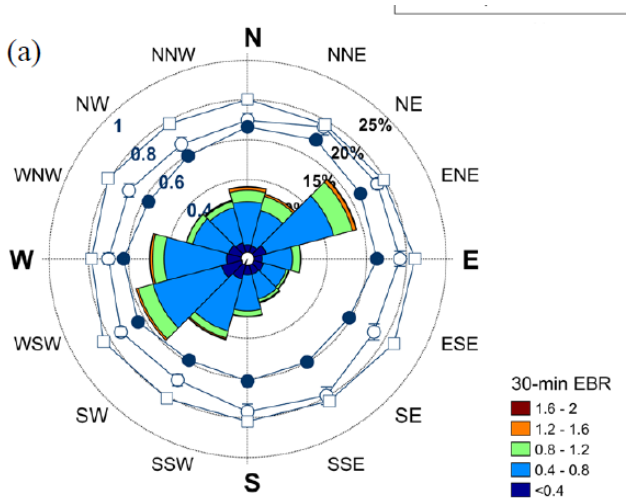


Figure 38: Proportion classes of SEB closure according to the upwind direction in Lonzée (Boland, 2019)

On a scale larger than 2 km, heterogeneities on Lonzée South from the tower are the N4 road axis and the urban area of Lonzée. On an larger scale (more than 10 km), it is also the direction of stronger heterogeneity since there is a river basin. From the satellite photos on Lonzée, it can be seen that the crop fields in the region 3 km around the tower are of length $\approx$ 300 m. Heterogeneities of scales $\approx$ 6 km are the river basin in the North-West and in the South. The proximity with these zones of potential downdraft might explain why the tower is situated in a zone of vertical updraft.

#### 5.2.0.3 Spatial heteroegenity in Vielsalm

In Vielsalm, the surface in a range of 10 km around the tower is constituted by a mix of forests and meadows. Mixed forests prevail in the West direction up to 10 km away from the tower and meadows which prevail in the NNE. Since forests evapotranspirate more and have a lower albedo than grasslands, this could explain why $CO_2$, temperature and $H_2O$ fluxes are stronger (see the value of ogives and Table 2) on Vie_22-06-12 compared to Vie_22-08-08 and Vie_22-08-09 when wind flows from the NNE, but no other major difference in the dimensions or the nature of heterogeneities can be made with this simple visual analysis.

# 6 Future perspectives

## 6.1 Extending the averaging period

In the present paper, time-series of 14 hours allowed to include oscillations of periods up to 3.2 hours with little edge effects, and this averaging period (in the frequency domain) was determined by computational requirements, in particular computer short-term memory. The use of a discrete wavelet basis such as Haar could reduce significantly computational requirements (Farge, 1992) and allow to extend the averaging time.

## 6.2 Stationarity tests

EC yields accurate values of flux when there are no motions of periods greater than 30 min, which are to the present day most often detected with the stationarity test of Foken and Wichura (1996) — FW in the present paper. However, results of the present paper show that it often failed to detect mesoscale motions. Tests assessing the statistical moment of the second order could be used together with FW to better detect mesoscale motions, maybe with different thresholds. In general, a better data selection would allow to use EC (which requires much less computational power than wavelets) for the periods it is suitable for, but an alternative method has to be used for the data that is not processed with EC. Otherwise, one unwanted outcome could be that stationarity tests majorly flag specific events as in Göckede et al. (2019) (Fig. 39), which would lead to selective exclusion of such events and e.g. undermine the accuracy of long-term budgets.

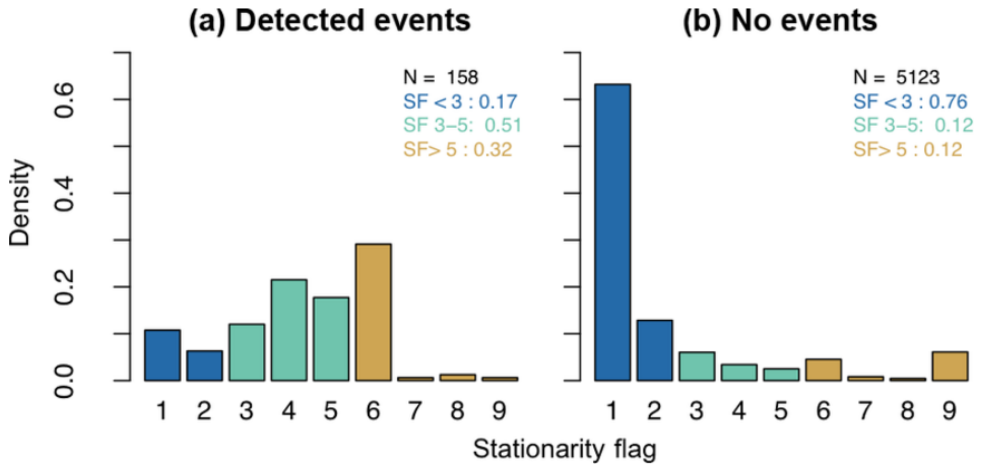


Figure 39: Stationarity flags (SF) on half-hourly records when outbursts of $CH_4$ were detected (left) and not detected (right). SF < 3, SF 3-5 and SF > 5 correspond respectively to states of high, medium and low stationarity (Göckede et al., 2019)

## 6.3 Spatial measurements

The investigation of quasi-stationary motions could be brought further by complementing tower measurements with spatial ones. LiDAR and drones are two techniques of minimal cost (compared to aircraft measurements) and installation efforts (compared to multiple tower sets) that could be implemented on Lonzée where there are no trees and where the bias due to quasi-stationary motions is most suspected. Additionally, LES imitating the heterogeneities on Lonzée as in Prabha et al. (2007b) could allow to observe formation of convective structures and variations of environmental conditions such as strong and weak wind, different wind direction and different radiative forcing. This could be complemented by an assessment of the heterogeneity of land cover in a range of 10 km, by computing the indexes of variation of the plant cover on that surface as in Stoy et al. (2013).

# 7 Summary and conclusions

The first objective of the present paper was to adapt the formula of wavelet covariance proposed by Schaller et al. (2017) so that it yields results comparable to EC for stationary 30-min temperature and

$CO_2$ flux records ($w'c'$).

Sensitivity analysis performed on 238 half-hourly stationary records showed that the accuracy of the wavelet covariance calculated with the Morlet wavelet normalized in $L^2$ depends on the minimal analyzed period $\text{Period}_{\text{min}}$, the scale step $\delta j$, the threshold for the cone of influence *qcoi*, while padding the edges of the time-series with artificial values is not recommended for this calculation since it yields either comparable or worse results than no padding at all. Unsurprisingly, the smallest values $\text{Period}_{\text{min}}$ and $\delta j$ (equal to $\delta t$ for both parameters) improved the accuracy and precision of wavelet covariance since they provided the best resolution of wavelet cross-coefficients. The sensitivity analysis of the covariance with respect to *qcoi* highlighted that the restrictiveness of the COI should be determined by the compromise of capturing low-frequency components but excluding edge effects. $qcoi = 0.10$ was evaluated as the best choice for half-hourly records, but a more restrictive (smaller) threshold could be more suitable when the averaging time is longer. Further, with these values, the covariance calculated with the Morlet normalized in $L^1$ provided the best results compared to a $L^2$ normalization and to the Mexican hat wavelet, but precautions should be made with this conclusion since the covariance was optimized with Morlet, and other values of parameters could be better adapted to the Mexican hat wavelet.

The second objective of the study was to investigate the presence of mesoscale components in turbulent fluxes which are, to the present day, the main suspects for SEB unclosure according to review papers (Foken, 2008; Mauder et al., 2020). For this purpose, flux cross-scalograms, cospectra and ogives were derived from wavelet cross-coefficients of the signals of vertical wind velocity $w$ and either temperature, $CO_2$ or $H_2O$ concentration measured with an EC system two ICOS sites in Belgium (Lonzée and Vielsalm). 14-hour long time-series were used to compute wavelet coefficients, which allowed to capture oscillation periods as high as 3.2 hours (corresponding to the border of the $\text{COI}_{0.10}$) without predominating edge effects. The observation of edge effects was eased since they resulted in discontinuities of the wavelet coefficients in places where portions of the cross-scalograms where concatenated.

Results showed that regardless of steady-state conditions of flow certified with three tests, mesoscale components were detected in almost every analyzed record. Mesoscale components were of low magnitude accordingly to previous studies (Finnigan et al., 2003; Mauder et al., 2007a, Paleri et al., 2022), but nonetheless represented a very large portion of the total flux, much larger than the SEB residual on the days of the analysis. The fact that ogives did not converge even in the low-frequency ranges lead to the suspicion that the estimation of the total flux (containing oscillations of periods up to 3.2 hours) was inaccurate (Foken et al., 2006a), in other words, flux cospectra should vanish when the averaging period is sufficient. For the four dates on which ogives oscillate, it is hypothesised that the non-convergent records could converge for a longer averaging period. However, the consistently growing ogives in the low-frequency (i.e. high periodic) ranges on the remaining two dates lead to think that the fluxes are probably overestimated on these two days due to the presence of updrafting quasi-stationary motions passing through the measurement point, and it is not excluded that the observational bias would also have contaminated the flux cospectra on the four other dates. Up to now, the bias that quasi-stationary motions introduce in single-point measurements has been mainly been theoretically discussed (Lee, 1998; Finnigan, 1999) or studied with numerical simulations of the flow (Patton et al., 2005; Inagaki et al., 2006; Prabha et al., 2007b; Lothon et al., 2007) but is still poorly understood in real conditions (Mauder et al., 2010), so further investigations e.g. with

spatial EC measurements (Mauder et al., 2007a, Paleri et al., 2022) are needed to determine if they are present and to understand their potential structure on Lonzée and Vielsalm. The moderate mean wind conditions and the heterogeneities on these two sites could explain the formation of convective mesoscale structures at scales larger than the boundary layer depth, but the analysis in the present paper does not allow to ascertain it.

pagebreak

# 8 Appendices

## 8.1 Requirement of stationarity of flow for EC

### 8.1.1 Applicability of Reynolds decomposition

Reynolds decomposition is the partitioning of a variable into an average and a fluctuant component (Eq.4). This allows to separate the flow into a mean component, that is considered a background flow, and the fluctuations, that we consider are due to turbulence (Kaimal and Finnigan, 1994, p. 162).

The rules of ensemble averaging (denoted here with angle brackets) for two quantities, for example $w$ and c, notably imply that (Kaimal and Finnigan, 1994, p.276):

1. $\langle c' \rangle = 0$
2. $\langle w' \langle c \rangle \rangle = 0$

Where $w$ and $c$ can be inverted without interfering with the validity of the equations. These rules are essential for simplifications that are systematically made to derive the scalar budget equation.

A priori, Reynolds decomposition is only valid under ensemble averaging (Kaimal and Finnigan, 1994, p.276). Broadly speaking, ensemble averaging is the computation of statistical moments from the sampled distribution of a random variable whose realizations are produced by N identical experiments. Typically, ensemble averages are calculated on data stemming from laboratory experiments, since these experiments are controlled and reproduced exactly (Stull, 1988). However, when atmospheric variables such as wind velocity and gas concentrations are sampled continuously from a tower, their values depend on time: the wind velocity at a certain time t is likely to be close to the velocity at the next sampling instant, which is t+0.05 s if the sampling frequency is 20Hz. Hence, averaging such values gives temporal averages. In order to apply Reynolds decomposition, time averages can be substituted to ensemble averages under the assumption that both averaging methods are equivalent, which is equivalent to the ergodic hypothesis. But this hypothesis is only verified for stationary time-series: in this case only are Reynolds postulates verified (Kaimal and Finnigan, 1994, p.276). This necessitates a thorough definition of stationarity and a rigorous method to test it. A parenthesis is worth making to emphasis that although WT can capture instationary power (Farge, 1992; Katul et al., 1994), it is not clear whether WT allows to calculate the total covariance $\overline{wc}$ or only its fluctuations $\overline{w'c'}$. According to Howell and Mahrt (1997), WT satisfies Reynolds postulates, so it is anyhow suitable to calculate $\overline{w'c'}$. However, if the ergodic hypothesis – verified when the time-series is stationary – is not verified, Reynolds decomposition for the other terms of the scalar budgets could be questioned. These considerations do not aim to question the exactitude of XWT to calculate the tur-

bulent flux term, since this has been proven by the numerous studies employing it (e.g. Mauder et al., 2007a). Rather, it raises the question of the theoretical fundaments that allow wavelets to replace $Cov_{EC}$ for instationary time-series.

### 8.1.2 The hypothesis of stationarity of flow

Roughly, stationarity is the property of a time-series to have statistical parameters that are constant over time. Finnigan and Kaimal (1994) define the stationary of time-series as the condition that their (co)variances approach stable values when the averaging time T is increased. Stationarity can be defined for moments of different orders. Studying the (co)variance of the means within a time-series assimilates to evaluating the stationarity of the first order. This type of stationarity can be tested with the commonly used test of Foken and Wichura (1996) (FW). Studying the variance of the variances corresponds to the stationarity of the second order. This order of stationarity is tested by the tests of Dutaur (1999) (DU) or Marht (1998) (MA). These tests are presented in Appendix 8.3.

Regardless of the order, stationarity depends on the averaging period T, which should therefore be chosen wisely. The minimal record period must be such that the averages of the highly fluctuating times series of *w* and *c* reach sufficiently stable values (Kaimal and Finnigan, 1994, p. 255). It can be calculated with a statistical approach described in Appendix 8.2. Additionally, significant components of periods greater than the record period must be excluded. This is achieved by setting the averaging period (hereby synonym of the record period) to the cospectral gap. In general, it is chosen as 30 min, satisfying both the minimal and maximal requirements. Still, the steady-state is jeopardized when the cospectral gap is not clearly present (e.g. McNaughton and Laubach, 2000).

## 8.2 Minimal averaging time for traditional EC processing

To assess the stationarity, Kaimal and Finnigan (1994, p.255) propose the following method: first, the record of period T is divided into small intervals $\alpha$ of period $T_\alpha$ (e.g. $T_\alpha = 10s$). Taking many small intervals, it is possible to calculate $\sigma^2_{\overline{\alpha}}$ , the ensemble variance of their time averages – to test the stationarity of the first order. If $\sigma^2_{\overline{\alpha}}$ is small enough, the time-series is considered stationary over the time interval T. $\sigma^2_{\overline{\alpha}}$ can be computed thanks to the variance of a small interval $\sigma^2_\alpha$ (Lumley and Panofsky, 1994) following:

$$\sigma^2_{\overline{\alpha}} \approx \frac{2\sigma^2_\alpha T_\alpha}{T} \tag{29}$$

Hence, if the averaging time T is chosen sufficiently big, the variance of the means is negligible, and the time-series is considered stationary. If we consider an acceptable error $\varepsilon = \frac{\sigma_{\overline{\alpha}}}{\alpha}$ smaller than a certain value (say 0.02), then we can compute the minimal averaging time T. For example, for a signal mean wind velocity $\overline{U} = 5ms^{-1}$, standard deviation $1ms^{-1}$, a segmentation period $T_\alpha = 10s$ , and an acceptable error of 0.02, the minimal averaging time period is 2000 seconds, which is close to 30 min. Lumley and Panofsky (1964) show that the minimal averaging period is approximately five times longer to verify the stationarity of the fourth order with the same acceptable error.

## 8.3 Stationarity tests

The three following stationarity tests were described in Fortuniak et al. (2013). The test proposed by Foken and Wichura (1996) tests the stationarity of the first order, i.e. the variability of the average covariance. The test is computed as follows : the 30-min record of $w'c'$ is divided into I (I = 6) 5-min segments, and the covariance of each segment $\overline{w'c'}_{5min}$ is calculated. The average of these covariances is compared to the total covariance of the 30-min record :

$$RN_{cov} = \frac{\sum_{i=1}^{I}(\overline{w'c'}_{5min})_i/I - \overline{w'c'}_{30min}}{\overline{w'c'}_{30min}} \tag{30}$$

The record is considered stationary if the computed value $RN_{cov} < 0.3$.

The test proposed by Mahrt (1998) assesses the stationarity of the second order. To this end, the 30-min record is divided into I=6 segments, and each of them are divided into J=6 sub-segments. The covariance of each sub-segment is calculated. The standard deviation of the covariances of the sub-segments ($\sigma_{within,i}$) are computed separately for each segment. The standard deviations of the sub-segment covariances are then averaged. The bigger the standard deviation of the covariances, the most likely is the time-series to be stationary, since the variation is within a sub-segment of 5 minutes is high.

$$RE = \frac{1}{I\sqrt{J}} \sum_{i=1}^{I} \sigma_{within,i} \tag{31}$$

Then the covariance within each segment $\overline{w'c'}_{10min}$ is computed, and the standard deviation of these covariances ($\sigma_{btw}$) is also calculated. Bigger values of $\sigma_{btw}$ imply a larger variability of the covariance over the whole period, and thus less stationarity. The *"Non-Stationarity ratio"* (*NR*; Mahrt, 1998) is calculated following :

$$NR = \frac{\sigma_{btw}}{RE} \tag{32}$$

The record is considered instationary if $NR > 2$.

The test proposed by Dutaur et al. (1999) and Nemitz et al. (2002) assesses the function of cumulated covariance over time $I(t)$ :

$$I(t) \; = \; \frac{1}{T} \int_0^t w'c' \; dt \tag{33}$$

This function is linear when the period is stationary. For this reason, Dutaur proposes to assess the quality of the linear regression of this function. The standard deviation of the residuals of the linear regression ($\sigma_{reg}$) reflects its non-linearity. The ratio of $\sigma_{reg}$ normalized by the covariance over the 30-min period, defines the relative covariance stationarity coefficient (*RSCS*), which is greater when the linear regression is of poor quality, i.e. when the 30-min period is instationary :

$$RSCS = \frac{2\sigma_{reg}}{\overline{w'c'}_{30min}} \tag{34}$$

The threshold proposed by Nemitz is $RSCS = 0.2$, above which the data is considered non-stationary.

## 8.4 Classification of atmospheric motions according to scale

Sun et al. (1996) proposed to partition the flux into three categories based on characteristics of scale dependence. According to them, turbulent, large-eddy, and mesoscale fluxes are due to motions of scales respectively smaller than 1 km, between 1 and 5 km, and greater than 5 km. Building on the hypothesis that motions are defined by 'active' and 'inactive' components, McNaughton and Laubach (2000) partitioned fluxes into three groups.

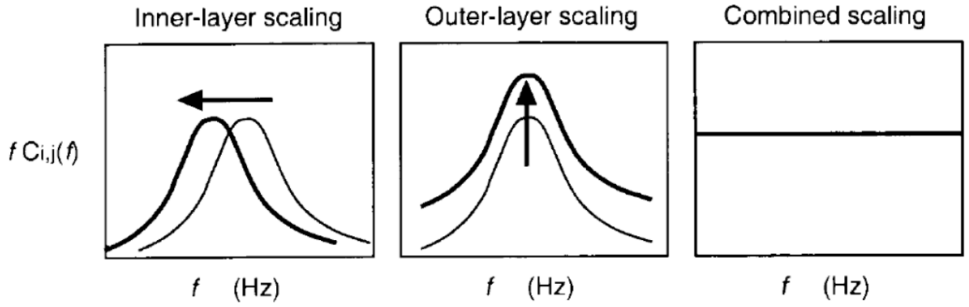


*Figure 2.* Schematic spectra of fluctuating quantities with arrows showing the effect of an increase in observation height, $z$, (a) (left-hand side) a spectrum with amplitude insensitive to observation height, as predicted by inner layer scaling (ILS); (b) (centre) a spectrum with position on the frequency axis insensitive toheight, as predicted by outer-layer scaling (OLS); (c) a spectrum with both amplitude and position on the frequency axis insensitive to height, as predicted for combined scaling (CS).

Figure 40: McNaughton and Laubach, 2000

The first group is outer-layer scaling (OLS), it corresponds to the mean flow and contains only inactive components, i.e. that cannot transfer momentum. OLS components are inactive because their major component is horizontal, and their vertical component is 90° out of phase with other fluctuations, which means that the vertical component is maximal when other components are 0. The second group is inner-layer scaling (ILS) and contains only active components, i.e. can transfer momentum and are responsible for turbulent flows. The third group is combined scaling (CS) and results of the interaction of the first two groups and represents the mesoscale range. The classification draws on the analysis of spectral behavior with respect to similarity parameters such as height and horizontal wind. In particular, spectral dependencies to measurement height are of different nature for these groups (depicted in Fig. 40). Under the presence of a cospectral gap, active and inactive components do not interact. On the contrary, the presence of interaction results in CS motions but no cospectral gap. Compared to other classification schemes, McNaughton and Laubach's approach is more connected to the underlying physics, it can notably explain the transfer of momentum from one type of motion to another (section 6).

## 8.5 Cross-scalograms in the low-frequency range

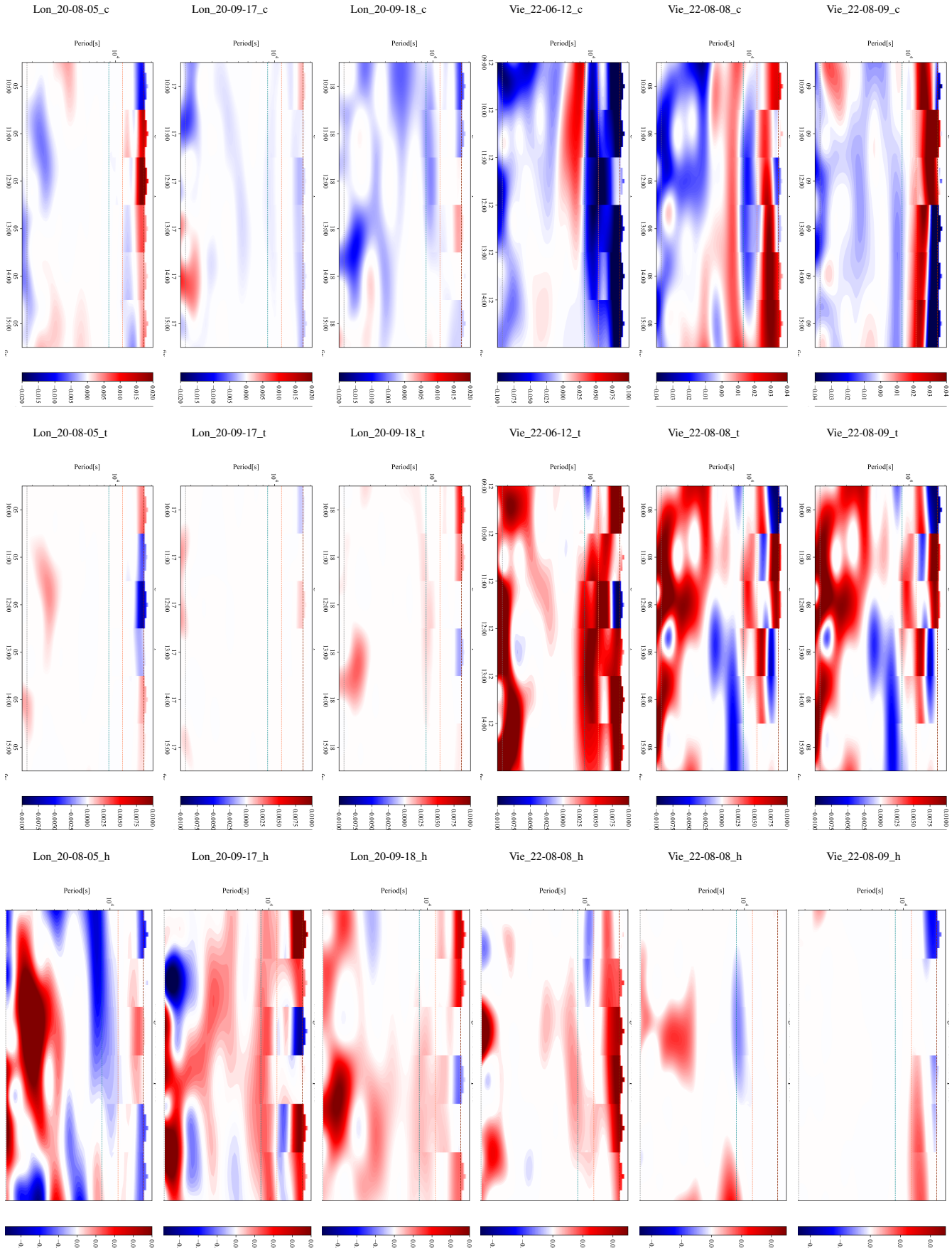


Figure 41: cross-scalograms of the periods > 30 min for all records. The colors are adapted to low magnitudes of wavelet coefficients and the COI lines are the same as in Fig. 26. The cross-scalograms are shifted by 90°on the right and the records are displayed in six columns according to the date and in three rows according to the scalar

## 8.6 EBR

. Half-hourly fluxes computed with EC processed come from two sources : data from the Carbon Portal is available online (https://data.icos-cp.eu/portal/) and the PI[5]-processed data is available on demand on an internal server to ICOS.

EBR of the period 09:00-16:00 (local time) for each day of the analysis are calculated from these half-hourly fluxes (Table 4). Both data sources use the same EC measurements described in ICOS reports (see 2.4), but different processing methods for the obtention of half-hourly fluxes consequence in different residuals for both sources. Methods for PI-processed fluxes are described in Moureaux et al. (2006), De Ligne et al. (2010) and Aubinet et al. (2001). EBR calculated from both sources differs mostly for the site of Lonzée, where the EBR is close to 100% according to CP but is only about 75% according to Biodyne. On Vielsalm, the differences in EBR are much less important.

Table 4: Energy balance ratio (EBR) calculated for each date between 9:00 and 16:00 local time (UTC+1). Half-hourly fluxes for the calculation of EBR are provided by the Carbon Portal (CP) or PI-processed from ICOS (L2)

| Site | Date | Source | EBR [%] |
|---|---|---|---|
| Lonzée | 20-08-05 | CP | 96 |
| | | L2 | 73 |
| | 20-09-17 | CP | 97 |
| | | L2 | 77 |
| | 20-09-18 | CP | 98 |
| | | L2 | 73 |
| Vielsalm | 22-06-12 | CP | 83 |
| | | L2 | 86 |
| | 22-08-08 | CP | 73 |
| | | L2 | 76 |
| | 22-08-09 | CP | 79 |
| | | L2 | 78 |

## 8.7 Combination of spatial and temporal averaging in a case study

The works of Mauder et al. (2008, 2010) calculated turbulent fluxes with the EC method combining temporal averaging and spatial averaging on measurements implemented with a setup of 25 slow-response towers. The study of 2010 focused on the attempt to close the SEB closure by attempting the combination of spatial and temporal averaging (Eq. 28).

However, the SEB unclosure was not attenuated with this setup. Essentially, sensible heat fluxes obtained with combined averaging were greater than those obtained with standard temporal averaging, but latent heat fluxes were smaller with the combined method compared to the standard method. Mauder et al. (2010) attribute the remaining error to the fact that the site was horizontally heterogeneous, and according to them, the vertical advection is heterogenous and should be assessed at different points in space in order to reduce the error. Nonetheless, they argue that the problem of horizontal heterogeneity is largely reduced by aircraft measurements, because the measurement height is more important.

[5]Principal Investigator

# 9 Bibliography

Attié, J.-L. and Durand, P. (2003) 'Conditional Wavelet Technique Applied to Aircraft Data Measured in the Thermal Internal Boundary Layer During Sea-Breeze Events', Boundary-Layer Meteorology, 106(3), pp. 359–382. Available at: https://doi.org/10.1023/A:1021262406408.

Aubinet, M. et al. (2001) 'Long term carbon dioxide exchange above a mixed forest in the Belgian Ardennes', Agricultural and Forest Meteorology, 108, pp. 293–315. Available at: https://doi.org/10.1016/S0168-1923(01)00244-1.

Aubinet, M., Vesala, T. and Papale, D. (eds) (2012) Eddy Covariance: A Practical Guide to Measurement and Data Analysis. Dordrecht: Springer Netherlands. Available at: https://doi.org/10.1007/978-94-007-2351-1.

Bitton, J. (2019) Analyse multi-échelle de l'évolution des flux de chaleur sensible et latente échangés ente un écosystème forestier et l'atmosphère au moyen de la transformée en ondelettes continue. University of Liège.

Boland, F. (2019) Analyse pluriannuelle des mécanismes influençant la qualité de mesure par covariance de turbulence de flux énergétiques d'un agroécosystème dynamique : Cas d'une grande culture à Lonzée en Hesbaye. University of Liège. Available at: http://hdl.handle.net/2268.2/8441.

Burba, G. and Anderson, D. (2010) A Brief Practical Guide to Eddy Covariance Flux Measurements: Principles and Workflow Examples for Scientific and Industrial Applications. LI-COR Biosciences. Available at: https://doi.org/10.13140/RG.2.1.1626.4161.

Butterworth, B.J. et al. (2021) 'Connecting Land–Atmosphere Interactions to Surface Heterogeneity in CHEESEHEAD19', Bulletin of the American Meteorological Society, 102(2), pp. E421–E445. Available at: https://doi.org/10.1175/BAMS-D-19-0346.1.

Dalu, G.A. et al. (1996) 'Heat and Momentum Fluxes Induced by Thermal Inhomogeneities with and without Large-Scale Flow', Journal of the Atmospheric Sciences, 53(22), pp. 3286–3302. Available at: https://doi.org/10.1175/1520-0469(1996)053<3286:HAMFIB>2.0.CO;2.

De Ligne, A., Heinesch, B. and Aubinet, M. (2010) 'New Transfer Functions for Correcting Turbulent Water Vapour Fluxes', Boundary-Layer Meteorology, 137(2), pp. 205–221. Available at: https://doi.org/10.1007/s10546-010-9525-9.

Desjardins, R.L. et al. (1997) 'Scaling up flux measurements for the boreal forest using aircraft-tower combinations', Journal of Geophysical Research: Atmospheres, 102(D24), pp. 29125–29133. Avail-

able at: https://doi.org/10.1029/97JD00278.

Dupont, S. (2020) 'Scaling of Dust Flux With Friction Velocity: Time Resolution Effects', Journal of Geophysical Research: Atmospheres, 125(1), p. e2019JD031192. Available at: https://doi.org/10.1029/2019JD031192.

Dutaur, L. et al. (1999) 'The Detection of non-stationarity in the Determination of Deposition Fluxes', Transactions on Ecology and the Environment, 28.

Einaudi, F. and Finnigan, J.J. (1993) 'Wave-Turbulence Dynamics in the Stably Stratified Boundary Layer', Journal of the Atmospheric Sciences, 50(13), pp. 1841–1864. Available at: https://doi.org/10.1175/1520-0469(1993)050<1841:WTDITS>2.0.CO;2.

Etling, D. and Brown, R.A. (1993) 'Roll vortices in the planetary boundary layer: A review', Boundary-Layer Meteorology, 65(3), pp. 215–248. Available at: https://doi.org/10.1007/BF00705527.

Farge, M. (1992) 'Wavelet Transforms and Their Applications to Turbulence', Annual Review of Fluid Mechanics, 24(1), pp. 395–458. Available at: https://doi.org/10.1146/annurev.fl.24.010192.002143.

Finnigan, J. (1999) 'A comment on the paper by Lee (1998): "On micrometeorological observations of surface-air exchange over tall vegetation"', Agricultural and Forest Meteorology, 97(1), pp. 55–64. Available at: https://doi.org/10.1016/S0168-1923(99)00049-0.

Finnigan, J.J. et al. (2003) 'A Re-Evaluation of Long-Term Flux Measurement Techniques Part I: Averaging and Coordinate Rotation', Boundary-Layer Meteorology, 107(1), pp. 1–48. Available at: https://doi.org/10.1023/A:1021554900225.

Foken, T., Mauder, M., et al. (2006) 'Attempt to close the energy balance for the LITFASS-2003 experiment.'

Foken, T., Wimmer, F., et al. (2006) 'Some aspects of the energy balance closure problem', Atmospheric Chemistry and Physics, 6(12), pp. 4395–4402. Available at: https://doi.org/10.5194/acp-6-4395-2006.

Foken, T. (2008) 'The Energy Balance Closure Problem: An Overview', Ecological Applications, 18(6), pp. 1351–1367. Available at: https://doi.org/10.1890/06-0922.1.

Foken, Th. and Wichura, B. (1996) 'Tools for quality assessment of surface-based flux measure-

ments', Agricultural and Forest Meteorology, 78(1), pp. 83–105. Available at: https://doi.org/10.1016/0168-1923(95)02248-1.

Fortuniak, K., Pawlak, W. and Siedlecki, M. (2013) 'Integral Turbulence Statistics Over a Central European City Centre', Boundary-Layer Meteorology, 146(2), pp. 257–276. Available at: https://doi.org/10.1007/s10546-012-9762-1.

Franz, D. et al. (2018) 'Towards long-term standardised carbon and greenhouse gas observations for monitoring Europe´s terrestrial ecosystems: a review', International Agrophysics, 32(4), pp. 439–455. Available at: https://doi.org/10.1515/intag-2017-0039.

Göckede, M., Kittler, F. and Schaller, C. (2019) 'Quantifying the impact of emission outbursts and non-stationary flow on eddy-covariance CH4 flux measurements using wavelet techniques', Biogeosciences, 16(16), pp. 3113–3131. Available at: https://doi.org/10.5194/bg-16-3113-2019.

Haugen (1978) 'Fourth Symposium on Meteorological Observations and Instrumentation of the American Meteorological Society, April 10–14, 1978, Denver, Colo.', in Bulletin of the American Meteorological Society. American Meteorological Society, pp. 93–126. Available at: http://www.jstor.org/stable/26217895 (Accessed: 15 August 2023).

Higgins, C.W. et al. (2013) 'Measured and Estimated Water Vapor Advection in the Atmospheric Surface Layer', Journal of Hydrometeorology, 14(6), pp. 1966–1972. Available at: https://doi.org/10.1175/JHM-D-12-0166.1.

Hiraishi, T. (ed.) (2014) 2013 revised supplementary methods and good practice guidance arising from the Kyoto Protocol. Geneva, Switzerland: Intergovernmental Panel on Climate Change.

Howell, J.F. and Mahrt, L. (1997) 'Multiresolution Flux Decomposition', Boundary-Layer Meteorology, 83(1), pp. 117–137. Available at: https://doi.org/10.1023/A:1000210427798.

Hudgins, L., Friehe, C.A. and Mayer, M.E. (1993) 'Wavelet transforms and atmopsheric turbulence', Physical Review Letters, 71(20), pp. 3279–3282. Available at: https://doi.org/10.1103/PhysRevLett.71.3279.

ICOS (2017) 'ICOS Ecosystem Station Labelling Report - Station: BE-Lon (Lonzee)'. Available at: https://meta.icos-cp.eu/objects/eo_cBxOeMONH2G8z4g0G_60J.

ICOS (2020) 'ICOS Ecosystem Station Labelling Report - Station: BE-Vie (Vielsalm)'. Available at: https://data.icos-cp.eu/objects/xiiL_kyPVoN35ecLfEMOPrEV.

Inagaki, A. et al. (2006) 'Impact of Surface Heterogeneity on Energy Imbalance: A Study Using LES', Journal of the Meteorological Society of Japan. Ser. II, 84(1), pp. 187–198. Available at: https://doi.org/10.2151/jmsj.84.187.

Kaimal, J.C. and Finnigan, J.J. (1994) Atmospheric boundary layer flows: their structure and measurement. New York: Oxford University Press.

Kanda, M. et al. (2004) 'LES Study of the Energy Imbalance Problem with Eddy Covariance Fluxes', Boundary-Layer Meteorology, 110(3), pp. 381–404. Available at: https://doi.org/10.1023/B:BOUN.0000007225.45548.7a.

Katul, G.G. et al. (1994) 'Intermittency in Atmospheric Surface Layer Turbulence: The Orthonormal Wavelet Representation', in E. Foufoula-Georgiou and P. Kumar (eds) Wavelet Analysis and Its Applications. Academic Press (Wavelets in Geophysics), pp. 81–105. Available at: https://doi.org/10.1016/B978-0-08-052087-2.50009-8.

Kirby, J.F. and Swain, C.J. (2013) 'Power spectral estimates using two-dimensional Morlet-fan wavelets with emphasis on the long wavelengths: jackknife errors, bandwidth resolution and orthogonality properties', Geophysical Journal International, 194(1), pp. 78–99. Available at: https://doi.org/10.1093/gji/ggt103.

Klosterhalfen, A. et al. (2019) 'Sensitivity analysis of a source partitioning method for H2O and CO2 fluxes based on high frequency eddy covariance data: Findings from field data and large eddy simulations', Agricultural and Forest Meteorology, 265, pp. 152–170. Available at: https://doi.org/10.1016/j.agrformet.2018.11.003.

Lee, X. (1998) 'On micrometeorological observations of surface-air exchange over tall vegetation', Agricultural and Forest Meteorology, 91(1), pp. 39–49. Available at: https://doi.org/10.1016/S0168-1923(98)00071-9.

Lee, X. (ed.) (2004) Handbook of micrometeorology: a guide for surface flux measurement and analysis. Dordrecht: Kluwer Acad. Publ (Atmospheric and oceanographic sciences library, 29).

Lee, X., Massman, W. and Law, B. (2004) Handbook of Micrometeorology: a guide for surface flux measurement and analysis. Dordrecht Boston: Kluwer (Atmospheric and cceanographic sciences library, 29).

Li, Y. et al. (2023) 'Quantitative Evaluation of Wavelet Analysis Method for Turbulent Flux Calculation of Non-Stationary Series', Geophysical Research Letters, 50(5), p. e2022GL101591. Available at: https://doi.org/10.1029/2022GL101591.

Lothon, M. et al. (2007) 'Impact of coherent eddies on airborne measurements of vertical turbulent fluxes', Boundary-Layer Meteorology, 124(3), pp. 425–447. Available at: https://doi.org/10.1007/s10546-007-9182-9.

Lumley, J.L. and Panofsky, H.A. (1964) The Structure of Atmospheric Turbulence. Interscience Publishers. Moureaux, C. et al. (2006) 'Annual net ecosystem carbon exchange by a sugar beet crop', Agricultural and Forest Meteorology, 139(1), pp. 25–39. Available at: https://doi.org/10.1016/j.agrformet.2006.05

Mader, S. (2020) 'Plant trees for the planet: the potential of forests for climate change mitigation and the major drivers of national forest area', Mitigation and Adaptation Strategies for Global Change, 25(4), pp. 519–536. Available at: https://doi.org/10.1007/s11027-019-09875-4.

Mahrt, L. (1998) 'Flux Sampling Errors for Aircraft and Towers', Journal of Atmospheric and Oceanic Technology, 15(2), pp. 416–429. Available at: https://doi.org/10.1175/1520-0426(1998)015<0416:FSEFAA>2.0.CO;2.

Mahrt, L. et al. (2001) 'Dependence of Turbulent and Mesoscale Velocity Variances on Scale and Stability', Journal of Applied Meteorology and Climatology, 40(3), pp. 628–641. Available at: https://doi.org/10.1175/1520-0450(2001)040<0628:DOTAMV>2.0.CO;2.

Mahrt, L. (2010) 'Computing turbulent fluxes near the surface: Needed improvements', Agricultural and Forest Meteorology, 150(4), pp. 501–509. Available at: https://doi.org/10.1016/j.agrformet.2010.01.015.

Mauder, M. et al. (2006) 'Processing and quality control of flux data during LITFASS-2003', Boundary-Layer Meteorology, 121(1), pp. 67–88. Available at: https://doi.org/10.1007/s10546-006-9094-0.

Mauder, M. et al. (2007) 'Surface energy balance measurements at a tropical site in West Africa during the transition from dry to wet season', Theoretical and Applied Climatology, 89(3), pp. 171–183. Available at: https://doi.org/10.1007/s00704-006-0252-6.

Mauder, M. et al. (2008) 'Measurement of the Sensible Eddy Heat Flux Based on Spatial Averaging of Continuous Ground-Based Observations', Boundary-Layer Meteorology, 128(1), pp. 151–172. Available at: https://doi.org/10.1007/s10546-008-9279-9.

Mauder, M. et al. (2010) 'An Attempt to Close the Daytime Surface Energy Balance Using Spatially-Averaged Flux Measurements', Boundary-Layer Meteorology, 136(2), pp. 175–191. Available at: https://doi.org/10.1007/s10546-010-9497-9.

Mauder, M., Desjardins, R.L. and MacPherson, I. (2007) 'Scale analysis of airborne flux measurements over heterogeneous terrain in a boreal ecosystem', Journal of Geophysical Research: Atmospheres, 112(D13), p. 2006JD008133. Available at: https://doi.org/10.1029/2006JD008133.

Mauder, M., Foken, T. and Cuxart, J. (2020) 'Surface-Energy-Balance Closure over Land: A Review', Boundary-Layer Meteorology, 177(2), pp. 395–426. Available at: https://doi.org/10.1007/s10546-020-00529-6.

McNaughton, K.G. and Laubach, J. (2000) 'Power Spectra and Cospectra for Wind and Scalars in a Disturbed Surface Layer at the Base of an Advective Inversion', Boundary-Layer Meteorology, 96(1), pp. 143–185. Available at: https://doi.org/10.1023/A:1002477120507.

Mercatoris, M. (2021) 'Environmental metrology chapter 4 - Signal processing'.

Metzger, S. et al. (2013) 'Spatially explicit regionalization of airborne flux measurements using environmental response functions', Biogeosciences, 10(4), pp. 2193–2217. Available at: https://doi.org/10.5194/bg-10-2193-2013.

Meyers, S.D., Kelly, B.G. and O'Brien, J.J. (1993) 'An Introduction to Wavelet Analysis in Oceanography and Meteorology: With Application to the Dispersion of Yanai Waves', Monthly Weather Review, 121(10), pp. 2858–2866. Available at: https://doi.org/10.1175/1520-0493(1993)121<2858:AITWAI>2.0.CO;2.

Misztal, P.K. et al. (2014) 'Airborne flux measurements of biogenic isoprene over California', Atmospheric Chemistry and Physics, 14(19), pp. 10631–10647. Available at: https://doi.org/10.5194/acp-14-10631-2014.

Moureaux, C. (2004) Conception et mise au point d'un système de mesure des flux de CO2 échangés par une culture agricole. University of Liège.

Moureaux, C. et al. (2006) 'Annual net ecosystem carbon exchange by a sugar beet crop', Agricultural and Forest Meteorology, 139(1), pp. 25–39. Available at: https://doi.org/10.1016/j.agrformet.2006.05.009.

Nemitz, E. et al. (2002) 'Micrometeorological Measurements of the Urban Heat Budget and CO 2 Emissions on a City Scale', Environmental science & technology, 36, pp. 3139–46. Available at: https://doi.org/10.1021/es010277e.

Nobach, H. et al. (2007) 'Review of Some Fundamentals of Data Processing', in C. Tropea, A.L. Yarin, and J.F. Foss (eds) Springer Handbook of Experimental Fluid Mechanics. Berlin, Heidelberg:

Springer (Springer Handbooks), pp. 1337–1398. Available at: https://doi.org/10.1007/978-3-540-30299-5_22.

Nordbo, A. and Katul, G. (2013) 'A Wavelet-Based Correction Method for Eddy-Covariance High-Frequency Losses in Scalar Concentration Measurements', Boundary-Layer Meteorology, 146(1), pp. 81–102. Available at: https://doi.org/10.1007/s10546-012-9759-9.

Oncley, S.P. et al. (2007) 'The Energy Balance Experiment EBEX-2000. Part I: overview and energy balance', Boundary-Layer Meteorology, 123(1), pp. 1–28. Available at: https://doi.org/10.1007/s10546-007-9161-1.

Orlanski, I. (1975) 'A Rational Subdivision of Scales for Atmospheric Processes on JSTOR', Bulletin of the American Meteorological Society, 56, pp. 527–530.

Paleri, S. et al. (2022) 'Space-Scale Resolved Surface Fluxes Across a Heterogeneous, Mid-Latitude Forested Landscape', Journal of Geophysical Research: Atmospheres, 127(23), p. e2022JD037138. Available at: https://doi.org/10.1029/2022JD037138.

Patton, E.G., Sullivan, P.P. and Moeng, C.-H. (2005) 'The Influence of Idealized Heterogeneity on Wet and Dry Planetary Boundary Layers Coupled to the Land Surface', Journal of the Atmospheric Sciences, 62(7), pp. 2078–2097. Available at: https://doi.org/10.1175/JAS3465.1.

Prabha, T.V. et al. (2007) 'Low-Frequency Effects on Eddy Covariance Fluxes under the Influence of a Low-Level Jet', Journal of Applied Meteorology and Climatology, 46(3), pp. 338–352. Available at: https://doi.org/10.1175/JAM2461.1.

Prabha, T.V. et al. (2008) 'Influence of Nocturnal Low-level Jets on Eddy-covariance Fluxes over a Tall Forest Canopy', Boundary-Layer Meteorology, 126(2), pp. 219–236. Available at: https://doi.org/10.1007/s10546-007-9232-3.

Prabha, T.V., Karipot, A. and Binford, M.W. (2007) 'Characteristics of secondary circulations over an inhomogeneous surface simulated with large-eddy simulation', Boundary-Layer Meteorology, 123(2), pp. 239–261. Available at: https://doi.org/10.1007/s10546-006-9137-6.

Rebmann, C. et al. (2018) 'ICOS eddy covariance flux-station site setup: a review', International Agrophysics, 32(4), pp. 471–494. Available at: https://doi.org/10.1515/intag-2017-0044.

Sabbatini, S. and Papale, D. (2017) 'ICOS Ecosystem Instructions for Turbulent Flux Measurements of CO2, Energy and Momentum'. Available at: https://doi.org/10.18160/QWV4-639G.

Saito, M. and Asanuma, J. (2008) 'Eddy Covariance Calculation Revisited with Wavelet Cospectra', Sola, 4, pp. 49–52. Available at: https://doi.org/10.2151/sola.2008-013.

Saito, M., Asanuma, J. and Miyata, A. (2007) 'Dual-scale transport of sensible heat and water vapor over a short canopy under unstable conditions', Water Resources Research, 43(5). Available at: https://doi.org/10.1029/2006WR005136.

Sakai, R.K., Fitzjarrald, D.R. and Moore, K.E. (2001) 'Importance of Low-Frequency Contributions to Eddy Fluxes Observed over Rough Surfaces', Journal of Applied Meteorology and Climatology, 40(12), pp. 2178–2192. Available at:
https://doi.org/10.1175/1520-0450(2001)040<2178:IOLFCT>2.0.CO;2.

Schaller, C. et al. (2019) 'Characterisation of short-term extreme methane fluxes related to non-turbulent mixing above an Arctic permafrost ecosystem', Atmospheric Chemistry and Physics, 19(6), pp. 4041–4059. Available at: https://doi.org/10.5194/acp-19-4041-2019.

Schaller, C., Göckede, M. and Foken, T. (2017) 'Flux calculation of short turbulent events : comparison of three methods', Atmospheric Measurement Techniques, 10(3), pp. 869–880. Available at: https://doi.org/10.5194/amt-10-869-2017.

Schobesberger, S. et al. (2023) 'Airborne flux measurements of ammonia over the southern Great Plains using chemical ionization mass spectrometry', Atmospheric Measurement Techniques, 16(2), pp. 247–271. Available at: https://doi.org/10.5194/amt-16-247-2023.

Steiner, A.L. et al. (2011) 'Analysis of coherent structures and atmosphere-canopy coupling strength during the CABINEX field campaign', Atmospheric Chemistry and Physics, 11(23), pp. 11921–11936. Available at: https://doi.org/10.5194/acp-11-11921-2011.

Steinfeld, G. et al. (2007) 'Spatial representativeness of single tower measurements and the imbalance problem with eddy-covariance fluxes: results of a large-eddy simulation study', Boundary-Layer Meteorology, 123(1), pp. 77–98. Available at: https://doi.org/10.1007/s10546-006-9133-x.

Stoy, P.C. et al. (2013a) 'A data-driven analysis of energy balance closure across FLUXNET research sites: The role of landscape scale heterogeneity', Agricultural and Forest Meteorology, 171–172, pp. 137–152. Available at: https://doi.org/10.1016/j.agrformet.2012.11.004.

Stull, R.B. (1988) An introduction to boundary layer meteorology. Dordrecht; Boston: Kluwer Academic Publishers (Atmospheric sciences library).

Sun, J. et al. (1996) 'Scale Dependence of Air-Sea Fluxes over the Western Equatorial Pacific', Journal of the Atmospheric Sciences, 53(21), pp. 2997–3012. Available at: https://doi.org/10.1175/1520-0469(1996)053<2997:SDOASF>2.0.CO;2.

Terradellas, E. et al. (2001) 'Wavelet methods: application to the study of the stable atmospheric boundary layer under non-stationary conditions', Dynamics of Atmospheres and Oceans, 34(2), pp. 225–244. Available at: https://doi.org/10.1016/S0377-0265(01)00069-0.

Torrence, C. and Compo, G.P. (1998) 'A Practical Guide to Wavelet Analysis', Bulletin of the American Meteorological Society, 79(1), pp. 61–78. Available at: https://doi.org/10.1175/1520-0477(1998)079<0061:APGTWA>2.0.CO;2.

Van Der Hoven, I. (1957) 'Power spectrum of horizontal wind speed in the frequency range from 0.0007 to 900 cycles per hour', Journal of Meteorology, 14(2), pp. 160–164. Available at: https://doi.org/10.1175/1520-0469(1957)014<0160:PSOHWS>2.0.CO;2.

Vickers, D. and Mahrt, L. (2003) 'The cospectral gap and turbulent flux calculations', Journal of Atmospheric and Oceanic Technology, 20(5), pp. 660–672. Available at: https://doi.org/10.1175/1520-0426(2003)20<660:TCGATF>2.0.CO;2.

Von Randow, C. et al. (2002) 'Scale Variability of Atmospheric Surface Layer Fluxes of Energy and Carbon over a Tropical Rain Forest in Southwest Amazonia. I. Diurnal Conditions', Journal of Geophysical Research, 107. Available at: https://doi.org/10.1029/2001JD000379.

Williams, A.G., Kraus, H. and Hacker, J.M. (1996) 'Transport Processes in the Tropical Warm Pool Boundary Layer. Part I: Spectral Composition of Fluxes.', Journal of Atmospheric Sciences, 53, pp. 1187–1202. Available at: https://doi.org/10.1175/1520-0469(1996)053<1187:TPITTW>2.0.CO;2.

Zhang, F. et al. (2007) 'Mesoscale Predictability of Moist Baroclinic Waves: Convection-Permitting Experiments and Multistage Error Growth Dynamics', Journal of the Atmospheric Sciences, 64(10), pp. 3579–3594. Available at: https://doi.org/10.1175/JAS4028.1.